Title	Voltage-controlled interfacial magnetism in Fe/MgO-based structure: interface engineering approach
Author(s)	Suwardy, Joko
Citation	大阪大学, 2019, 博士論文
Version Type	VoR
URL	https://doi.org/10.18910/73592
rights	
Note	

Voltage-controlled interfacial magnetism in Fe/MgO-based structure: interface engineering approach

JOKO SUWARDY

SEPTEMBER 2019

Voltage-controlled interfacial magnetism in Fe/MgO-based structure: interface engineering approach

A dissertation submitted to

THE GRADUATE SCHOOL OF ENGINEERING SCIENCE

OSAKA UNIVERSITY

in partial fulfillment of the requirements of the degree of

DOCTOR OF PHILOSOPHY IN SCIENCE

BY

JOKO SUWARDY

SEPTEMBER 2019

ABSTRACT

Spintronics research has been triggered due to the rich physics beneath it and the tremendous novel applications. One of the most promising applications of spintronic devices is magnetoresistive-random access memory (MRAM) because it promises to be universal memory owing to non-volatility, high-endurance and fast operation speed. However, the manipulation of spin in MRAM is still dominated by an electric-current application, which possesses a Joule heating that too large to be ignored. To achieve a greater impact, energy consumption in MRAM have to be reduced and thus novel scenario of magnetization switching in MRAM is necessary. One of the candidates is voltage-driven switching based on voltage-controlled magnetic anisotropy (VCMA) effect. However, some challenges remain for voltage-driven switching MRAM, such as thermal stability and deterministic switching. These two obstacles can be solved by large VCMA effect, so-called VCMA coefficient, and large voltage-controlled interfacial Dzyaloshinskii-Moriya interaction (VCDMI). Therefore, the research for material which possesses a large coefficient of that both effects are necessary.

I focused on material research for large VCMA, as well as VCDMI. These two effects are interfacial phenomena and therefore, the manipulation of material and interface is the key. In this study, several materials $3d$-metal (Fe, Co, Ni), $4d$-metals (Pd) and $5d$-metal (Ir) are utilized to manipulate the interface of Fe/MgO. The characterization was conducted by using propagating spin-wave spectroscopy. The modulation of resonance frequency of the spin-wave due to voltage application is analyzed and the changes in interfacial perpendicular magnetic anisotropy (i-PMA) and i-DMI are estimated. I demonstrated the enhancement of VCMA and VCDMI via interface manipulation.

Chapter 2 describes the theoretical method and experimental method. The "theoretical method" explains the magnetization dynamics and dispersion relation of magnetostatic surface spin wave from which the VCMA and VCDMI are estimated. The "experimental method" session explains the procedure of sample fabrication and spin-wave spectroscopy measurement through antenna method.

Chapter 3 presents the result and discussion on VCMA and VCDMI. Different materials insertion enhances VCMA in different ways. For Pd, insertion to the top layer are effective to enhance VCMA and the ferromagnetic layer underneath it, through ferromagnetic proximity effect, determines the magnitude. For Ir, the most effective structural to enhance VCMA is

when the Ir atoms are located in the second layer from MgO. Furthermore, I demonstrate that the increase in Ni concentration in CoNi-alloy decreases VCMA. We found that pure-Co as the $3d$ ferromagnetic layer has the maximum VCMA. The VCDMI is demonstrated to be simultaneously tuned and having a magnitude in the same order with VCMA. These results are important for voltage-driven MRAM development.

Content

4

List of Figure

8

Chapter 1   Introduction

Spintronics emerged as a new field of study to complement mainstream charge-based electronics. In a practical sense, the introduction of electron's spin degree of freedom promises to add more capabilities and performance of the electric products, such as non-volatility, increase in areal density, and reduction of electric power consumption. One of the most potential application of spintronic device is magnetoresistive random-access memory (MRAM).

Spin-transfer effect induced magnetization switching has become a common way to switch the magnetization direction in MRAM devices [1], [2]. However, the energy required to switch magnetization directions by the spin-transfer effect is large at ~10^7 times higher than the Landauer limit of $k_B T \ln 2$, where k_B is the Boltzmann constant [3]. This energy dissipation occurs by Joule heating caused by the electron flow. Consequently, a new control technique for magnetization is necessary. Voltage-controlled magnetic anisotropy (VCMA) in ferromagnetic metals [4], [5], a kind of magnetoelectric effect, permits spin manipulation and enables the construction of ultralow-power high-density MRAM [6]. The VCMA can be observed in Fe–MgO-based magnetic tunnel junctions [7]. Furthermore, pure-electronic VCMA, as demonstrated by VCMA-induced precessional magnetization switching [8]–[10] and ferromagnetic resonance excitation [11], [12], showed a high-speed response (<0.1 ns), indicating the feasibility of voltage-driven MRAM. However, the enhancement of VCMA efficiency remains a challenge.

Interface engineering is a promising approach to improve VCMA efficiency because the modulation of magnetic anisotropy arises from electronic modification at the interface of the ferromagnet and an oxide layer. In this study, I engineered the interface of Fe/MgO and investigated its influence to VCMA efficiency, as well as the magnitude of voltage-controlled interfacial Dzyaloshinskii-Moriya interaction (VCDMI).

1.1. Magnetoresistance Effects

The discovery of giant magnetoresistance in 1988 opened up a new era for spin-based electronics [13]. The giant magnetoresistance could only be demonstrated through magnetic hetero-structure which composed of two-ferromagnetic metal (FM) sandwich in between non-
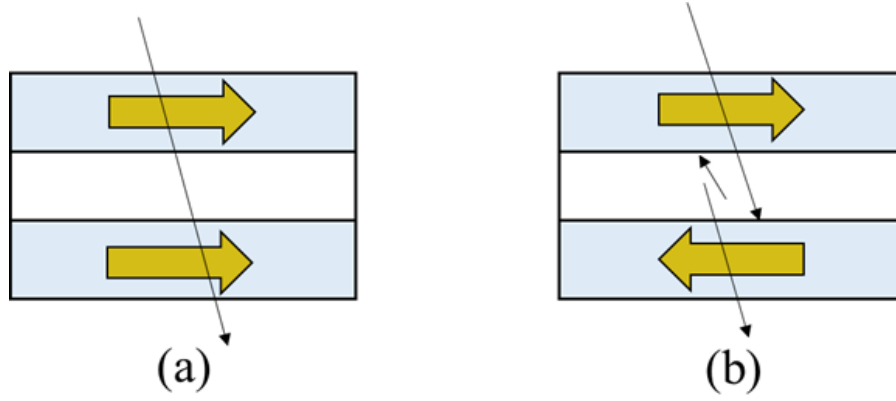
Figure 1.1: Schematic of the giant magnetoresistance effect in spin valve structure: ferromagnetic metal (FM)/non-magnetic metal (NM)/ ferromagnetic metal (FM) trilayer structure. (a) parallel state, (b) antiparallel state. In parallel state, current can travel easily lead to low resistance. On the other hand, in antiparallel state, current will be scattered resulting higher resistance.

magnetic metal (NM) (Figure 1.1). The giant resistance different exhibited between parallel alignment and antiparallel. The resistance change, so called magnetoresistance ratio (MR), typically express as $M_R = (R_{AP} - R_P)/R_p$. The discovery of this effect has a profound impact on understanding of spin-electron transport and its application. One of the application of giant magnetoresistance effect can be found in read head sensor of hard disk drives (HDD), which enabled large areal density in HDD. It was considered as one of the main contribution of spintronic research to information technology [14].

By replacing the spacing NM to oxide material, other phenomenon based on quantum tunneling was observed. This effect is known as tunneling magnetoresistance. In 1995, tunneling magnetoresistance effect in magnetic tunnel junction Fe/Al-O/Fe trilayer was reported [15], [16]. In this report, MR ratio about 20% was obtained, which even larger than reported tunneling magnetoresistance ratio of giant magnetoresistance effect at that time. Since then, research on tunneling magnetoresistance based-magnetic tunnel junction structure had gained significant attention.

A theoretical calculation predicted a giant tunneling magnetoresistance ratio, more than 1000% in Fe(001)/MgO(001)/Fe(001) [17], [18]. This enhancement is attributed to high symmetry filtering effect across MgO barrier. After this report, many efforts had been devoted to MgO-based magnetic tunnel junction research. In 2004, Yuasa et al. [19] and Parkin et al. [20] experimentally demonstrated the giant MR ratio (>180%) in single crystalline MgO-
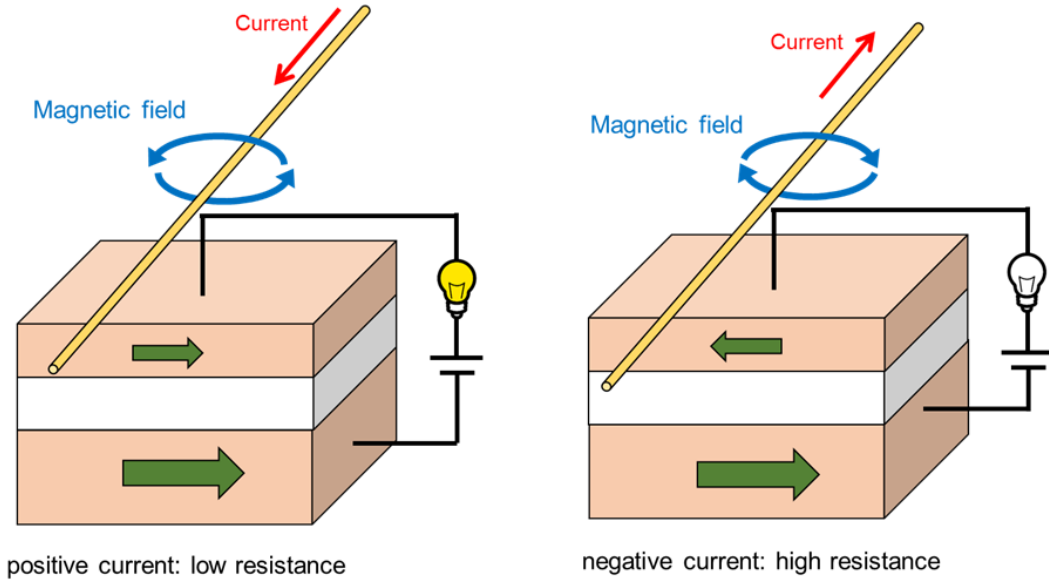
Figure 1.2: Schematic of magnetization switching by induced-magnetic field produced by electrical wire. By changing the direction of the current, the magnetic field is changing, lead to change in the magnetization in thinner (free) layer.

magnetic tunnel junction. After that, a dramatic enhancement in MR ratio (> 200 %) had been observed in sputter-deposited CoFeB/MgO/CoFeB magnetic tunnel junction [21]. Further improvement in MR ratio (>600 %) was reported in CoFeB/MgO/CoFeB pseudo-spin valves annealed at 525 $^{\circ}$C [22] .

The tunneling magnetoresistance effect had been anticipated mainly as a complementary or a substitution for the giant magnetoresistance effect magnetic sensor. However, with such huge MR ratio from tunneling magnetoresistance effect, the realization of non-volatile magnetic memory, so called magnetic random access memory (MRAM) is possible [23]. In the following session, I introduce several methods to switch the magnetization in MRAM. Then, I introduced the research on interfacial perpendicular magnetic anisotropy (i-PMA) and voltage-controlled magnetic anisotropy (VCMA). After that, I introduced the research on voltage effects in antisymmetric exchange, Dzyaloshinskii-Moriya interaction. Finally, the purpose of this dissertation will be given.

1.2. Magnetization switching methods

MRAM is a promising candidate for universal memory owing to non-volatility. The building block in MRAM is magnetic tunnel junction. The advancing in current thin-film
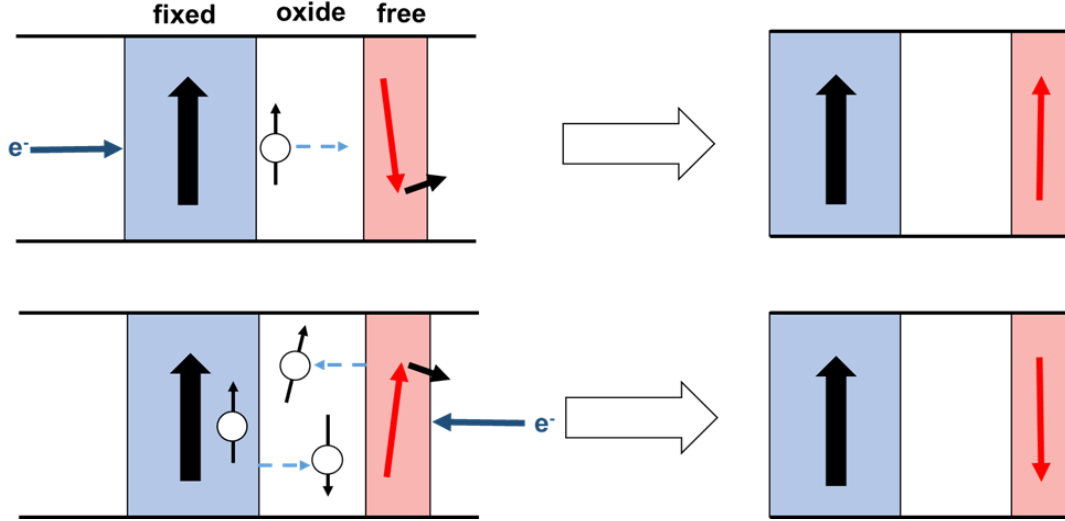
Figure 1.3: Principle of spin-transfer switching in a magnetic tunnel junction. Reversing the current flowing direction will induce either parallel or antiparallel configuration

technology allows to produce small-size magnetic tunnel junction and thus high density MRAM is possible. Moreover, the writing and reading process can be done electrically. High magnetoresistance ratio in MgO-based magnetic tunnel junction can decrease the reading error, makes a reliable reading process. However, one of the remaining crucial challenge is how to efficiently manipulate the magnetization in magnetic tunnel junction.

One of the oldest method to switch magnetization is using electric wire. Figure 1.2 illustrates the switching through electrical current in a magnetic tunnel junction. A magnetic field generated by current flow in the wire. If the magnetic field is sufficient, the magnetization in the free layer can be switched. To toggle the magnetization, simply change the direction of the current. However, the required magnetic field is inversely proportional to the magnetic tunnel junction size [24]. As a result, for a smaller size magnetic tunnel junction higher current is required. Therefore, this way of switching is not suitable for MRAM application in terms of scalability.

Another method is using perpendicular current applied across magnetic tunnel junction which called spin-transfer switching [25]. The principle of spin-transfer switching is illustrated in Figure 1.3. Here, a magnetic tunnel junction structure is assumed, composed of a thicker (fixed) FM layer, insulating layer, and a thin (free) FM layer. The thick FM layer acts as a spin polarizer providing spin-polarized current, while thin layer can be excited by the spin torque. In Figure 1.3(a), electrons flow from thick to thin layer. First, the electrons are polarized favoring the magnetization of thick layer, and then the torque is applied to free layer. If the
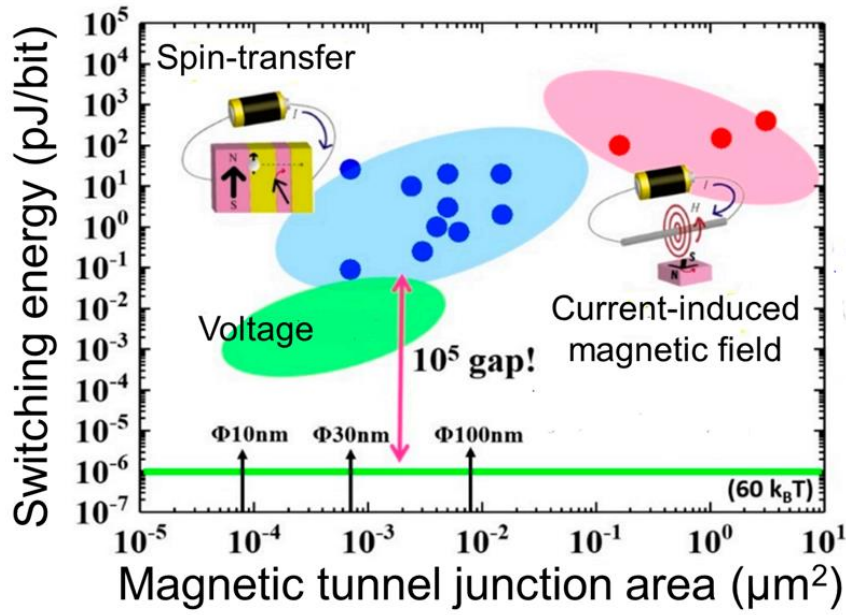
Figure 1.4: Comparison of reported value of switching energy from different magnetization switching techniques as function of magnetic tunnel junction area. The current-induced magnetic field (red-dot), and spin-transfer switching (blue-dot). Green cloud represents the target area of voltage-driven switching MRAM. Picture is reproduced after Ref. [26].

initial position is antiparallel, the free layer will switch. When electron flows from thin layer to thick layer, the direction of the torque applied to thin layer will be reversed, due to opposite spins of reflected electron from thick layer.

Figure 1.4 shows magnetic tunnel junction area dependence of switching energy from several reports on current-induced magnetic field and spin-transfer switching [26]. Drastic reduction of writing current in MRAM had been achieved by spin-transfer switching in comparison to current-induced magnetic field switching (approx. 100 fJ/bit $\approx 10^7$ k_BT) [2]. However, if we compare to required energy for data retention (60 k_BT, correspond to green line in Figure 1.4), there is still a large gap of energy in the order of 10^5 [26]. This energy loss is caused by Ohmic dissipation from the electric-current flow. Therefore, to overcome this issue, a novel magnetization control, free of electric-current, is highly desirable. One of the candidates is by using voltage-effect induced magnetization switching based on voltage-controlled magnetic anisotropy (VCMA) effects. In the next session, more details about VCMA effect and its switching will be given.

1.3. Interfacial perpendicular magnetic anisotropy (i-PMA)
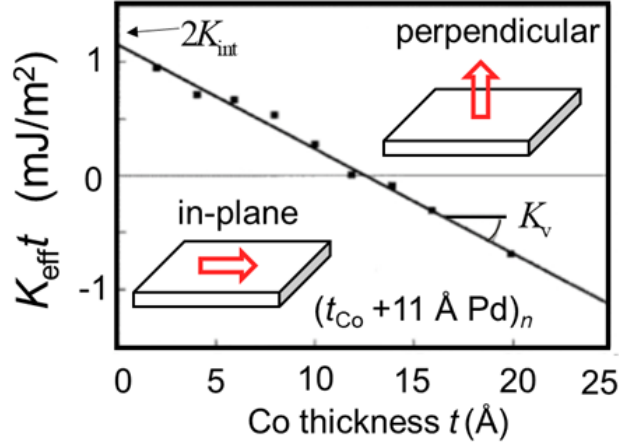
Figure 1.5: A typical $K_{eff}.t$ vs t graph: Thickness of Co layer dependence on $K_{eff}.t$ in Co/Pd multilayer [27]

Normally, the easy axis in ferromagnetic thin film lies in-plane of the film due to domination of demagnetizing field (shape anisotropy). However, at lowered thickness, the easy axis in perpendicular direction can be observed. This phenomenon appears due to magnetic anisotropy result from spin orbit interaction from the lowered symmetry at surface/interface [27],[28],[30]. Therefore, it is often called interfacial perpendicular magnetic anisotropy (i-PMA).

Early experimental observation of i-PMA were reported for ferromagnetic/heavy metal multilayer such as Co/Pd [27] and Co/Pt [31]. Phenomenological effective magnetic anisotropy energy (K_{eff}) can be separated into volume contribution (K_v) and interface contribution (K_{int}), which can be express as:

$$K_{eff} = K_v + \frac{2K_{int}}{t} = K_{cry} - \frac{1}{2}\mu_0 M_s^2 + \frac{2K_{int}}{t}, \qquad (1.1)$$

where, the volume contribution is attributed to bulk-magnetocrystalline anisotropy and demagnetizing field. A typical way to separate these two contribution is by measuring the total effective magnetic anisotropy energy at various thickness, as shown in Figure 1.5. Here, a positive (K_{eff}) indicates the perpendicular magnetic easy axis while negative indicates the in-plane. The K_v can be determined from the slop and K_{int} intercept at 0-nm Co from $K_{eff}.t$ vs t plot (see Figure 1.5). It can be seen, below a certain thickness the interface anisotropy contribution overcome the volume contribution lead to a perpendicularly magnetized film. Later, the i-PMA was also discovered at the ferromagnetic/oxide interfaces such as CoFe/AlO$_x$ [32] and Fe/MgO
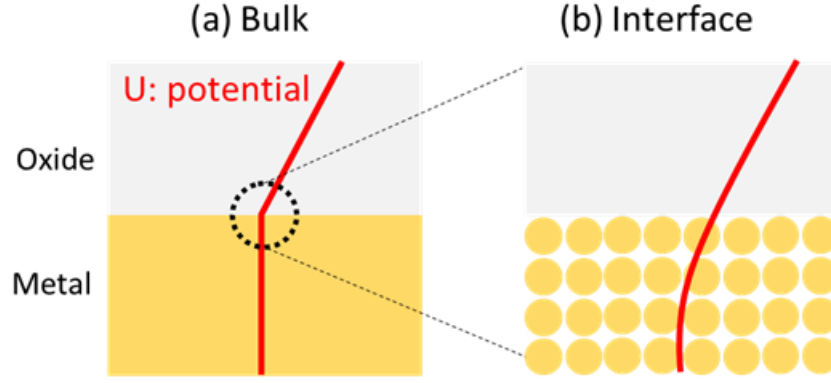
Figure 1.6: Schematic of electric field potential drop in metal/oxide junction. The potential is indicated by the red line

[33]. The magnitude of the i-PMA in these system is surprisingly has the same order with that found in ferromagnetic/heavy metal (~1.4 mJ/m2) [30], even though Co and Fe considerably has low spin-orbit coupling.

1.4. Voltage-controlled magnetic anisotropy (VCMA)

The electric-field manipulation of spin has been reported in various system, i.e. magnetostriction effects manipulation of magnetic properties in magnetic tunnel junction/piezoelectric-material [34], electric-field control phase transition in ferromagnetic semiconductor [35] or in ultrathin-ferromagnetic metal [36], and multiferroics materials [37]. However, these systems have some drawbacks, such as limited operation temperature, and/or low endurance and thus, doesn't suit for MRAM application. Therefore, in this dissertation, I focused on voltage-controlled magnetic anisotropy (VCMA) effect in ferromagnetic-metal/oxide interface. These type of VCMA is known also as pure-electronic VCMA effects.

Voltage effects in ferromagnetic metal have long been considered impractical, because of screening effects by free electrons (see Figure 1.6(a)). However, if we see closely to the interface, actually, electric field penetrates to the interface of metal (order of an atomic layer, as shown in Figure 1.6(b)), before its potential drop as increasing distance from interface. Moreover, in ferromagnetic-metal/oxide system the interface perpendicular magnetic anisotropy (i-PMA) can be existed. Therefore, the modification of magnetic anisotropy at ferromagnetic/oxide interface by using voltage application is anticipated.

17
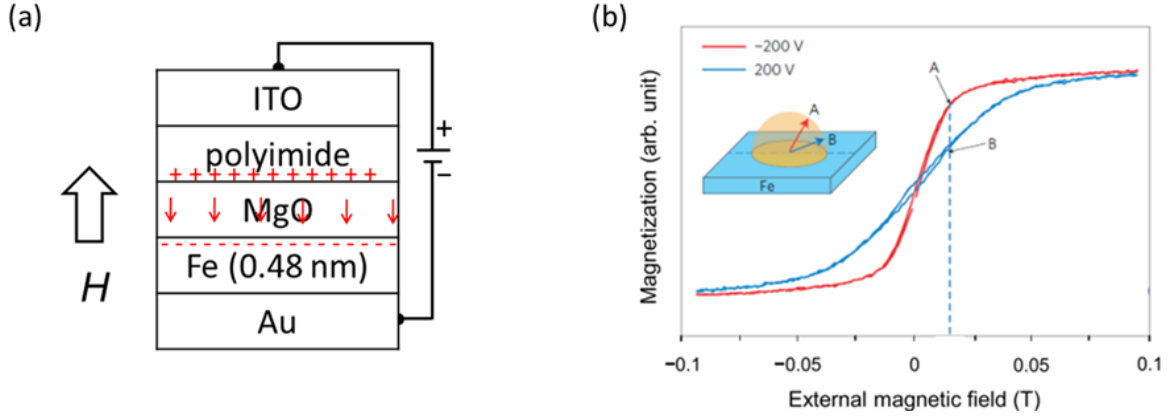
Figure 1.7: One of the earliest report of VCMA effect observation in Fe-MgO-based structure at room-temperature measurement [5]. (a) Device schematic of all-solid state device of Au/Fe/MgO/polymide/ITO subjected to perpendicular external magnetic field and voltage. Upon application of voltage, the electric field built up inside the device. The negative charge will be accumulated at Fe/MgO interface (b) Clear change in hysteresis magnetization curve of 0.48 thick Fe, under different applied bias voltage $\pm$ 200 V suggest the modulation of magnetic anisotropy energy of the film.

In 2009, Maruyama et al., successfully demonstrated the VCMA effect at room-temperature in Fe/MgO-based structure [5]. Figure 1.7(a) shows the schematic sample structure of all solid state device Fe-MgO-based structure. Figure 1.7(b) shows polar magneto-optical Kerr effect (MOKE) hysteresis curves of 0.48 nm-thick Fe that were measured under perpendicular external magnetic field and bias voltage $\pm$ 200 V. One can see an increase in saturation magnetic field under positive voltage, which is the clear evident of the magnetic anisotropy modulation due to voltage application. The mechanism of voltage-modulation of magnetic anisotropy can be considered as follow. Upon the application of voltage, the electric field is built-up inside the device. Under positive voltage, the electron will be accumulated at Fe/MgO interface which change the *d*-band electron density lead to modification of magnetic anisotropy energy. In this system, the phenomenological effective magnetic anisotropy energy can be express as:

$$K_{eff} = K_{v} + \frac{2K_{int}}{t}, \tag{1.2}$$

which can be separated as the contribution of volume anisotropy (K_v) and the interfacial anisotropy (K_{int}). The t denoted the Fe thickness. Since the electric field only effective at
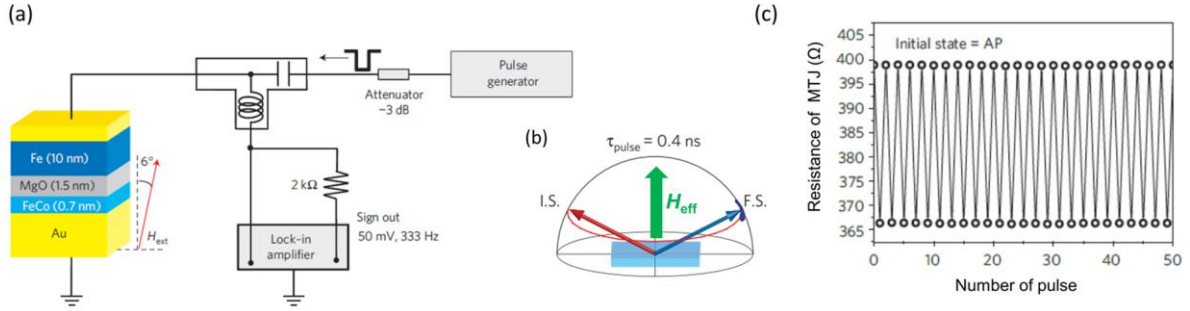
Figure 1.8: First report on VCMA-induced precessional magnetization switching [8]. (a) the sample schematic and measurement circuit with pulse-generator generated short pulse voltage. (b) illustration of magnetization precession by application of 0.4 ns pulse voltage. I.S. indicated the initial position (red) and F.S is final position (blue). (c) MTJ-resistance due to application of 0.55 ns-long pulse voltage with electric field -1V/nm. Resistance changes are clearly observed for AP (antiparalel) and P (parallel) alignment in MTJ.

Fe/MgO interface, the voltage application only modulates the i-PMA. Therefore, the VCMA can be defined as:

$$\text{VCMA [J/V.m]} = \frac{\text{Change in interfacial perpendicular anisotropy (i-\textbf{PMA}) [J/m}^2\text{]}}{\text{Electric Field [V/m]}} \quad (1.3)$$

For this observation in Fe/MgO-based structure the VCMA is 30 fJ/Vm. One of the merits of this reported is because it employed all-solid state based, it can be transferred to magnetic tunnel junction structure. Later, VCMA had been reported in magnetic tunnel junction structure by Shiota et al., [38] and Nozaki et al., [7].

1.4.1. Magnetization switching by VCMA effect

Bi-stable magnetization switching by VCMA effect can't easily be attained because unlike magnetic field, electric field can't break time reversal symmetry. Some reports [39], [40] suggested a bi-stable magnetization switching by combining spin-transfer effect and VCMA. However, in this case, the expectation to reduce the writing energy becomes limited [41]. In 2011, Shiota et al. [8] demonstrated VCMA-induced precessional magnetization switching by using a pulsed voltage in epitaxial $Fe_{80}Co_{20}$/MgO/Fe magnetic tunnel junction, as shown in Figure 1.8 (a). Top 20-nm Fe layer is the reference layer and ultra-thin $Fe_{80}Co_{20}$ (0.7 nm) is the free layer. Figure 1.8 (b) illustrates the magnetization precession in the free layer. At initial the magnetization in the free layer tilted 45° to film plane caused by external magnetic

field. By applying the short pulsed voltage, the i-PMA is erased and the magnetization starts to precess around the effective field. By turn off the voltage, i.e. at half precession time, magnetization end up at stable point. Magnetization can be switch to initial position by applying the same pulse voltage. Figure 1.8 (c) shows the magnetic tunnel junction resistance change due to application of short pulsed voltage. This result shows that VCMA effect can be applied for bi-stable magnetization switching and has a fast switching time (< 1 ns). Moreover, the writing energy are 1/500th than the spin-transfer switching. After that, Kanai et al. [9] and Grezes et al. [10] demonstrated a low writing energy of VCMA precessional switching in high resistance magnetic tunnel junction down to 6 fJ/bit. This result demonstrated the potential to realize ultralow-power MRAM by using VMA induced magnetization switching.

Apart from the merits, some challenges remain toward realization of voltage-driven MRAM, such as, achieving the large VCMA coefficient and low-write error rate. Elimination of i-PMA is required during voltage-induced precessional switching. However, when the cell size is reduced, i-PMA of the free layer need to be high to maintain the thermal stability (for retain the data). Therefore, the large VCMA effect is desirable. The target VCMA coefficient is estimated in the range of 200 fJ/Vm to 500 fJ/Vm for cache memory and 600 fJ/Vm to 1500 fJ/Vm for main memory application [26]. However, to date the VCMA coefficient in practical material such as CoFeB is still limited to about 100 fJ/Vm [42], [43]. Therefore, the material research for large VCMA effect is necessary.

1.4.2. Material research for large VCMA

In order to search for material with large VCMA, the understanding of the physical origin of this effect is important. Several mechanisms of VCMA effect had been studied for different system. One of the earliest theoretical study was reported in 2008. Duan et al. [44] reported, by first-principles calculation, that the VCMA effect in ferromagnetic metals appears due to spin-dependent screening of electric field at metal surface. The bias-voltage induces considerable changes in the surface/interface magnetization and surface/interface magneto-crystalline anisotropy. The VCMA coefficient and its sign, was explained to be depended on the density and spin polarization of the charges carrier near the fermi level of the ferromagnet. In 2009, Nakamura et al., [45] by using first-principles calculation, showed the changes in band structures of monolayer-Fe upon application of bias-voltage. They claimed that the coupling between p orbitals and d orbital near the Fermi level plays important role. It is interesting to

20
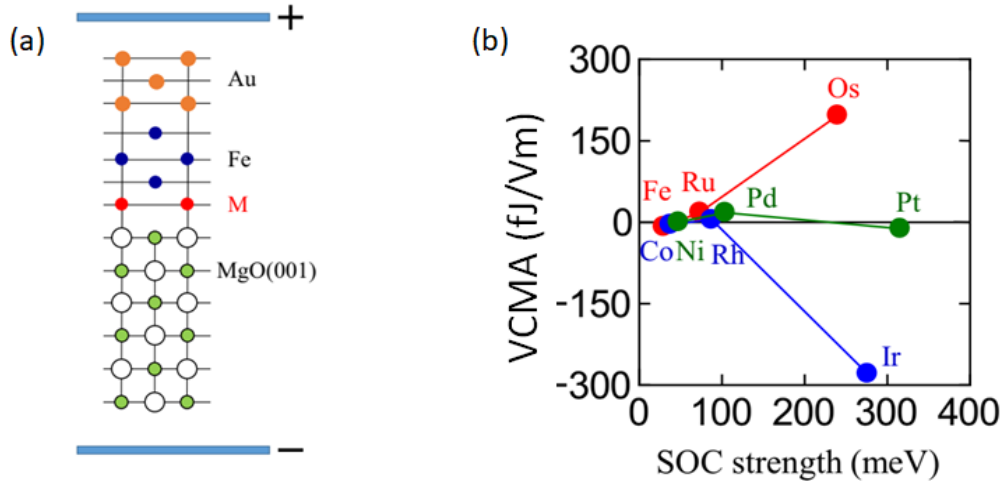
Figure 1.9: First principles study on heavy-metal materials insertion at Fe/MgO interface [49]. (a) schematic of the atomic structure model, M is the insertion material, (b) VCMA results of several insertion materials.

note, from these two reports that orbital magnetic moment anisotropy of Fe changes considerably due to voltage application, lead to changes in i-PMA energy. Tsujikawa et al., [46] studied Pt/Fe/Pt/vacuum and obtained that accumulated charges at the surface modified the electron $3d$- orbital band filling cause substantial change in i-PMA. Other possible mechanism also been discussed such as Rasbha spin-orbit anisotropy [47] and strain-induced VCMA effect [48].

Nakamura et al. reported the effect of heavy-metal insertion: $4d$ (Ru, Rh, Pd) and $5d$ (Os, Ir, Pt) at Fe/MgO interfaces of VCMA by first-principles calculation [49] . The interface-i-PMA arises from spin-orbit interaction of electron spin with the atomic lattice and thus large spin orbit coupling material might increase the electric field effect on i-PMA. They found insertion of $5d$-metal Ir and Os are effective to enhance VCMA (Figure 1.9). Several experimental studies had been conducted by inserting a metal layer at CoFeB-based/MgO system, but the reported VCMA coefficient was less than 100 fJ/Vm [50] [43]. Recently, Nozaki et al. demonstrated a high VCMA of -320 fJ/Vm in FeIr-alloy/MgO system [51]. This result showed the possibility to obtain giant VCMA effect by large-spin orbit coupling material.

Other than $5d$-metal, VCMA effect involving $4d$-metal Pd had been reported experimentally. Hibino et al. reported VCMA effects up to -66 fJ/Vm in sputter-deposited Pt/Co/Pd/MgO system. They consider the VCMA effect in this system attributed to

21
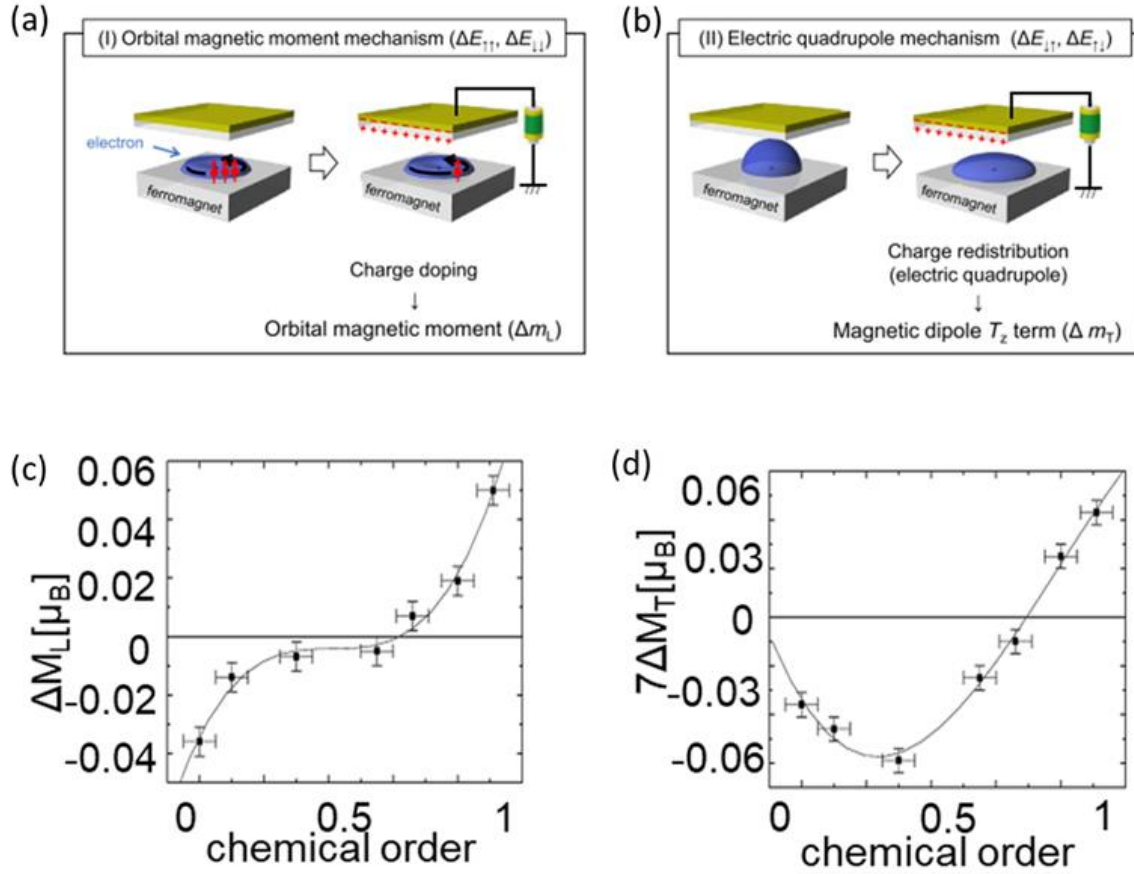
Figure 1.10: Two possible mechanism affects pure electronics VCMA effects [52], [41] (a) orbital magnetic moment mechanism and (b) electric-quadrapole mechanism. Controlling both mechanism through chemical order (1 is ordered) in FePd system, reported by [53], (c) orbital magnetic moment Δm_L and (d) magnetic dipole Δm_T as function of chemical order.

ferromagnetic proximity induced effects in Pd layer. The bulk Pd actually a paramagnetic but in the low dimension and deposited on the ferromagnetic layer such as Fe and Co, it could become ferromagnet. This report gives an insight that not only the insertion of heavy metal layer insertion at Fe/MgO can be tuned to observe enhancement in VCMA but also the ferromagnetic layer beneath it can be important. Subsequently, Hibino et al., reported the VCMA in the same system measured at low-temperatures. They observed a non-linear VCMA up to 1600 fJ/Vm at 10 K. They explained that this giant VCMA attributed to temperature dependence of strain in Pd. However, only static measurement had been done thus the response speed of this VCMA has not been confirmed yet. For MRAM application, it is important to reveal whether this VCMA is purely-electronics effect or not.

Miwa et al. [52] investigated the VCMA effect in $L1_0$-FePt by using element specific measurement x-ray magnetic circular dichroism (XMCD), and x-ray absorption spectrum (XAS) and proposed possible mechanism of pure-electronics VCMA effect. The VCMA effect in this system arose from two mechanisms. First, the charge doping induced anisotropy in orbital magnetic moment (Figure 1.10(a)) and the second is electric quadrupole mechanism due to charge redistribution upon bias voltage (Figure 1.10(b)). By treating the second-order perturbation of the spin-orbit interaction, the PMA energy (ΔE) can be express as [41]:

$$\Delta E \approx -\frac{1}{4}\frac{\lambda'}{\hbar}\left(\left\langle \Delta L_{\zeta,\downarrow\downarrow}\right\rangle - \left\langle \Delta L_{\zeta,\uparrow\uparrow}\right\rangle\right) + \frac{7}{2}\frac{\lambda'}{\hbar}\left(\left\langle \Delta T'_{\zeta,\downarrow\uparrow}\right\rangle + \left\langle \Delta T'_{\zeta,\uparrow\downarrow}\right\rangle\right) \tag{1.4}$$

Here, the PMA energy is defined as spin-orbit interaction energy from perpendicular magnetize film subtracted with in-plane magnetized one. Where, λ' is the spin-orbit coupling coefficient in the d-band, $\left\langle \Delta L_\zeta\right\rangle$ and $\left\langle \Delta T'_\zeta\right\rangle$ are the expectation value of angular momentum (**L**) and magnetic dipole operator (**T**), respectively. The $\uparrow(\downarrow)$ denotes for the contribution from the majority (minority) spin band. The orbital magnetic moment (m_L) and the effective spin moment ($m_{eff} = m_s - 3m_T$) can be characterized by using sum-rule analysis from XMCD spectra. Because the m_s is usually isotropic the effective spin moment change can be approximated as $\Delta m_{eff} \approx \Delta m_T$. The relation of the orbital magnetic moment change Δm_L and magnetic dipole change Δm_T can be expressed as [41]:

$$\begin{aligned}\Delta m_L &\equiv m_{L,\perp} - m_{L,//}\\ &= -\frac{\mu_B}{\hbar}\left(\left\langle \Delta L_{\zeta,\uparrow\uparrow}\right\rangle + \left\langle \Delta L_{\zeta,\downarrow\downarrow}\right\rangle\right)\end{aligned} \tag{1.5}$$

$$\begin{aligned}\Delta m_T &\equiv -7m_{T,\perp} - (-7m_{T,//})\\ &\approx -\frac{\mu_B}{\hbar}\left(\left\langle \Delta L_{\zeta,\uparrow\uparrow}{}^2\right\rangle - \left\langle \Delta L_{\zeta,\downarrow\downarrow}{}^2\right\rangle\right) - \frac{7\mu_B}{\hbar}\left(\left\langle \Delta T'_{\zeta,\downarrow\uparrow}\right\rangle + \left\langle \Delta T'_{\zeta,\uparrow\downarrow}\right\rangle\right)\end{aligned} \tag{1.6}$$

They found the large contribution from Δm_T and smaller contribution of $\Delta m_{L,\downarrow(\uparrow)}$. However, these two contribution partially canceled out each other and thus limited the total VCMA coefficient of 140 fJ/Vm. Nevertheless, this report suggested once the material with constructive contribution of both term is to be design the VCMA with magnitude 10 times larger are feasible [52]. Previous report has demonstrated the orbital magnetic moment and magnetic dipole can be tuned by controlling the chemical order [53], as shown in Figure 1.10(c) and (d). Hence, the VCMA coefficient is expected to be controlled with the same manner.
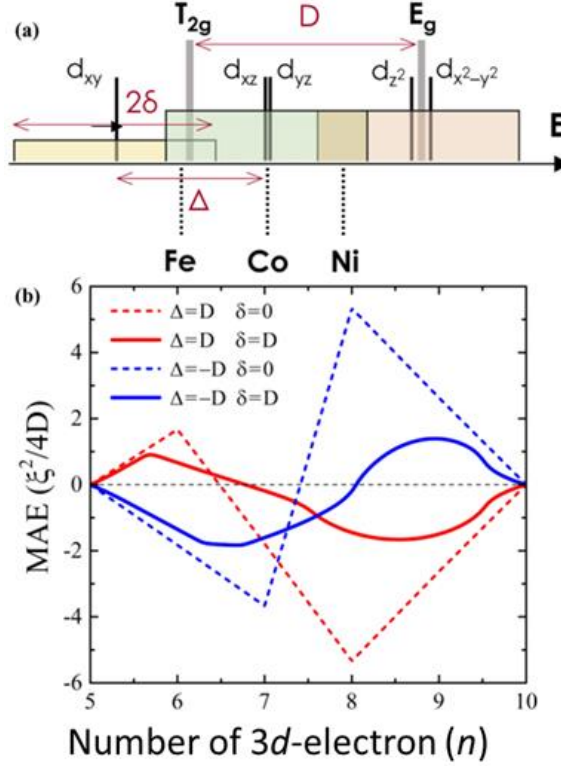
Figure 1.11: A qualitative picture of magnetic anisotropy energy as function of number of 3*d*-electron [54]. (a) schematic of 3*d*-orbital splitting by tetragonal symmetry crystal field. (b) magnetic anisotropy energy as function of number of 3*d*-orbital electron for different T_{2g} level splitting (Δ) and broadening (γ).

Apart from using heavy metal insertion, alloying 3*d*-ferromagnet itself can be potential to increase VCMA coefficient. In 2017, Zhang et al. proposed a simple picture of VCMA influenced by 3*d*-orbital electron occupation in ferromagnetic metal. Figure 1.11 shows the magnetic anisotropy of ferromagnetic metal as function of 3*d*-orbital filling calculated using second order perturbation theory. The VCMA is indicated by the slope of the curve. The clean surface and more realistic case (overlap of band) are represented by solid red line. It can be seen the sign of VCMA effect may change around $n = 5.5$. Furthermore, one peculiar slope indicates possible high VCMA in Co-Ni region, around $n = 7.5$.

1.5. Interfacial Dzyaloshinskii-Moriya interaction (i-DMI) and its voltage-modulation

The DMI is an antisymmetric exchange interaction which appears in system with lack of spatial inversion symmetry incorporating with spin-orbit interaction. The DMI was first introduced by Dzyaloshinskii in 1957 to explain the weak ferromagnetism observed in
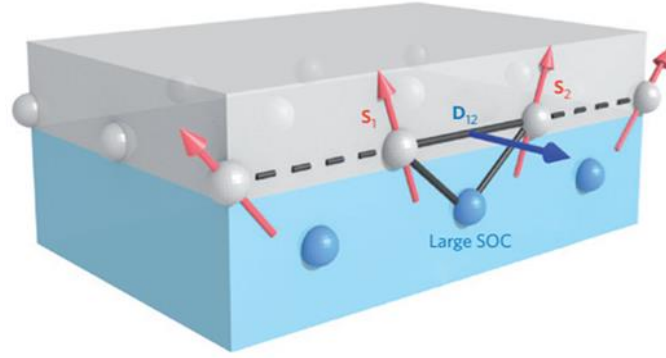
Figure 1.12: Schematic of a DMI at the interface of ferromagnetic metal (grey) and heavy metal with strong spin orbit coupling [62].

materials like α-Fe$_2$O$_3$ [55]. Then, Moriya showed that this interaction can be derived analytically from Hamiltonian of interacting electrons by considering relativistic spin-orbit correction [56]. The DMI plays important role to magnetic properties in various systems, such as spin glass [57], molecular magnet [58], cuprates [59], multiferroics [60], and chiral magnetic structure [61]. In multiferroics materials, the DMI is important key in magnetoelectric effect because this interaction responsible for electric polarization. Recently, the DMI in thin magnetic film gained much attention because its role in stabilization of skyrmions and magnetic domain walls [62], [63]. Moreover, the voltage-controlled DMI is proposed for deterministic voltage-driven precessional switching [64].

In ultrathin ferromagnet, the DMI can arise from inversion symmetry breaking at interface, so called, interfacial DMI (i-DMI). Figure 1.12 depicted the existence of DMI at the interface of ferromagnetic/heavy metal layer with large spin orbit coupling. The DMI between two atomic spin $\mathbf{S}_1$ and $\mathbf{S}_2$ can be express as $H_{\mathrm{DMI}} = -\mathbf{D}_{12} \cdot (\mathbf{S}_1 \times \mathbf{S}_2)$, where $\mathbf{D}_{12}$ is the DMI vector, related to the triangle composed two magnetic sites and atom with large spin orbit coupling. This i-DMI may exist regardless of crystal symmetry and much stronger than bulk interaction [65]. The i-DMI can be tuned through interfacial engineering to control the chiral magnetic structure type and velocity of domain walls [65].

The observations of i-DMI are mainly be done by probing spin wave (magnon) excitation. One of the first observation was reported by Zakeri et al. [66], by using spin-polarized electron energy loss spectroscopy (SPEELS). They reported asymmetric spin-wave excitation in W/Fe which attributed to i-DMI   All electrical measurement by using microwave antenna to excite spin wave, also been reported to characterize i-DMI energy [68].
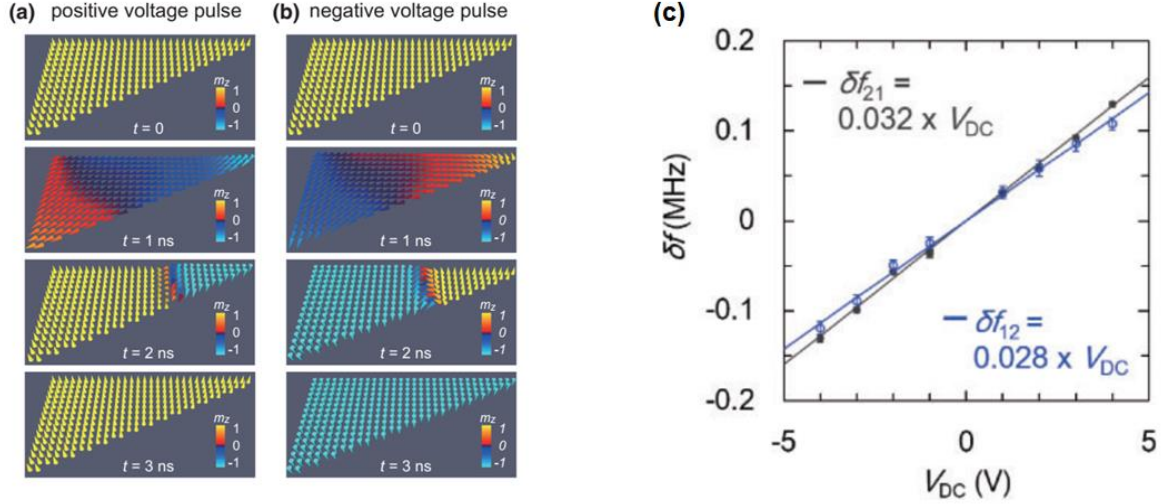
Figure 1.13: Micromagnetic simulation of perpendicular magnetized triangle subjected to in-plane external magnetic field switched by applying voltage pulse (a) positive, (b) negative voltage pulse. The final state of magnetization is determined by polarity of voltage pulse. Picture taken from Ref. [64]. (c) experimentally measured voltage-controlled interfacial DMI (VCDMI) in Au/Fe/MgO multilayer. The voltage-induced frequency shift δf is influenced by chirality of spin which attributed to i-DMI modulation. Picture taken from Ref. [69]

For a practical purpose, having a large i-DMI energy is necessary, i.e. for stabilization of skyrmions state in skyrmions device [63], and high velocity current-driven domain wall device [70]. Furthermore, being able to manipulate the i-DMI is another critical issue. Imamura et al., [64] proposed the deterministic switching of voltage-induced precessional switching. They performed the micro-magnetic simulation and demonstrated VCMA and voltage-controlled i-DMI (VCDMI) can switch the perpendicular magnetized triangle. The final state of magnetization is determined by the polarity of voltage pulsed regardless to initial magnetization state as shown in Figure 1.13(a) and (b). Experimentally, Nawaoka et al. [69] successfully demonstrated VCDMI in Au/Fe/MgO artificial multilayer. They performed spin-wave spectroscopy by using micro-size antenna and observed the non-reciprocal magnetostatic surface spin wave (MSSW) propagating subjected to voltage bias. The VCDMI can be defined as:

$$\text{VCDMI [J/V.m]} = \frac{\text{Change in i-DMI energy density } (D) \; [\mu J/m^2]}{\text{Electric Field [V/nm]}} \tag{1.7}$$

However, the magnitude of VCDMI in Au/Fe/MgO system is still low, estimated about 7 fJ/Vm. Nevertheless, this result shows the possibility of voltage-controlled i-DMI, in particular for ferromagnetic/oxide interface

1.6. Purpose

The ability to manipulate magnetic properties with electric-field has significant merit in term of energy efficiency. In this dissertation, we focused on voltage-effects on two interfacial magnetisms; interfacial perpendicular magnetic anisotropy (i-PMA) and interfacial Dzyaloshinskii-Moriya interaction (i-DMI). The related phenomena of the voltage modulation of these two properties it called; voltage-controlled magnetic anisotropy (VCMA) and voltage-controlled Dzyaloshinskii-Moriya interaction (VCDMI). Since the i-PMA and i-DMI were arose from spin-orbit interaction, we employed the heavy-metal material Pd and Ir, which have large spin-orbit coupling in combination with $3d$-metal Fe, Co and Ni.

I studied the VCMA and VCDMI effects in single-crystalline Fe/MgO-based structure. By engineered the interface of Fe/MgO, I try to control the VCMA and VCDMI in the system. I used three approaches to engineer the interface:

1. Atomic layer insertion (Co/Pd combination),

2. Artificial alloy-formation (Ir location control in Fe layer), and

3. Control of the number of d-electron (Ni fraction dependence in $Co_{1-x}Ni_x$ layer)

The deposition of multilayer thin film was carried out by using electron beam evaporation molecular beam epitaxy. During the deposition, a position-controlled linear shutter was employed to engineer the interface material attached to MgO. Moreover, post-annealing treatment was also being done.

The characterization of VCMA and VCDMI was conducted through spin-wave spectroscopy by using two port vector network analyzer measurement. This technique has several merits compare to common VCMA characterization through magnetization curve change. The spin-wave spectroscopy has advantageous to study VCMA with various thickness because it applicable to materials with wide range of interfacial PMA (i-PMA), while in common method, its often difficult to study because the changes in magnetization curves is too small. Moreover, by using two antennas, the propagation dependent of spin-wave resonance

27

under influenced of voltage can be utilized to characterize the VCMA and VCDMI simultaneously.

Chapter 2   Method

In the following sections the method which used to analyze i-PMA field (H_{int}), VCMA and VCDMI are explained. The theoretical method section describes the analytical expression of VCMA and VCDMI derived from dispersion relation of magnetostatic surface spin-wave (MSSW). The experimental method section describes the sample fabrication including the multilayer deposition and microfabrication of coplanar waveguide antennas. The details explanation of propagating spin-wave measurement by two-port vector network analyzer will be given.

2.1. Theoretical method

2.1.1. Energies in Ferromagnet

The total energy inside a ferromagnet is constructed by number of interactions. The knowledge of the involving energies is crucial to portray the dynamics. In this section, the following energies which considerably important in this study are introduced.

➢ **Zeeman Energy**

Under an external magnetic field $\mathbf{H_{ext}}$, a ferromagnetic tend to align their magnetization in the same direction to minimize the energy. The energy density is given by [71]

$$\varepsilon_{zee} = -\frac{\mu_0}{V}\int(\mathbf{M}\cdot\mathbf{H_{ext}})dV,$$ (2.1)

where $\mu_0 = 4\pi\times10^{-7}$ H/m is permeability of free space

➢ **Exchange Energy**

The exchange interaction was initially proposed by Heisenberg [72]. This interaction reflects the Coulomb interaction of neighboring atoms in conjunction with Pauli exclusion principle, which forbids the two electrons to have the same quantum state. Between two atoms with spin $\mathbf{S}_i$ and $\mathbf{S}_j$ there is an interaction with energy [73].

$$E_{ex} = -2J\mathbf{S}_i \cdot \mathbf{S}_j \tag{2.2}$$

where J is being exchange integral. If $J > 0$, the energy is lowest when $\mathbf{S}_i$ and $\mathbf{S}_j$ are parallel. The interaction decrease rapidly with increasing distance (short-range), hence the value of J is largest for nearest-neighbor spins. For positive J, the tendency to align the nearest neighbor spins parallel causes complete parallel alignment of the entire system, lead to ferromagnetism.

The exchange energy density at mesoscopic level is given by [74]

$$\varepsilon_{ex} = \frac{A}{V} \int \left(\nabla \cdot \frac{\mathbf{M}}{M_s} \right) dV, \tag{2.3}$$

where $\mathbf{M}$ is magnetization vector, M_S being saturation magnetization. A is the exchange integral which is proportional to the exchange integral J, by $A \approx JS^2 Z_c/a_0$, where S is magnitude of the spin, Z_c is number of atoms per unit cell, and a_0 is the lattice constant.

> **Demagnetizing Field Energy**

The demagnetizing field, also known as the stray field, is the magnetic field generated by the magnetization of the ferromagnet itself. The energy density of demagnetizing filed can be written as:

$$\varepsilon_d = -\frac{\mu_0}{2V} \int \left(\mathbf{M} \cdot \mathbf{H}_d \right) dV, \tag{2.4}$$

The demagnetizing field of a material with arbitrary shape is very difficult to calculate. However, for a special case, in uniformly magnetized ellipsoids, the demagnetizing field is expressed by [74]:

$$\mathbf{H}_d = -\bar{N}\mathbf{M} \tag{2.5}$$

where $\bar{N}$ is the demagnetizing tensor, with unit trace $N_x + N_y + N_z = 1$. For a thin film with z-axis perpendicular to film plane, $N_x = N_y = 0$, and $N_z = 1$. Thus, in the in-plane magnetized thin film, the Eq. (2.5) can be written

$$\varepsilon_d = -\frac{\mu_0}{2V} \int \left(\mathbf{e_z} \cdot \mathbf{M} \right)^2, \tag{2.6}$$

where $\mathbf{e_z}$ is the unit vector in the z-direction, perpendicular to film plane.

> **Anisotropy energy**

Anisotropy energy is resulted from spin-orbit interaction [75]. The direction of magnetization relative to atomic arrangement inside a ferromagnet determined the energy. Even though is considerably smaller than exchange energy, anisotropy energy plays important role in low-dimension such as thin film. Here, I briefly explain the anisotropy energy in crystalline structure and interface. The anisotropy due to shape effects already introduced and treated as demagnetizing field energy.

Anisotropy energy in crystalline material is determined by its crystal structure. For a cubic crystal, the energy density in Cartesian coordinate is given by [71]:

$$\varepsilon_{\text{cry}} = K_1(m_x^2 m_y^2 + m_x^2 m_z^2 + m_y^2 m_z^2) + K_2 m_x^2 m_y^2 m_z^2 \tag{2.7}$$

where m_i is the magnetization component along the cubic axes. K_1 is the highest value anisotropy constant, typically $\pm 10^4 \, \text{J/m}^3$, varies with materials [71]. The constant K_2 and higher order constant usually can be neglected.

Apart from volume attributed above, a phenomenological magnetic anisotropy from interface contribution is often observed in thin films. This effects attributed to the environment condition of surface atom, such as discontinuity of crystal ordered. For a very thin layers (<2 nm), the interfacial anisotropy can dominate and lead to a perpendicular magnetic anisotropy (PMA). The energy density for interfacial anisotropy can be described as

$$\varepsilon_{\text{int}} = -\frac{K_{\text{int}}}{t} m_z^2 \tag{2.8}$$

where K_{int} is interfacial anisotropy constant and t is film thickness.

> **Dzyaloshinskii-Moriya energy**

A material with low symmetry exhibit a weak antisymmetric interaction, induced by spin-orbit coupling, the Dzyaloshinskii-Moriya interaction (DMI). The energy of DMI is described

$$\varepsilon_{\text{DMI}} = \mathbf{D}_{ij} \cdot (\mathbf{S}_i \times \mathbf{S}_j) \tag{2.9}$$

where $\mathbf{D}_{ij}$ is the Dzyaloshinskii-Moriya interaction vector.

In thin film ferromagnet, this effect appears at the interface of material due to lack of inversion symmetry, so called, interfacial-DMI. Many efforts have been devoted enhance and modulated the i-DMI effect because it is responsible to stabilize a chiral magnetic structure skyrmions [63], [62].

From all the contributing energies in ferromagnet, we can calculate the total energy as

$$\varepsilon_{tot} = \varepsilon_{ex} + \varepsilon_{zee} + \varepsilon_{d} + \varepsilon_{cry} + \varepsilon_{cry} + \varepsilon_{int} + \varepsilon_{DMI} \tag{2.10}$$

From this equation, the total effective magnetic field can be calculated as

$$\mathbf{H}_{eff} = -\frac{1}{\mu_0} \nabla_{\mathbf{M}} \varepsilon_{tot} \tag{2.11}$$

The $\mathbf{H}_{eff}$ determines the instantaneous axis magnetization precession.

2.1.2. Magnetization Dynamics and Spin waves

• **Magnetization Dynamics**

Inside a ferromagnet the magnetization dynamics appears due to effective magnetic field ($\mathbf{H}_{eff}$) as shown in Figure 2.1. The first model for magnetization dynamics was introduced in 1935 by Landau-Lifshitz (LL):
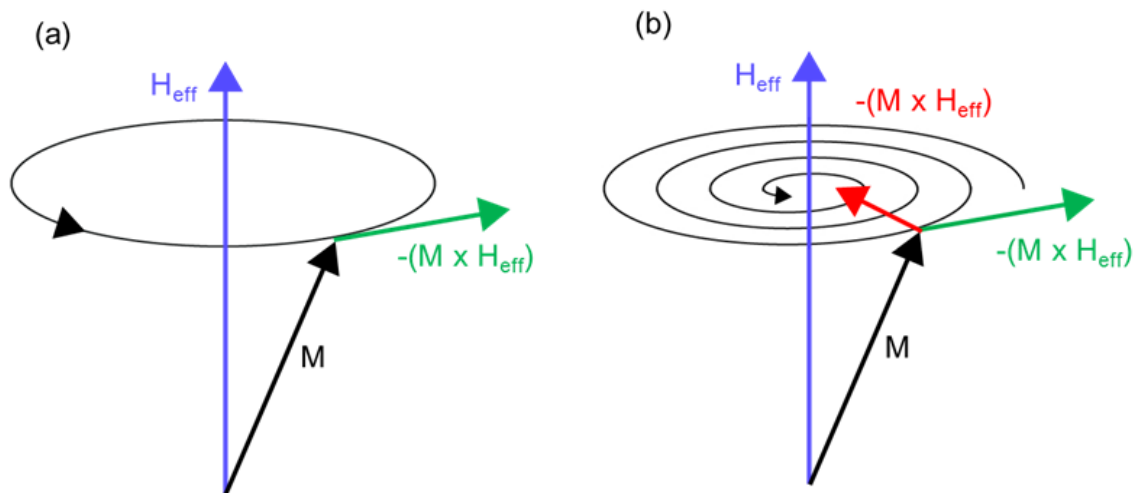
Figure 2.1: Schematic of magnetization precession (a) without a damping, and (b) with a phenomenological damping term (red) lead to magnetization relaxation in direction of $H_{eff.}$

$$\frac{d\mathbf{M}}{dt} = -\gamma\mu_0\mathbf{M}\times\mathbf{H}_{\text{eff}},$$ (2.12)

where γ is the gyromagnetic ratio. The $\gamma = g\,q\,/\,2m_e$, where g is called *Lande' g*-factor, q is charge of electron and m_e is the mass of electron. This model describes a precessional motion of magnetization around effective magnetic field. However, this model can't explain the experimental observation. After a finite time, the magnetization direction should be aligning to minimal energy direction. Landau-Lifshitz modified this disparity by adding a damping term[76]

$$\frac{d\mathbf{M}}{dt} = -\gamma\mu_0\mathbf{M}\times\mathbf{H}_{\text{eff}} - \frac{\lambda}{M_s^2}\mathbf{M}\times(\mathbf{M}\times\mathbf{H}_{\text{eff}}),$$ (2.13)

where λ is phenomenological damping constant. In 1995, Gilbert modified the damping term in LL equation. The damping term in Gilbert model depends on the time derivative of magnetization. The equation then be known as Landau-Lifshitz-Gilbert (LLG) equation, which given by

$$\frac{d\mathbf{M}}{dt} = -\gamma\mu_0\mathbf{M}\times\mathbf{H}_{\text{eff}} + \frac{\alpha}{M_s}(\mathbf{M}\times\frac{d\mathbf{M}}{dt}),$$ (2.14)

where α is dimensionless damping parameter after Gilbert.

- **Spin waves**

   In the previous sub-section only the uniform magnetization motion which occurs at a same frequency and phase was addressed. A non-uniform magnetization precession can also exist in ferromagnetic material due to defects or non-uniform applied magnetic field (Figure 2.2(a)).This type of precession mode excites the spin wave (also known as magnon). The spin wave which dominated by exchange interaction has a short wavelength. In contrary, in infinite ferromagnetic thin film, a long wavelength spin wave can be excited, govern by dipolar interaction [77]. This type of spin wave is referred as magnetostatic mode. There are three types of magnetostatic spin-wave, determined by the angle between magnetization (**M**) direction and the in-plane wave vector (k). Figure 2.2(b) shows the geometry and dispersion relations in different magneto-static spin wave mode. In this study, I utilized the magnetostatic surface wave (MSSW) mode, where thin film is magnetized in-plane and k is detected in-plane perpendicular to M, to characterize magnetic anisotropy change. In the following section I
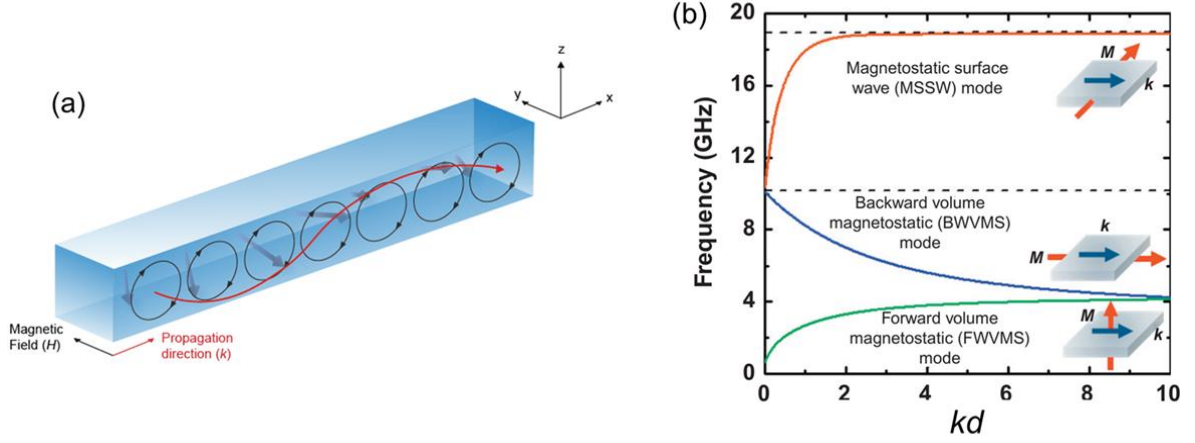
Figure 2.2: (a) Schematic excited spin-wave under external magnetic field. *k* propagates along *x*-direction resulted by non-uniform precession of spin around external magnetic field direction. (b) The geometry and dispersion relation of magnetostatic spin-wave. In the study, I use the magnetostatic surface spin-wave (MSSW) configuration. Picture taken after [77].

derived the basic equation of magnetostatic mode (Walker's equation), dispersion relation of MSSW and present the relation of VCMA and VCDMI to frequency shift of MSSW resonance.

- **Walker's Equation**

In this section, basic equation for magnetostatic wave, so called Walker equation, is derived [78]. In the frequency domain Maxwell's equation can be written

$$\nabla \times \mathbf{H} = -i\omega \mathbf{D} + \mathbf{J}, \tag{2.15}$$

$$\nabla \times \mathbf{E} = i\omega \mathbf{B}, \tag{2.16}$$

$$\nabla \cdot \mathbf{D} = \rho \tag{2.17}$$

$$\nabla \cdot \mathbf{B} = 0 \tag{2.18}$$

where **H** is the magnetic field intensity (A/m), **D** is the electric flux density (C/m^2), **B** is magnetic flux density (T), **J** is the electric current density (A/m^2), **E** is the electric field intensity (V/m), and ρ is being the electric charge density (C/m^3). Inside a material the flux density D and B are related to the field intensity as follow

$$\mathbf{D} = \varepsilon_0 \mathbf{E} + \mathbf{P}, \tag{2.19}$$

34

$$\mathbf{B} = \mu_0(\mathbf{H} + \mathbf{M}), \tag{2.20}$$

where $\mathbf{P}$ is the electric dipole moment (C/m^2) and $\mathbf{M}$ is being magnetic dipole moment (A/m), usually referred as the polarization and magnetization, respectively. If the response is non-instantaneously to the given field, the response must be obtained by integrating over all excitations. This type of material is called dispersive medium. However, in frequency domain the response always reaches a steady state condition and thus the integration is not necessary. Therefore, the polarization and magnetization can be written as:

$$\mathbf{P}(\omega) = \varepsilon_0 \overline{\chi}_e(\omega) \cdot \mathbf{E}(\omega) \tag{2.21}$$

$$\mathbf{M}(\omega) = \overline{\chi}_m(\omega) \cdot \mathbf{M}(\omega) \tag{2.22}$$

where $\overline{\chi}_e$ and $\overline{\chi}_m$ are the electric and magnetic susceptibility tensor, respectively. Substituting above equations to Eq.(2.19) and Eq. (2.20) gives

$$\mathbf{D} = \overline{\varepsilon} \cdot \mathbf{E} \tag{2.23}$$

$$\mathbf{B} = \overline{\mu} \cdot \mathbf{H} \tag{2.24}$$

where, $\overline{\varepsilon}$ and $\overline{\mu}$ are the permittivity and permeability tensor which can be express as

$$\overline{\varepsilon} = \varepsilon_0(\overline{\mathbf{I}} + \overline{\chi}_e) \tag{2.25}$$

$$\overline{\mu} = \mu_0(\overline{\mathbf{I}} + \overline{\chi}_m) \tag{2.26}$$

$\overline{\mathbf{I}}$ is a unit matrix.

Now, let's consider a Fe thin film magnetized in z-direction by applying external magnetic field (same geometry as depicted in Figure 2.3). We assume motion of the fields as small time-dependent perturbation added to static equilibrium. For simplicity, the exchange field and anisotropy field are neglected:

$$\mathbf{M} = \mathrm{M}_s \hat{z} + \mathbf{m}e^{-i\omega t} \tag{2.27}$$

$$\mathbf{H}_{\mathrm{eff}} = \mathrm{H}_{\mathrm{ext}} \hat{z} + \mathbf{h}e^{-i\omega t} \tag{2.28}$$

insert above equations to Eq. (2.12), gives us:

$$\frac{d\left(\mathrm{M}_s \hat{z} + \mathbf{m}e^{-i\omega t}\right)}{dt} = -\gamma\mu_0\left(\mathrm{M}_s \hat{z} + \mathbf{m}e^{-i\omega t}\right) \times \left(\mathrm{H}_{\mathrm{ext}} \hat{z} + \mathbf{h}e^{-i\omega t}\right) \tag{2.29}$$

$$\frac{d\left(\mathrm{M}_s \hat{z} + \mathbf{m}e^{-i\omega t}\right)}{dt} = -\gamma\mu_0\left(\begin{array}{c}\mathrm{M}_s \hat{z} \times \mathrm{H}_{\mathrm{ext}} \hat{z} + \mathrm{M}_s \hat{z} \times \mathbf{h}e^{-i\omega t} + \\ \mathbf{m}e^{-i\omega t} \times \mathrm{H}_{\mathrm{ext}} \hat{z} + \mathbf{m}e^{-i\omega t} \times \mathbf{h}e^{-i\omega t}\end{array}\right) \tag{2.30}$$

m and **h** is oscillating magnetic dipole and magnetic field, respectively. The **m** and **h** are assumed to be small, thus their product can be ignored. Thus Eq. (2.1) can be solved as:

$$-i\omega\mathbf{m} = \hat{z} \times \left(-\omega_M \mathbf{h} + \omega_0 \mathbf{m} \right), \tag{2.31}$$

where

$$\omega_M = -\gamma\mu_0 M_s \text{ and } \omega_0 = -\gamma\mu_0 H_{ext} \tag{2.32}$$

solving the linearized torque equation (Eq.(2.31)) for **m** gives

$$\begin{pmatrix} m_x \\ m_y \end{pmatrix} = \begin{pmatrix} \chi & i\kappa \\ -i\kappa & \chi \end{pmatrix} \begin{pmatrix} h_x \\ h_y \end{pmatrix} \tag{2.33}$$

where

$$\chi = \frac{\omega_M\omega_0}{(\omega_0^2 - \omega^2)} \text{ and } \kappa = \frac{\omega_M\omega}{(\omega_0^2 - \omega^2)} \tag{2.34}$$

The magnetic susceptibility tensor can be identified from Eq.(2.33)

$$\bar{\chi} = \begin{bmatrix} \chi & i\kappa \\ -i\kappa & \chi \end{bmatrix} \tag{2.35}$$

Thus, inserting above equation to (Eq. (2.26)), we can be obtained the permeability tensor:

$$\bar{\mu} = \mu_0 \begin{bmatrix} 1+\chi & -i\kappa & 0 \\ i\kappa & 1+\chi & 0 \\ 0 & 0 & 1 \end{bmatrix} \tag{2.36}$$

The basic equation for magnetostatic wave should be satisfy Maxwell's equation magnetostatic limit in the absence of current, which read:

$$\nabla \times \mathbf{h} = 0 , \tag{2.37}$$

$$\nabla \cdot \mathbf{b} = 0 , \tag{2.38}$$

where

$$\mathbf{b} = \bar{\mu} \cdot \mathbf{h} , \tag{2.39}$$

Moreover, the magnetic field **h** can be expressed by *magnetostatic scalar potential* ψ [79]:

$$\mathbf{h} = -\nabla\psi \tag{2.40}$$

Combining Eqs. (2.38), (2.39), and (2.40) gives

$$\nabla \cdot \left(\bar{\mu} \cdot \nabla\psi\bar{\mu} \right) = 0 \tag{2.41}$$
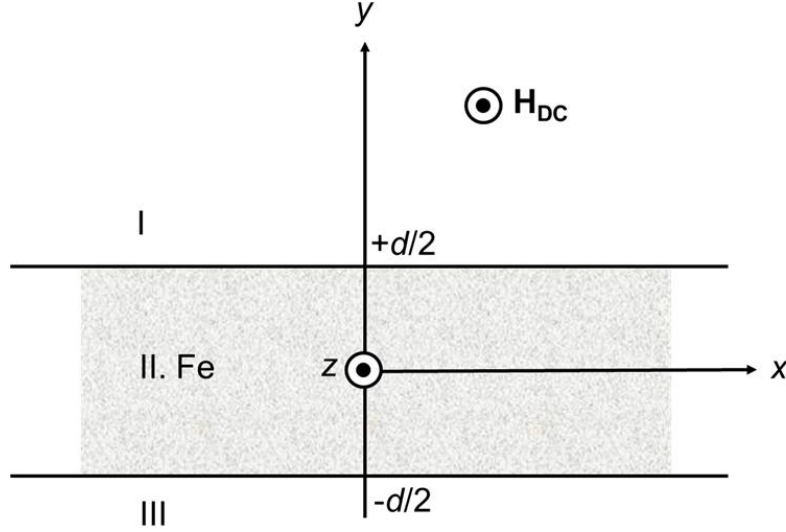
Figure 2.3: Geometry for magnetostatic surface spin wave (MSSW) dispersion relation analysis

This equation can be expanded by using Eq. (2.26) and (2.36) to obtain

$$(1+\chi)\left[\frac{\partial^2\psi}{\partial x^2}+\frac{\partial^2\psi}{\partial y^2}\right]+\left[\frac{\partial^2\psi}{\partial z^2}\right]=0 \tag{2.42}$$

above equation is called Walker equation, which describing magnetostatic mode propagation in homogeneous media. This equation can be used to find dispersion relation, $\omega(k)$, by considering boundary condition in the propagating medium.

- **Dispersion relation of magnetostatic surface spin wave (MSSW)**

  In this section dispersion relation $\omega(k)$ of MSSW is derived. Figure 2.3 shows the geometry that used for the analysis. Considering the material, i.e. Fe thin film, is located in the region II, while top and bottom areas are denoted as region II and III, respectively. Here, for simplicity we assumed the film are isotropic. The external magnetic field (H_{ext}) and magnetization (M_s) of the Fe-thin film are lying in z-direction, thus for the MSSW mode, the k should be propagating along $\pm x$. We assume the potential to be proportional to $\exp(ivk_x x)$, where $v=\pm1$. Now, as a trial solution, the potential at each region can be defined as:

$$\psi_I(r) = Ce^{-k_x y + ivk_x x}, \tag{2.43}$$

$$\psi_{II}(r) = \psi_0 \cos(k_y y)e^{ivk_x x}, \tag{2.44}$$

$$\psi_{III}(r) = De^{k_x y + ivk_x x} \tag{2.45}$$

37

Thus, for region II, Walker's equation (2.42) can be reduces to

$$(1+\chi)(k_x^2 + k_y^2) = 0 \tag{2.46}$$

A possible solution to this equation is $(1+\chi) = 0$. However, this only for one specific frequency. Therefore, we use $k_x^2 = -k_y^2$ for the solution. Suppose k_x to be real for propagating waves, then k_y must be imaginary. Thus, in region II, potential must have growing and decaying exponentials:

$$\psi_{II}(r) = \left[\psi_{0+} e^{ky} + \psi_{0-} e^{-ky}\right] e^{i\nu kx}, \tag{2.47}$$

Note, wave number subscript have dropped to k.

Next, we apply the boundary condition. At $y = \pm d/2$, ψ must be continuous :

$$C\, e^{-kd/2} = \psi_{0+} e^{kd/2} + \psi_{0-} e^{-kd/2}, \tag{2.48}$$

$$D\, e^{-kd/2} = \psi_{0+} e^{-kd/2} + \psi_{0-} e^{kd/2}, \tag{2.49}$$

The remaining boundary condition required the normal magnetic flux density **b** to be continuous at $y = \pm d/2$. The y component of magnetic flux density in y axis can be expressed as:

$$b_y = \nabla_y \psi \ \text{(in the region I and III)} \tag{2.50}$$

$$b_y = i\kappa \nabla_x \psi + (1+\chi)\nabla_y \psi \ \text{(in the region II)} \tag{2.51}$$

Thus, requiring b_y to be continuous at $y = \pm d/2$ gives

$$C\, e^{-kd/2} = \nu\kappa\left[\psi_{0+} e^{kd/2} + \psi_{0-} e^{-kd/2}\right] - (1+\chi)\left[\psi_{0+} e^{-kd/2} + \psi_{0-} e^{+kd/2}\right] \tag{2.52}$$

$$D\, e^{-kd/2} = -\nu\kappa\left[\psi_{0+} e^{-kd/2} + \psi_{0-} e^{kd/2}\right] + (1+\chi)\left[\psi_{0+} e^{-kd/2} + \psi_{0-} e^{+kd/2}\right] \tag{2.53}$$

Substituting eqs.(2.48) and (2.49) to eqs. (2.52) and (2.53) consecutively, and collecting the terms, we obtained:

$$\begin{bmatrix} (\chi+2-\nu\kappa)e^{kd/2} & -(\chi+\nu\kappa)e^{-kd/2} \\ -(\chi-\nu\kappa)e^{-kd/2} & (\chi+2+\nu\kappa)e^{kd/2} \end{bmatrix} \begin{bmatrix} \psi_{0+} \\ \psi_{0-} \end{bmatrix} = 0 \tag{2.54}$$

The dispersion relation can be obtained when the determinant of the coefficient matrix to zero:

38

$$e^{-2kd} = \frac{(\chi + 2)^2 - \kappa^2}{\chi^2 - \kappa^2} \tag{2.55}$$

It is noteworthy that dependence on v vanished, suggesting that the dispersion relation doesn't change if the propagation direction is reversed. Insert χ and κ from Eq. (2.34) and solving for ω^2, we can obtain

$$\omega^2 = \omega_0(\omega_0 + \omega_M) + \frac{\omega_M^2}{4}\left[1 - e^{-2kd}\right] \tag{2.56}$$

This equation is known as basic dispersion relation of magnetostatic surface spin waves (MSSW).

In a real case i.e. the surrounding material of Fe and magnetic anisotropy of Fe is not isotropic, the permeability tensor $\bar{\chi}$ must be derived again from LL-equation lead to different expression in dispersion relation. In frequency form it can be express as [80],[69]:

$$f_R = -\frac{\mu_0 \gamma_0}{2\pi} \sqrt{\begin{array}{l}\left(|H_{ext}| + H_{cry}\right)\left(|H_{ext}| + M_S + H_{cry} - H_{int}\right) \\ + \frac{M_S}{4}(M_S - H_{int})\left(1 - \exp\left(-2|k|t_{Fe}\right)\right)\end{array}} \tag{2.57}$$

Above equation take account the contribution from fourfold crystalline magnetic anisotropy field (H_{cry}) and interfacial-perpendicular magnetic anisotropy field (H_{int}). The effective field (H_{eff}) can be expressed as:

$$H_{eff} = H_{ext}\hat{z} + \frac{\mu_0}{2}\begin{pmatrix} H_{cry} \\ H_{cry} + M_s - H_{int} \end{pmatrix}\vec{m}e^{-i\omega t} + \vec{h}e^{-i\omega t} \tag{2.58}$$

Moreover, by including the DMI contribution, D, the dispersion relation can be written [81]:

$$f_R = -\frac{\mu_0 \gamma_0}{2\pi} \sqrt{\begin{array}{l}\left(|H_{ext}| + H_{cry}\right)\left(|H_{ext}| + M_S + H_{cry} - H_{int}(V_{DC})\right) \\ + \frac{M_S}{4}(M_S - H_{int}(V_{DC}))\left(1 - e\left(-2|k|t_{Fe}\right)\right)\end{array}} \mp \frac{\gamma_0}{\pi}\frac{D(V_{DC})k}{M_S} \tag{2.59}$$

In this study we use above equation to analyze VCMA and VDMI from MSSW resonance.

- **Voltage-induced frequency shift**

In our experiment, the resonance frequency of MSSW is measured under voltage-application. From Eq. (2.59), two properties were considered to be modulated by voltage application, H_{int}, and D. In this subsection, we derived the equation that use to independently

analysis the voltage-induced frequency shifts of spin-wave resonance attributing to interfacial-perpendicular magnetic anisotropy change (VCMA) and interfacial-Dzyaloshinskii-Moriya interaction (VCDMI).

The measurement was conducted using two antennas (antennas 1 and 2), the propagation of spin-wave direction $+k$, if antenna 2 acted as receiver (denoted as 21) while $-k$, if antenna 1 acted as receiver (denoted as 12). When voltage is applied, small frequency shift induced can be written as:

$$f_{R} + \delta f_{21} = -\frac{\mu_0 \gamma_0}{2\pi} \sqrt{\begin{array}{c}\left(|H_{ext}| + H_{cry}\right)\left(|H_{ext}| + M_S + H_{cry} - H_{int} - \delta H_{int}\right) \\ +\frac{M_S}{4}\left(M_S - H_{int} - \delta H_{int}\right)\left(1 - e\left(-2|k|t_{Fe}\right)\right)\end{array}} - \frac{\gamma_0 \delta D k}{\pi M_S} \quad (2.60)$$

$$f_{R} + \delta f_{12} = -\frac{\mu_0 \gamma_0}{2\pi} \sqrt{\begin{array}{c}\left(|H_{ext}| + H_{cry}\right)\left(|H_{ext}| + M_S + H_{cry} - H_{int} - \delta H_{int}\right) \\ +\frac{M_S}{4}\left(M_S - H_{int} - \delta H_{int}\right)\left(1 - e\left(-2|k|t_{Fe}\right)\right)\end{array}} + \frac{\gamma_0 \delta D k}{\pi M_S} \quad (2.61)$$

Above equation represent the small frequency shift in $+k$ (δf_{21}) and $-k$ (δf_{12}) directions. Summation of these two equation gives:

$$2f_{R} + \delta f_{21} + \delta f_{12} = -2\frac{\mu_0 \gamma_0}{2\pi} \sqrt{\begin{array}{c}\left(|H_{ext}| + H_{cry}\right)\left(|H_{ext}| + M_S + H_{cry} - H_{int}\right) + \\ \frac{M_S}{4}\left(M_S - H_{int} - \delta H_{int}\right)\left(1 - e\left(-2|k|t_{Fe}\right)\right) - \\ \delta H_{int}\left(|H_{ext}| + H_{cry} + \frac{M_S}{4}\left(1 - e\left(-2|k|t_{Fe}\right)\right)\right)\end{array}} \quad (2.62)$$

Note that the DMI term has vanish. Next, replacing f_R without DMI term to Eq. (2.62), we obtain:

$$2f_{R} + \delta f_{21} + \delta f_{12} = -2\frac{\mu_0 \gamma_0}{2\pi} \sqrt{\frac{f_{R}^{2}}{\left(\mu_0 \gamma_0 / 2\pi\right)^2}\left(1 - \frac{\delta H_{int}\left(|H_{ext}| + H_{cry} + \frac{M_S}{4}\left(1 - e\left(-2|k|t_{Fe}\right)\right)\right)\left(\mu_0 \gamma_0 / 2\pi\right)^2}{f_{R}^{2}}\right)} \quad (2.63)$$

$$2f_{R} + \delta f_{21} + \delta f_{12} = 2f_{R} \sqrt{1 - \frac{\delta H_{int}\left(|H_{ext}| + H_{cry} + \frac{M_S}{4}\left(1 - e\left(-2|k|t_{Fe}\right)\right)\right)\left(\mu_0 \gamma_0 / 2\pi\right)^2}{f_{R}^{2}}} \quad (2.64)$$

The term in the square can be approximated using Taylor expansion. Then, Eq. (2.64) can be written as:

$$2f_{\mathrm{R}}+\delta f_{21}+\delta f_{12} \cong 2f_{\mathrm{R}}\left(1-\frac{\delta H_{\mathrm{int}}\left(|H_{\mathrm{ext}}|+H_{\mathrm{cry}}+\frac{M_{\mathrm{S}}}{4}\left(1-e(-2|k|t_{\mathrm{Fe}})\right)\right)\left(\mu_0\gamma_0/2\pi\right)^2}{2f_{\mathrm{R}}^2}\right) \tag{2.65}$$

Thus

$$\delta f_{21}+\delta f_{12} \cong -\frac{\delta H_{\mathrm{int}}\left(|H_{\mathrm{ext}}|+H_{\mathrm{cry}}+\frac{M_{\mathrm{S}}}{4}\left(1-e\left(-2|k|t_{\mathrm{Fe}}\right)\right)\right)\left(\mu_0\gamma_0/2\pi\right)^2}{f_{\mathrm{R}}} \tag{2.66}$$

Solving above equation for δH_{int}, we obtain

$$\delta H_{\mathrm{int}} \cong -\frac{f_{\mathrm{R}}\left(\delta f_{21}+\delta f_{12}\right)}{\left(|H_{\mathrm{ext}}|+H_{\mathrm{cry}}+\frac{M_{\mathrm{S}}}{4}\left(1-e\left(-2|k|t_{\mathrm{Fe}}\right)\right)\right)\left(\mu_0\gamma_0/2\pi\right)^2} \tag{2.67}$$

The VCMA energy can be calculate:

$$\xi_{\mathrm{VCMA}} = \frac{1}{2}\frac{\mu_0 M_{\mathrm{S}}t_{\mathrm{Fe}}}{E_{\mathrm{MgO}}}\delta H_{\mathrm{int}} \tag{2.68}$$

Inserting δH_{int} from eq. (2.67), we get:

$$\xi_{\mathrm{VCMA}} \cong -\frac{M_{\mathrm{S}}t_{\mathrm{Fe}}}{\mu_0 E_{\mathrm{MgO}}}\frac{\left(\frac{2\pi}{\gamma_0}\right)^2 f_{\mathrm{R}}\left(\frac{\delta f_{21}+\delta f_{12}}{2}\right)}{\left(H_{\mathrm{ext}}+H_{\mathrm{cry}}+\frac{M_{\mathrm{S}}}{4}\left(1-e^{-2kt_{\mathrm{Fe}}}\right)\right)} \tag{2.69}$$

This equation is used to calculate VCMA.

Next, the VCDMI energy is derive. Subtracting Eq. (2.60) and (2.61), we obtained:

$$f_{\mathrm{R}}+\delta f_{21}-\left(f_{\mathrm{R}}+\delta f_{12}\right)=\delta f_{21}-\delta f_{12}=-2\frac{\gamma_0\delta Dk}{\pi M_{\mathrm{S}}} \tag{2.70}$$

The change in i-DMI energy, D, due to voltage application can be represent as:

$$\delta D = -\frac{1}{2}\frac{\pi M_{\mathrm{S}}}{\gamma_0 k}\left(\delta f_{21}-\delta f_{12}\right) \tag{2.71}$$

Normalized this equation to electric field, we can obtain i-DMI energy change. The VCDMI can be expressed as:

$$\xi_{\mathrm{iDMI}} = -\frac{\pi}{\gamma_0}\frac{M_{\mathrm{S}}}{E_{\mathrm{MgO}}k}\left(\frac{\delta f_{21}-\delta f_{12}}{2}\right) \tag{2.72}$$
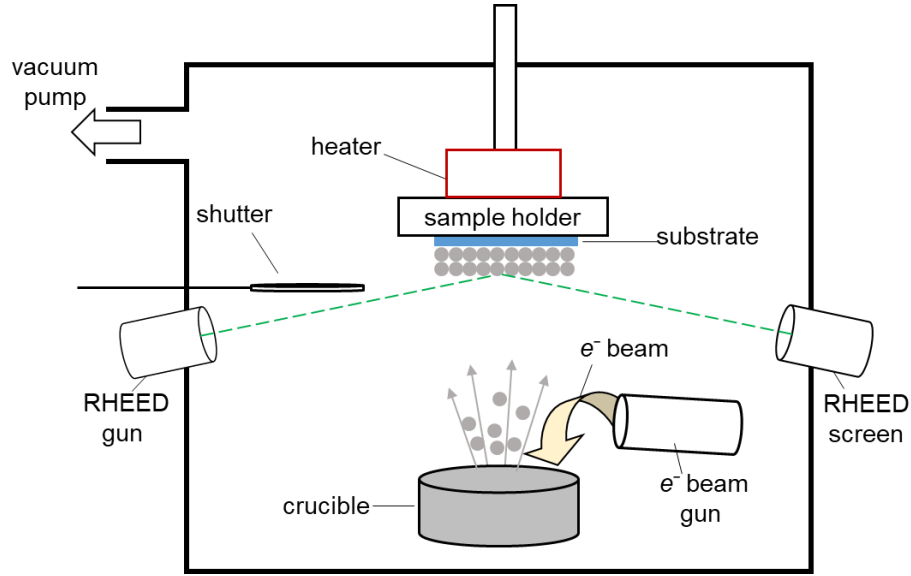
Figure 2.4: Schematic of molecular-beam epitaxy with electron-gun evaporation system.

2.2. Experimental Method

2.2.1. Device Fabrication

The sample, which consists of multilayer thin film, was fabricated through molecular-beam epitaxy (MBE) deposition and RF-magnetron sputtering deposition. The MBE is employed to form the epitaxial deposition. Figure 2.4 illustrates MBE schematic. There are two main aspects in MBE deposition. First, the deposition takes place in ultra-high vacuum (typically 10^{-8}-10^{-12} Torr). Second, the deposition rate is low (typically less than 3000 nm/hour) to allow film grow epitaxially. In solid source MBE, target elements in ultra-pure form are heated by electron-beam evaporators or Knudsen effusion cells. We employed electron-beam to sublime for all materials target which used in this study. The chamber is connected to
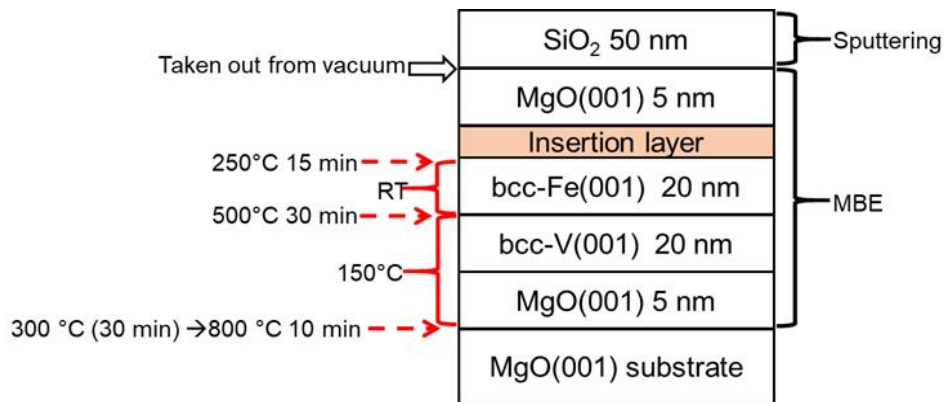
Figure 2.5: The schematic of multilayer film deposited by molecular beam epitaxy and rf-magnetron sputtering.

Table 2.1 Material in MBE deposition and its bulk crystalline properties

Material [Ref.]	Bulk crystal structure	Lattice constant (Å)	Density (g/cm^3)
MgO [82]	NaCl-type cubic	$a = 4.13$	3.57
V [83]	body-centered cubic (bcc)	$a = 3.02$	6.11
Fe [84]	bcc	$a = 2.87$	7.88
Co [85]	hexagonal close-packed (hcp)	$a = 2.51, c = 4.07$	8.84
Ni [86]	fcc	$a = 3.53$	8.9
Pd [87]	face-centered cubic (fcc)	$a = 3.89$	12.01
Ir [88]	fcc	$a = 3.84$	22.56

the vacuum systems (consist of turbo molecular pump (TMP), rotary-pump (RP) and ion pump) to achieve the base pressure in the growth chamber to be less than 4×10^{-8} Pa. It is also being equipped by computer-control shutter and substrate heater which allows us to control of deposition condition. Moreover, the thickness and quality of single crystal growth were monitored by crystal oscillator and reflection high-energy electron diffraction (RHEED).

The target materials which been used in MBE deposition are listed in Table 2.1. In this study, we used three kinds of ferromagnetic (FM) 3d-metals; Fe, Co, and Ni. Furthermore, 4d-material Pd and 5d-material Ir also are being used. Figure 2.5 shows the multilayer stacking and fabrication condition. As a substrate, we used single-crystalline NaCl-type MgO. Before film deposition, the MgO substrate was pre-annealed at 300 °C for 30 min and 800 °C for 10 min. After that, we deposited 5-nm MgO at 150 °C (dep. rate: 0.1 Å/s) to prevent the impurity material diffusion, such as carbon, from MgO substrate [89]. Then, V-layer was deposited at 150 °C with dep. rate 0.2 Å/s and then post-annealed at 300 °C for 30 min. The V-layer is used as under-layer to minimize the lattice-mismatch in Fe-layer growth. After that, Fe was grown at room temperature (dep. rate: 0.1 Å/s). To obtain a flat surface, in situ post-annealing was conducted at 250 °C for 15 min. Figure 2.6 shows reflection high-energy electron diffraction image of 20-nm Fe indicating the improvement of Fe-surface crystallinity after post-annealing. No annealing was conducted after this step to ensure no diffusion in occurs in the sample. After that, ultra-thin insertion layer was deposited. In this study, we employed several materials to be inserted in between Fe/MgO layer; Co, Ni, Pd, and Ir. To control the thickness of the insertion layer, the auto-shutter had been used. The details of the ultra-thin layer insertion deposition procedure are explained in each sections. After the insertion layer deposition, another 5-nm-MgO was grown. Then the sample was being taken out from MBE chamber

<center>(a)   (b)</center>
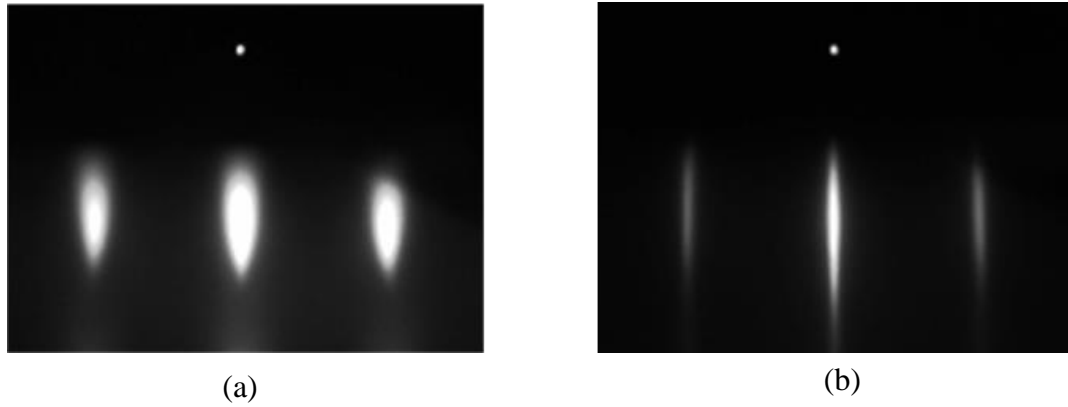
Figure 2.6: Reflection high-energy electron diffraction image of Fe 20 nm parallel to MgO [100] plane, a) before post-anneal, b). after in situ post-anneal 250 °C 15 min. Streak line indicates flatter surface

(exposed to air) and being transfer to sputtering chamber. In sputtering, we deposited 5-nm SiO_2 to prevent further oxidation to the sample. In the finished sample, another 45-nm SiO_2 was deposited as additional insulating layer by sputtering during microfabrication process.

To conduct the spin-wave spectroscopy by electrical measurement, the microfabrication was conducted to pattern the sample. Figure 2.7 illustrates the spin wave device. The multilayer film was patterned into a rectangular shape (100×400 μm) with the long axis parallel to the Fe [100] direction. Two antennas (short-circuit coplanar waveguide) composed of Cr (5 nm)/Au (200 nm) films were fabricated parallel to the Fe [100] direction through a lift-off process. It consists of a signal line (2 μm) and two ground lines (1 μm) with gaps of 1 μm, and an intermediate gate electrode between the antennas. The two antennas separated by 10 μm. To apply the voltage, a contact pad was fabricated by etching down the film until the Fe-layer.

The spin wave device was fabricated through electron-beam (EB) lithography, Ar+ milling and electron-beam deposition. The details step as follows:

1. Cross-mark

   Figure 2.8(a) shows cross-mark pattern which use for EB-registration mark. After the multilayer deposition, the sample cleaned by IPA and iso-propanol solution. After clean, a negative tone resist, (ZEP520 resist with approx. 200 nm thick) was coated onto the sample through spin coater. The sample then was pre-baked at 180 °C for 90 sec. To avoid the charge-up during EB-exposure, a conducting layer, espacer, was coated to the sample. EB-drawing then was conducted to hardness the resist. After resist development, 5-nm Cr

<center>44</center>
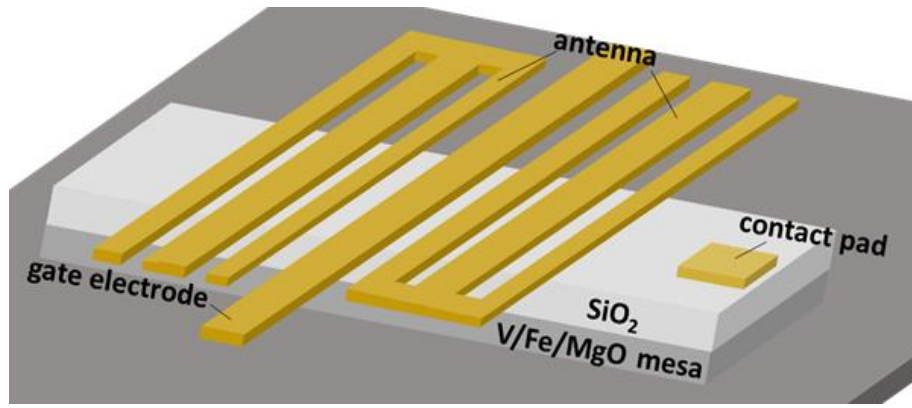
Figure 2.7: Schematic of spin-wave device. It consists of a multilayer film wire (100 x 400 μm), two micro-sized antennas and an intermediate gate electrode. The two antennas separated by 10 μm. Each antenna consists of a signal line (2 μm) and two ground lines (1 μm) with gaps of 1 μm, and an intermediate gate electrode between the antennas. A contact pad connected to Fe-layer.

and 70-nm Au were deposited. Finally, the remaining the resist was removed through lift of process.

2. Wire pattern

   The multilayer film was patterned into a rectangular shape (100 × 400 μm) with the long axis parallel to the Fe[100] direction as depicted in Figure 2.8(b). For this pattern, EB-lithography process used positive tone resist (TGMR-360) coated onto the sample. The sample then was pre-baked at 130 °C for 90 sec. After EB-drawing, for development the resist post-baked (at 110 °C for 90 second) was necessary. Then, the film was etched down to the MgO bottom layer. Before lift off the resist, 20-nm SiO_2 was sputtered to avoid oxidation in Fe-layer. It should be noted, the thickness of SiO_2 should not more than 20-nm, because the removal of the resist becomes difficult.

3. Deposit additional insulator SiO_2 layer (45 nm)

   After lift-off the resist, 45-nm SiO_2 was grown to the film by using sputtering. This layer was fabricated as additional insulating layer for voltage measurement.

4. Edge pattern
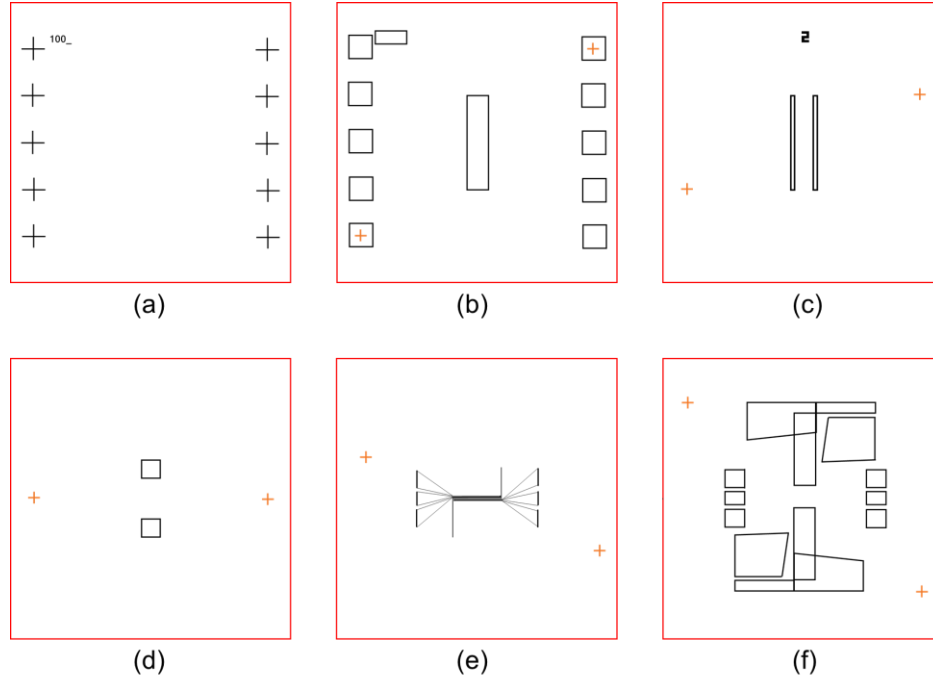
Figure 2.8: Schematic of the patterns which used for EB-lithography drawing. (a) Registration mark, (b) wire, (c) Edge, (d) hole, (e) antenna 1 and (f) antenna 2.

To increase the endurance and avoid breakdown of the sample during the voltage-bias, at the edge of wire-pattern, 20-nm SiO_2 was deposited by sputtering. Figure 2.8(c) shows the pattern which used for EB-drawing. For this step, we used ZEP-520 for the resist.

5. Hole pattern

To apply voltage perpendicularly to the film, a conduction lane must be formed to the bottom of conduction layer. The film was etched down to the Fe-layer using Ar^+ milling after EB-drawing of hole-pattern (see Figure 2.8(d)). After that the resist was removed through lift-off process.

6. Antenna pattern

Two antennas and an intermediate gate electrode were fabricated using pattern as shown in Figure 2.8(e) and (f). In this process, two times EB-drawing were conducted. After resist development, 5-nm Cr and 200 nm Au were deposited by electron-beam deposition. After that the resist was removed through lift-off process. Figure 2.9 shows the top view of finish device.
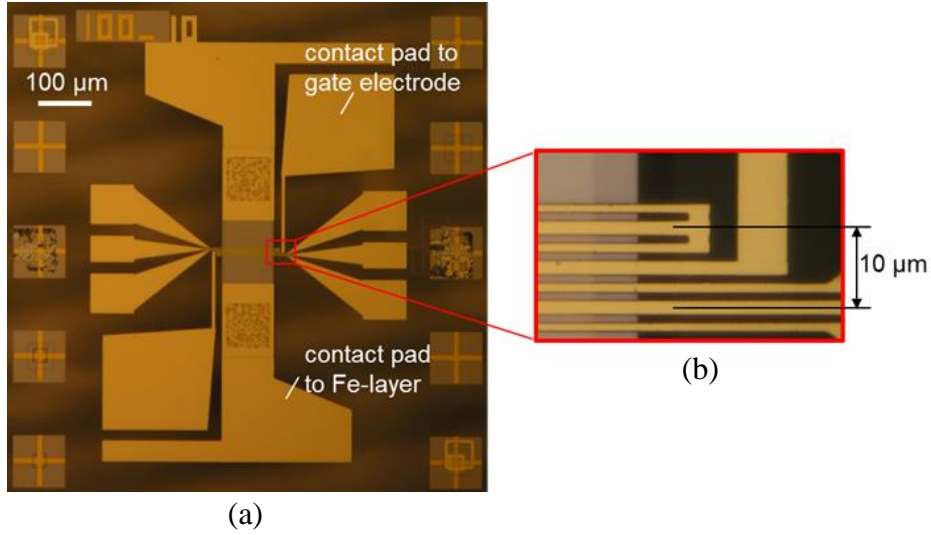
Figure 2.9: (a) Top view off final spin-wave device, and (b) magnify image of antennas

After finish the microfabrication, some samples were being annealed intentionally. This treatment was done only for Co/Pd insertions sample and Ir-insertion sample. The purpose of post-annealing is to induce atomic re-arrangement at Fe/MgO interface. Thin layer insertions are expected to react to post-annealing. It can be a relaxation of stress or diffusion that mediated VCMA and VCDMI enhancement. The post-annealed was conducted inside a chamber with base pressure $< 4 \times 10^{-4}$ Pa, at several annealing temperatures for 30 minutes. No magnetic field or ambient gas was applied during annealing.

2.2.2. Device characterization

The spin wave device had been fabricated into spin-wave device which includes the antennas as a coplanar wave-guide, an intermediate electrode and a contact pad to bottom Fe to apply voltage across the film. The measurement was conducted by acquired the microwave response from the multilayer under external magnetic field and/or under voltage-bias. In this section the spin-wave signal observation and its modulation for characterization of anisotropy field (H_{int} and H_{cry}), magnetic anisotropy change (VCMA) and interfacial Dzyaloshinskii-Moriya interaction (VCDMI) will be explained.

To measure voltage-effects in ferromagnetic-metal, usually an ultra-thin layer (< 1 nm) was used, investigated through changing in magnetization hysteresis. In thicker film, this change is too small to analyze. The voltage-effects characterization by spin-wave spectroscopy
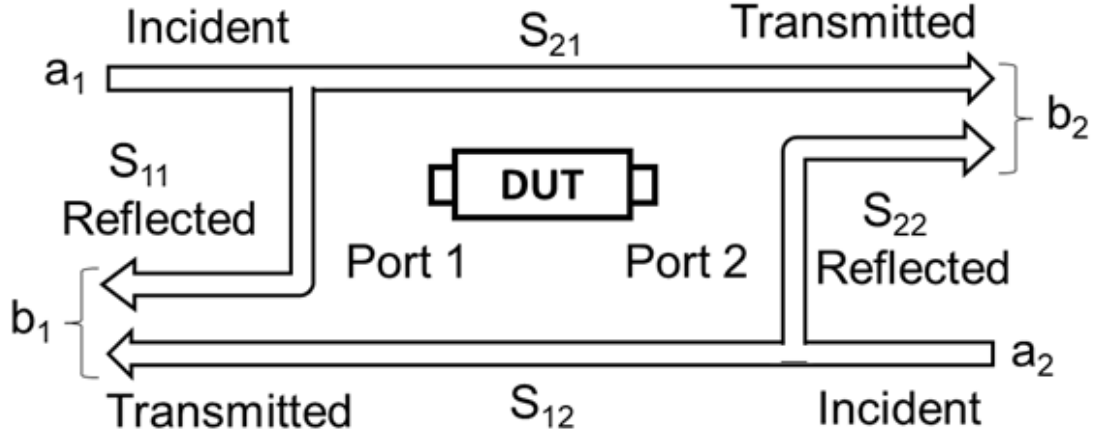
Figure 2.10: Schematic relation between the *S*-parameters, incident wave (a_i) and outgoing wave (b_i) in the two-ports measurement. DUT is stand for the device under test, in our case is correspond to spin-wave device. Picture reproduced after [90]

can overcome this issue. This technique was developed in our group by previous student K. Nawaoka [69].

The vector network analyzer measures the microwave response of the sample in the formed of scattering parameter which also called, *S*-parameter. The total number of *S*-parameter is equal to the square of the number of ports. In our experiment, two ports are being used, thus it has four *S*-parameters. The convention for *S*-parameters numbering is that the first number following the S is the port of radio-frequency power leaving the sample and the second number is the port where the radio-frequency is entering the sample. For example, the S_{21} is measure of power from port 2 as the result of applying the radio-frequency power in port 1. The schematic of relation between, the incident wave (a_i), the out-going wave (b_i) and the *S*-parameters is illustrated in Figure 2.10. For two ports measurement and thus four *S*-parameters, the relation can be expressed as:

$$\begin{pmatrix} b_1 \\ b_2 \end{pmatrix} = \begin{bmatrix} S_{11} & S_{12} \\ S_{21} & S_{22} \end{bmatrix} \begin{pmatrix} a_1 \\ a_2 \end{pmatrix} \tag{2.73}$$

when the radio-frequency power only come from one port and another port is terminated, each S_{ij} parameter is the ratio between the outgoing wave (b_i) at port i and the incident wave (a_j) at the port j [91].
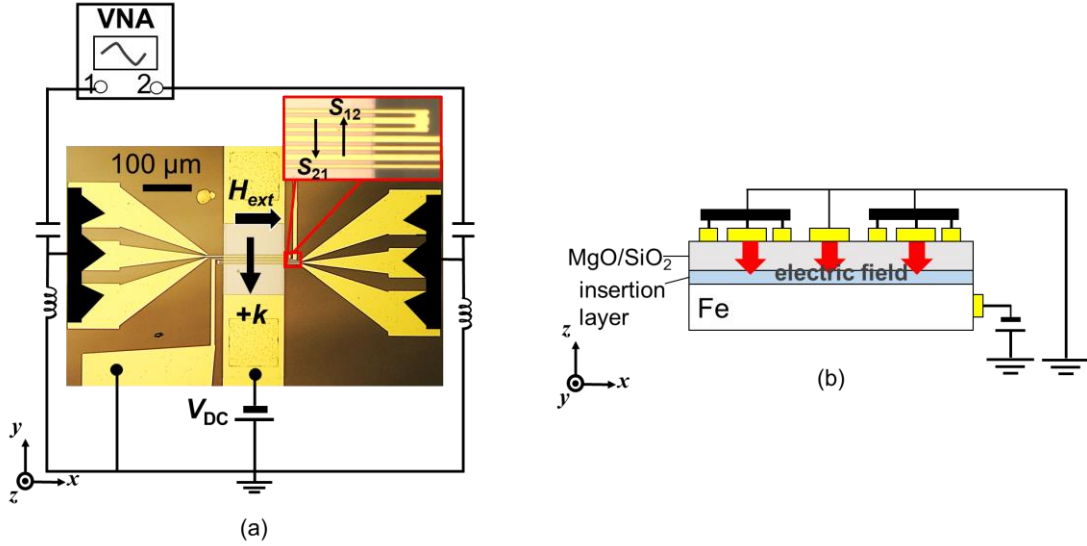
Figure 2.11: (a) Measurement circuit to detect a spin wave signal. The antennas are connected to vector network analyzer (VNA) by GSG probe. External voltage (V_{DC}) is applied from source meter via dc-probe connecting to contact pad and intermediate gate electrode. An external magnetic field (H_{ext}) is applied in in-plane direction. Two bias-tee are used to protect the vector network analyzer from electrostatic charge. Vector network analyzer and source meter are connected to the same ground via bias-tee. (b) Schematic of electric field which applied perpendicularly across the multilayer.

Figure 2.11(a) shows the schematic of the measurement set-up. Both antennas are connected to vector network analyzer through coaxial cable, k-connector, and microwave-GSG probe. Source meter are connected to contact pad (conduction path to Fe-layer) and intermediate gate electrode via dc-probe. Two bias-tee are used to protect vector network analyzer from electrostatic charge. Vector network analyzer and source meter are connected to same ground via bias-tee. The micro-size antenna functions as coplanar waveguide. Two antennas separated by 10 μm and has short-end as shown in Figure 2.9(b). It has non-uniform spatial distribution of magnetic field resulted from current flow in the antenna as depicted in Figure 2.12(a). By this antenna design, the selected wave number has the main peak at wave number, $k = 1.2$ μm (see Figure 2.12(b)), while other smaller peak was also observed in other higher k. The two ports vector network analyzer measurement is employed to detect the microwave response from the spin-wave device. The vector network analyzer can generate microwave incident signal with wide range of frequency. In our vector network analyzer, the frequency range is between 10 MHz to 50 GHz.
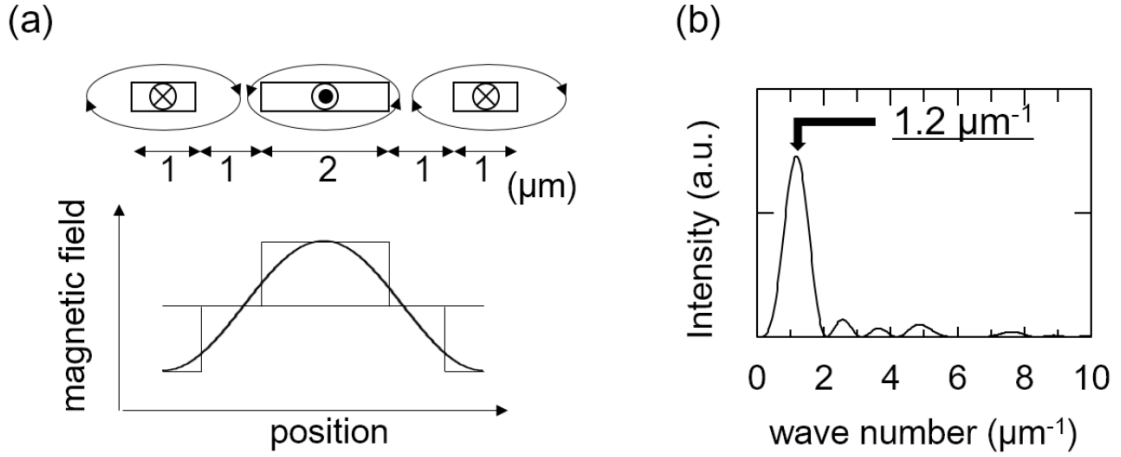
Figure 2.12: (a) magnetic field distribution in the designed antenna, (b) Fourier transfer of spatial distribution in (a). Picture are taken from [80]

In this study, two kinds of measurements were done. First, so called spin-wave nature measurement to evaluate the magnetic anisotropy properties. This magnetic anisotropy measurement was carried out by sweeping external magnetic field (H_{ext}) without application of bias voltage. Second, the voltage-modulation spin-wave measurement by applying external voltage across the sample with fix applied external magnetic field (H_{ext}). The first part of measurement will be explained.

- **Magnetic anisotropy field characterization**

To evaluate the magnetic anisotropy field, spin wave measurement was conducted by applying external magnetic field ($\mu_0 H_{ext}$) without of external voltage bias ($V_{DC} = 0$). The experiment set-up is depicted in Figure 2.11. For this measurement, frequency range in vector network analyzer was set to 10 - 20 GHz. RF power of -15 dBm (32 μW) with 1 kHz bandwidth. At first, large external magnetic field ($\mu_0 H_{ext}$ = 270 mT) was applied to saturate the magnetization of Fe in in-plane direction x. The spectrum at large magnetic field is also used as a background signal. Then, spectra at smaller magnetic field H_{ext} was captured, in the range 0 to 100 mT. For each applying magnetic field signal was being taken 10 times and then been averaged.

Figure 2.13(a) shows the S_{11} reflection from three different external magnetic fields $\mu_0 H_{ext}$ = 40, 60 and 80 mT. One can see the signal are deviated from Lorentzian form in higher frequency region, which may attribute to harmonic product of k-selection. The signal then
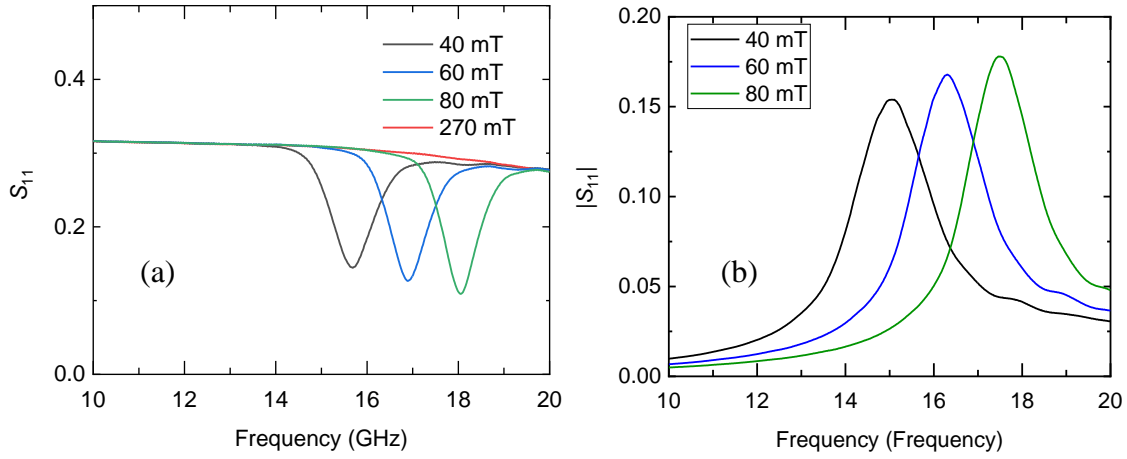
Figure 2.13: (a) Typical S_{11} reflectance from spin-wave measurement. Signal at $\mu_0 H_{ext}$ =270 mT are used as background (b) normalized signal after subtracting signal with background signal at $\mu_0 H_{ext}$ =270 mT. $|S_{11}| = | S_{11}(H_{ext}) - S_{11,BG}(270 \text{ mT})|$
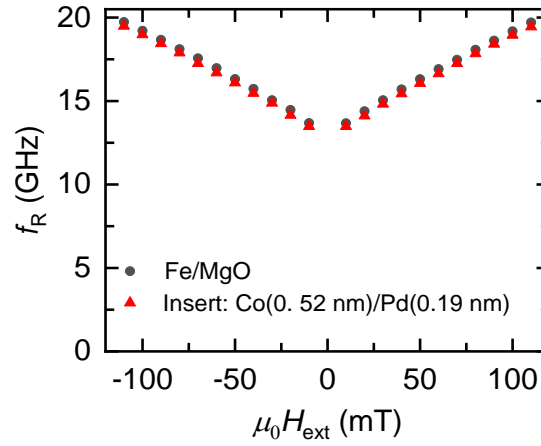
Figure 2.14: Spin wave-resonant frequency as different applied external magnetic field H_{ext}. The results from two sample are shown: Fe/MgO (black) and Fe/Co(0.52 nm)/Pd(0.19 nm)/MgO (red).

normalized with background signal from $\mu_0 H_{ext}$ = 270 mT. Figure 2.13(b) shows the normalized signal $|S_{11}| = | S_{11}(H_{ext}) - S_{11,BG}(270 \text{ mT})|$. The spin-wave resonance frequency (f_R) is determined from the frequency of normalized signal peaks.

Then, each resonance frequencies (f_R) can be summarized for every applied external magnetic field H_{ext}. Figure 2.14 shows the resonance frequencies (f_R) for two samples: Fe/MgO and Fe/Co(0.52 nm)/Pd(0.19 nm)/MgO. It can be seen that the insertion affects the resonance frequencies (f_R) suggesting the change in the sample magnetic properties upon Co/Pd insertion to Fe/MgO interface. Now, we can extract the magnetic anisotropy properties from the resonance frequencies (f_R) using Eq. (2.59). One should be noted that the fitting ignored DMI
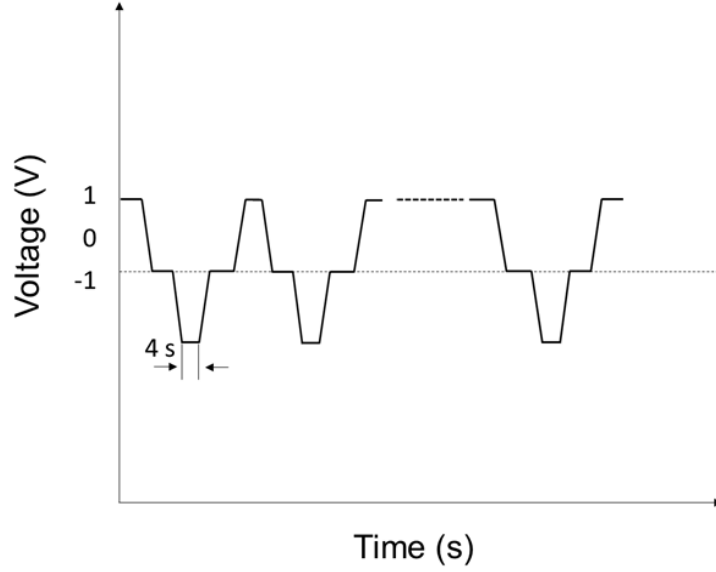
Figure 2.15: Schematic illustration of applying sweeping voltage at 1 V. One cycle defined as, 1 V – 0 V– (-1 V) – 0 V. Measurement for each voltage was done up to 600 cycle.

contribution in this case because no splitting was observed in S_{11}, suggesting DMI contribution out of measurement resolution (appx. 0.5 J/m^2 [80]).

- **Voltage-effects characterization**

    For characterization of voltage effect the measurement schematic is the same as previous section which depicted in Figure 2.11. The parameter in vector network analyzer is set to RF power of -15 dBm (32 µW) with 1 kHz bandwidth. The applied magnetic field $\mu_0 H_{ext}$ was fixed at 40 mT and external voltage (V_{DC}) was sweep up to 5 V. At first, again, large external magnetic field ($\mu_0 H_{ext}$) = 270 mT) was applied to saturate the magnetization of Fe in in-plane direction x. The frequency range of vector network analyzer is shortened to range of resonance of 40 mT.

    Figure 2.11(b) shows the schematic of electric field applied across the spin wave device. The electric field in MgO layer is responsible for the voltage-effect in underneath ferromagnet. To calculate the electric field, we can model the sample as two capacitors in series with dielectric constant of SiO$_2$ and MgO are ε_{SiO2} =3.9 and ε_{MgO} = 9.6, respectively. The electric field in the MgO layer estimated:

$$E_{MgO} = \left(\varepsilon_{SiO_2} / V_{DC} \right) / \left(\varepsilon_{SiO_2} d_{MgO} + \varepsilon_{MgO} d_{SiO_2} \right) \tag{2.74}$$

52
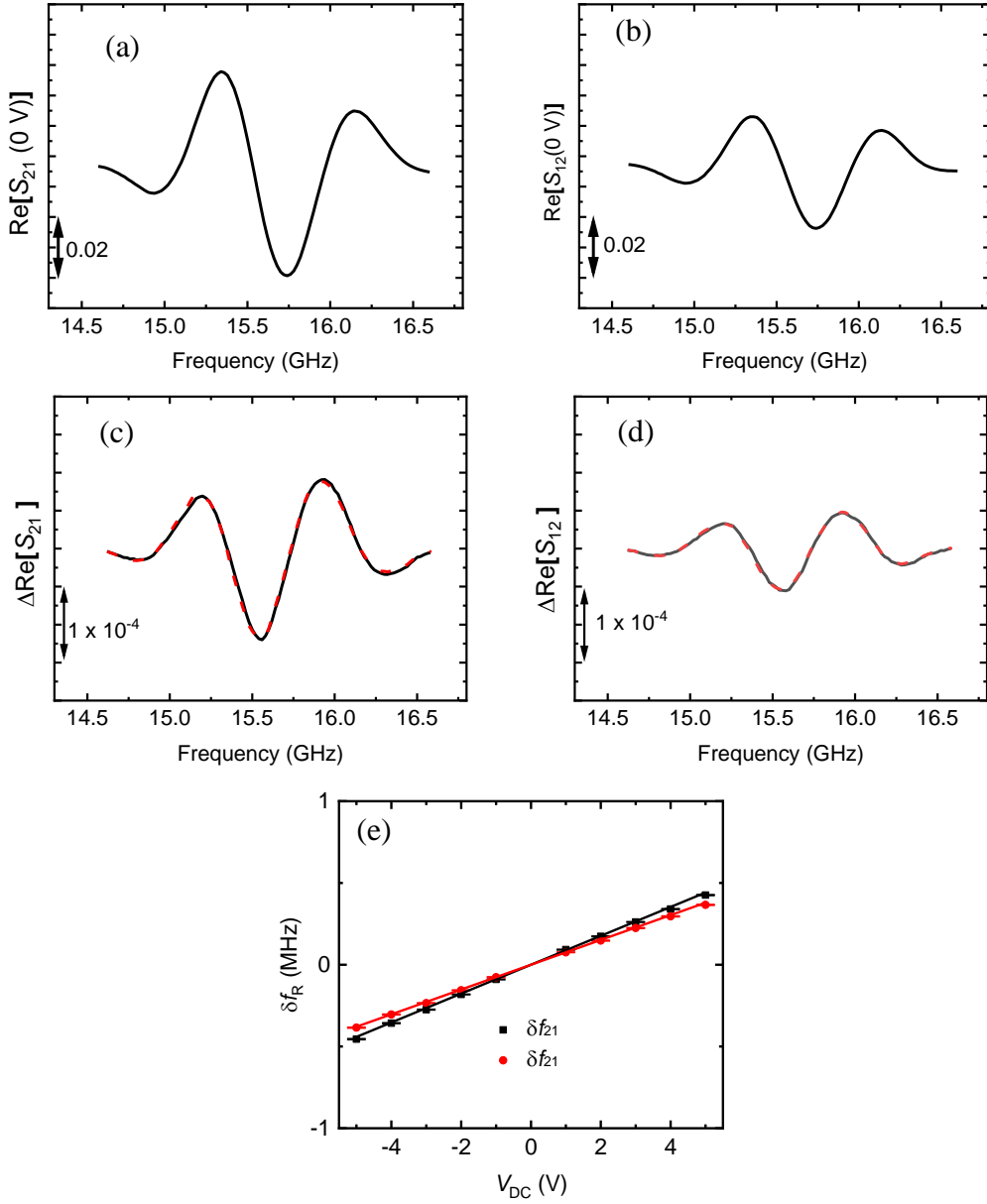
Figure 2.16: Spin wave propagating signal, (a) in S_{21} direction, (b) in 21 direction. (c) and (d) represent the subtracting signal: $Re[S_{21(12)}] = Re[S_{21(12)}(5\text{ V})] - Re[S_{21(12)}(0\text{ V})]$. Red line indicates fitting of voltage-induced frequency shift (δf_R). (e) Applied voltage dependent of δf_R. All the signal come from same sample without insertion layer Fe/MgO.

with d_{MgO} and d_{SiO_2} are being thickness of MgO and SiO2 layer, respectively. The electric field in MgO is calculated, 8 mV/nm at $V_{DC} = 1$ V. The scheme for applying voltage is shown in Figure 2.15. To elaborate, i.e. if we would like apply $V_{DC} = 1$V, for one cycle of measurement, $V_{DC} = 1$ V $\rightarrow 0_{down}$ V $\rightarrow -1$ V $\rightarrow 0_{up}$ V. The voltage is keep in constant for short period of time ~4 s. For each voltage, the spin wave signal is captured by vector network analyzer with 10 times averaging. This cycle is repeated up to 600 times. The bias voltage was applied up to 5 V. This way of implementing voltage is to avoid a breakdown of the sample.

53
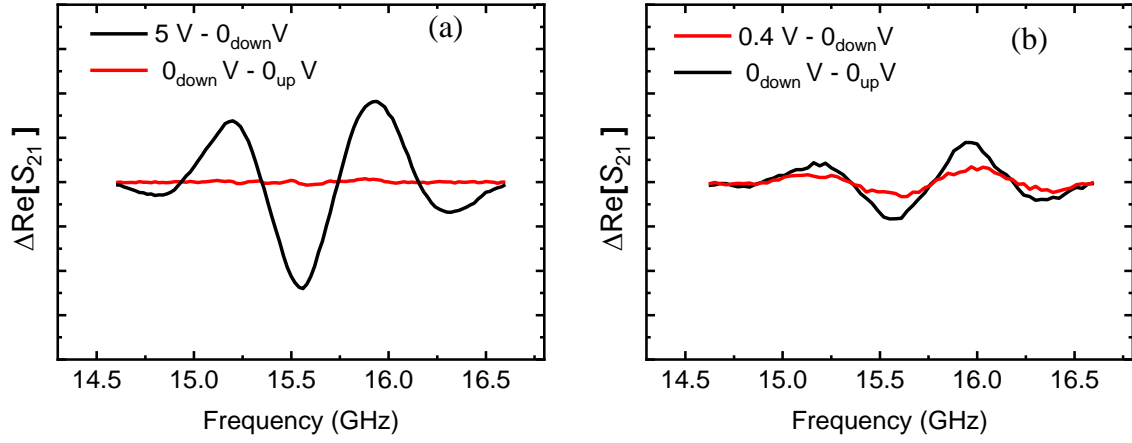
Figure 2.17: Subtracting of spin-wave propagation signal (a) sample without charge trapping, (b) sample with charge trapping

Typical spin-wave propagation. at $V_{DC} = 0$, are shown in Figure 2.16(a) and (b). One can see that the intensity of S_{21} and S_{21} are different. This is attributed to rotation direction mismatch of magnetic field produced by antenna and spin waves [92]. The subtracting signal of propagating spin wave under application of $V_{DC} = 5$ V and $V_{DC} = 0$ V are shown in Figure 2.16(c) and (d). The $Re[S_{21(12)}] = Re[S_{21(12)}(5\ V)]$ - $Re[S_{21(12)}(0\ V)]$. The subtracted signal $\Delta Re[S_{21(12)}]$ shifts to lower frequencies, indicating that the application of an external voltage affects the magnetic properties of the sample. The magnitude of shifting than can be quantified as voltage induced frequency shift (δf_R). The δf_R is obtained from $\Delta Re[S_{21(12)}] = -\delta f_{21(12)} d\ Re[S_{21(12)}(0)] / df$. Where $d Re[S_{21(12)}(0\ V)]/df$ represents the numerical differentiation of $Re[S_{21(12)}]$ signal at $V_{DC} = 0$ V. One can see from Figure 2.16 (e) the voltage-induced frequency shift are different between both directions suggesting the modulation of i-DMI. The VCMA and VCDMI can be calculated from this experimentally obtained δf_R, using Eq. (2.69) and (2.72) which given in section 2.

Now, the charge trapping phenomenon will be explained. The VCMA effect that is being motivation in this study should be a fast one (~ns). Even though from our measurement, we did not measure the time response off VCMA effect in ns region, but we can trace the hysteresis effect attributed charge trapping in insulating layer. Figure 2.17 shows the subtracting of spin-wave propagation signal. It can be seen in Figure 2.17 (b) that $0_{down} - 0_{up}$ signal (red) has almost the same order signal with applied voltage (black), suggesting there is a hysteresis existed in the sample due to present of charge trapping effects. In this study, the samples which possesses charge trapping will be excluded from VCMA and VCDMI calculation.

Chapter 3   Results and Discussion

3.1. Atomic layer insertion (Co/Pd combination)

In this section, I focused on influence of Co/Pd atomic layer insertion at Fe/MgO interface. Our interest in employing the Co/Pd layers combination was begin with several previous studies. The insertion of monolayer Co had been reported to enhance VCMA effect in single-crystalline Fe/MgO interface [93]. Moreover, a sputter-deposited Co/Pd/MgO system showed the VCMA efficiencies of −66 fJ/Vm [94] and 1600 fJ/Vm [95] at room temperature and 10 K, respectively. Previously, it was reported that the orbital magnetic moment and magnetic dipole T_z term in a FePd alloy could be modified through changes in chemical ordering [53]. Therefore, alloying of the interface, which corresponds to changing the chemical order, attached to the MgO layer may be one approach to achieve a high VCMA efficiency. Therefore, it is interesting to characterize VCMA and VCDMI under Pd layer insertion at the Fe(Co)/MgO interface in well-defined epitaxial growth sample and investigates the post-annealing treatment influence. These results had been published on physical review B journal.

3.1.1. Experimental

The sample structure is illustrated by Figure 3.1(a). The multilayers consisting of MgO(001) buffers (5 nm)/bcc-V(001) (20 nm)/bcc-Fe(001) (20 nm)/Co (t_{Co})/Pd (t_{Pd})/MgO(001) barriers (5 nm) were grown onto NaCl-type single-crystal MgO(001) substrates by the electron-beam deposition technique of molecular beam epitaxy under ultrahigh vacuum (base-pressure ~10^8 Pa). A common method to characterize VCMA involves the use of a magnetic tunnel junction-structure, in which the ferromagnetic layer thickness is typically 1–2 nm. However, to study VCMA with various thicknesses, the spin-wave spectroscopy is advantageous because it can be applicable to materials with wide ranges of interfacial PMA and DMI [69]. Notably, VCMA and VCDMI are determined only by the condition of the interface layer attached to the MgO layer and are independent of the ferromagnetic layer thickness. While a relatively thick ferromagnetic layer (20 nm) is employed for spin-wave spectroscopy to obtain high signal-to-noise ratio, the condition and materials obtained can be transferred to a more realistic structure for MRAM device. The MgO substrate was annealed at 800 °C for 10 min before the multilayer deposition. To prevent carbon diffusion from the MgO substrate surface [89], the MgO(001) buffer layer was grown
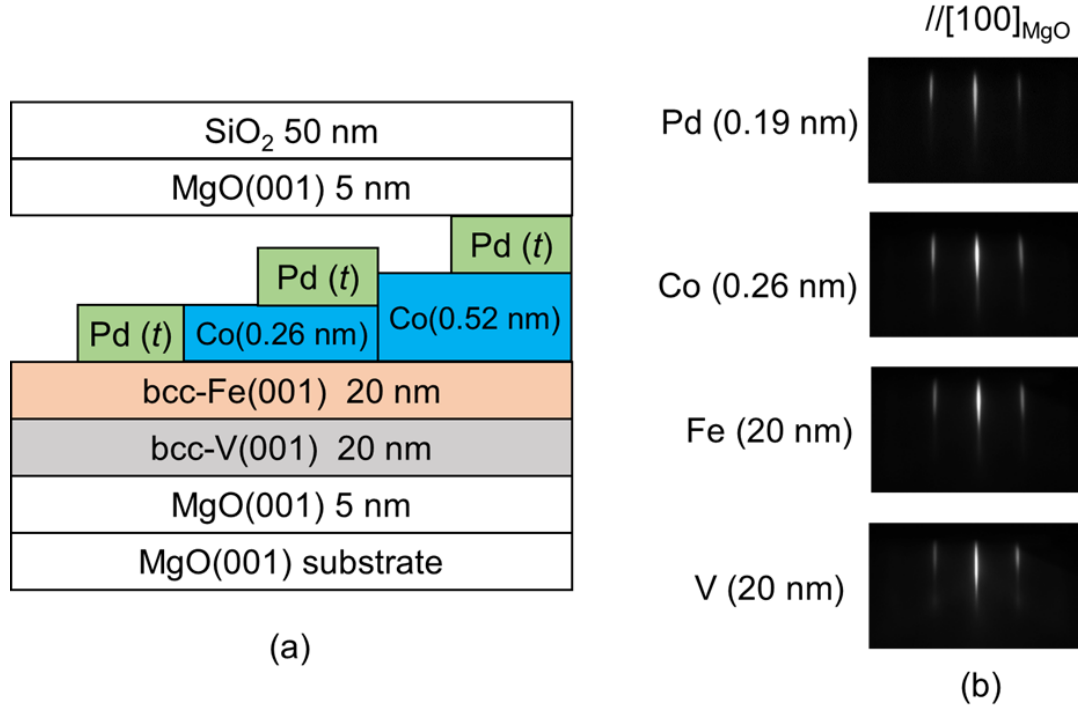
Figure 3.1: (a) Schematic illustration of the multilayer structure design. In between, Fe/MgO layer, Co and Pd thin layers were controlled to form a layer step. By this way, the Pd layer can be existed on top of Fe, Co (0.26 nm) and Co (0.52 nm). (b) Reflection high-energy electron diffraction images from the top surfaces of the V, Fe, Co, and Pd layers, where the incident beam is aligned with the [100] direction of the MgO(001) substrate.

at 150 °C. The V buffer was grown at 150 °C. After cooling, Fe layers were deposited at room temperature. To obtain a clean and flat surface, the V buffer layer and Fe layer were post-annealed at 500 °C for 30 min and 250 °C for 15 min, respectively. Afterward, 0–0.52 nm (~0–4 monolayers (MLs)) of Co and 0–0.95 nm (~0–5 MLs) of Pd were deposited without heating the substrate. All the layers with various thicknesses were prepared on the same wafer by using a position-controlled linear shutter during deposition. With these thickness variations, we can investigate the interfaces of Fe/MgO, Co/MgO, Fe/Pd/MgO, and Co/Pd/MgO. After the MgO barrier deposition, the multilayer was removed from vacuum. A 50-nm-thick SiO_2 layer was deposited by sputtering as an additional dielectric layer. Figure 3.1(b) shows images obtained by reflection high-energy electron diffraction of the V, Fe, Co, and Pd layers. Sharp streak patterns are observed in all layers, indicating the formation of epitaxial and flat interfaces at each layer. The 0.26-nm Co (~2 ML) and 0.19-nm Pd (~1 ML) layers are confirmed to have grown coherently onto the bcc-Fe(001) surface.
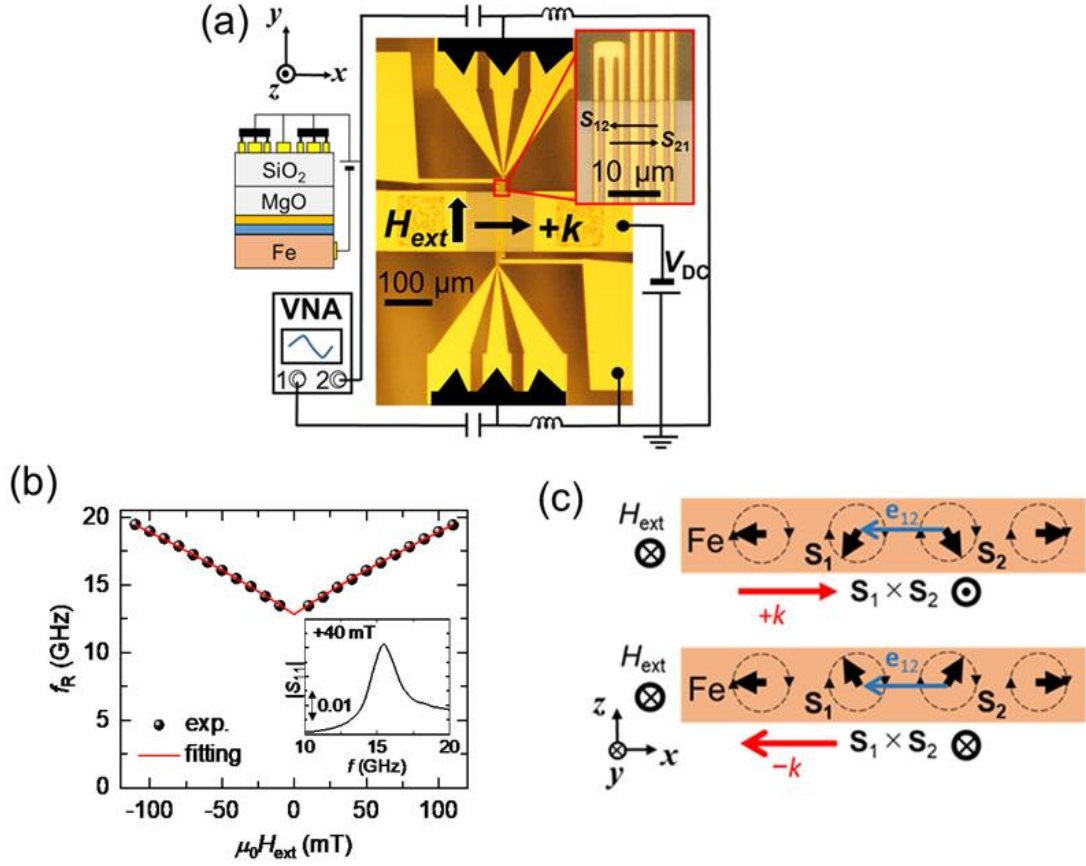
Figure 3.2: (a) Optical microscope image of spin-wave device with measurement configuration schematic. An in-plane magnetic field (H_{ext} in the *y*-direction) is applied to excite magneto-static surface spin-waves (MSSWs). The *k*-vector of the MSSW is parallel to the *x*-direction. A vector network analyzer is connected to two microscale antennas to excite and detect the spin-waves. An electric field (*z*-direction) is applied to the ferromagnetic layer through the MgO/SiO$_2$ dielectrics when a bias voltage (V_{DC}) is applied to the two antennas and gate electrode. (b) The magnetic field dependence of the spin-wave resonant frequency (f_R) of Fe/Co (0.52 nm)/Pd (0.19 nm), determined from the peak position of the S_{11} signal. The red curve shows fitting (Eq. (3.1)). (c) Directional dependence of MSSW propagation. MSSW with +*k* and –*k* corresponds to signals from vector network analyzer of S_{21} and S_{12}, respectively. Black arrows indicate the spin direction; circles represent the precessional motion of the spin.

The characterizations of VCMA and VCDMIs in the multilayers depicted in Figure 3.1 were conducted by spin-wave spectroscopy. Figure 3.2(a) shows the top view of the spin-wave device with the measurement geometry. By using electron-beam lithography and Ar ion milling, the multilayer film was patterned into a rectangular shape (100 × 400 μm) with the

long axis parallel to the Fe[100] direction. Two antennas (short-circuit coplanar waveguide) composed of Cr (5 nm)/Au (200 nm) films were fabricated parallel to the Fe[100] direction through a lift-off process. An in-plane magnetic field was applied in the y-direction to excite the magnetostatic surface spin-wave (MSSW). The two individual antennas separated by 10 μm were designed to excite and detect the spin-waves in the $\pm x$-direction with the wave number (k) of 1.2 μm^{-1}. The inset of Figure 3.2(a) depicted the antenna that consists of a signal line (2 μm) and two ground lines (1 μm) with gaps of 1 μm, and an intermediate gate electrode between the antennas. The voltage is applied to the Fe ferromagnetic layer, which is schematically depicted in left-hand-side inset. The MSSW in the device was analyzed by measuring the S parameters using a vector network analyzer with an applied radio frequency power of −15 dBm (32 μW) and a bandwidth of 1 kHz. Between the two antennas, an intermediary gate electrode was placed; all are connected to the same ground via bias-tee. To investigate the electric field-induced changes of the interfacial magnetic anisotropy and Dzyaloshinskii-Moriya interactions, that is, the VCMA and VCDMI, a bias voltage (V_{DC}) was applied during the spin-wave measurements. It was previously reported that changes in the chemical order of ferromagnetic materials around interfaces with MgO may influence the VCMA [52]. To observe this, we also performed the spin-wave measurements with post-annealed devices. The post-annealing of the spin-wave device was conducted for 30 min at 200–300 °C under high vacuum ($<4 \times 10^{-4}$ Pa).

Figure 3.2(b) shows the typical spin-wave resonant frequency (f_R) under different external magnetic fields ($\mu_0 H_{ext}$) for the Fe/Co (0.52 nm)/Pd (0.19 nm)/MgO sample. The frequency is determined from the peak position of the $|S_{11}|$ spectrum. For instance, a spectrum under $\mu_0 H_{ext} = 40$ mT is depicted in the Figure 3.2(b) inset. In this case, no bias voltage was applied ($V_{DC} = 0$). To analyze the fourfold crystalline anisotropy ($\mu_0 H_{cry}$) and the interfacial perpendicular anisotropy field ($\mu_0 H_{int}$), we fitted the resonant frequency (f_R) by using the following equation [69],[25]:

$$f_R = -\frac{\gamma_0 \mu_0}{2\pi} \sqrt{ \begin{array}{c} \left(|H_{ext}| + H_{cry} \right) \left(|H_{ext}| + M_S + H_{cry} - H_{int} \right) \\ + \dfrac{M_S}{4} \left(M_S - H_{int} \right) \left(1 - \exp\left(-2|k|t_{Fe} \right) \right) \end{array} } \qquad (3.1)$$

where γ_0 is the gyromagnetic ratio of Fe ($-\gamma_0/2\pi = 2.94 \times 10^{10}$ 1/(T·s)), μ_0 is the permeability of vacuum ($4\pi \times 10^{-7}$ H m^{-1}), M_S is the saturation magnetization of the bulk Fe ($\mu_0 M_S = 2.16$ T), k is the wavenumber (1.2 μm^{-1}) determined by the waveguide design, and t_{Fe} is the thickness of the Fe layer (20 nm). While the interfacial property $\mu_0 H_{int}$ might be sensitive to Co and Pd
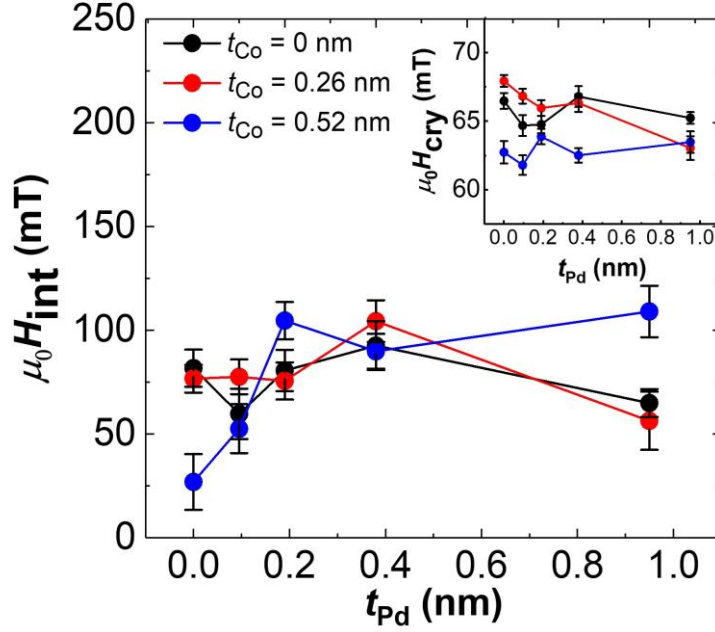
Figure 3.3: Interfacial perpendicular magnetic anisotropy field ($\mu_0 H_{int}$) as a function of Pd thickness (t_{Pd}) for various thicknesses of Co (t_{Co}). Inset graph shows the crystalline anisotropy field ($\mu_0 H_{cry}$).

insertion, the bulk physical properties, i.e. γ_0, M_S, and t_{Fe}, are assumed to be constant. This is because the thicknesses of the inserted Co and Pd layers (< 1 nm) are much smaller than that of the Fe layer (20 nm). $\mu_0 H_{int}$ is correlated to the perpendicular magnetic anisotropy energy, K_{int}, and is expressed as $K_{int} = \mu_0 M_S t_{Fe} H_{int}/2$. The S_{11} spectrum includes the excitation of MSSWs in both the $+k$ and $-k$ directions; therefore, the spectrum may show splitting from the i-DMI contribution [66], [81]. However, in Figure 3.2(b), it is difficult to confirm splitting in the S_{11} spectrum. The original i-DMI is small because of the relatively thick ferromagnetic layer (~20 nm); therefore, the possible peak split caused by the i-DMI energy would be much smaller than the linewidth of the spectra. For this reason, the i-DMI term was neglected in Eq. (3.1).

To characterize the VCMA and VCDMIs, spin-wave spectroscopy with a modulation technique [69] was implemented. We averaged 600 individual spectra of the S_{21} and S_{12} propagation signals under an applied bias voltage. Figure 3.2(c) illustrates the directional dependence of MSSW propagation. It shows that MSSWs with different k-directions possess different vector spin chiralities. This non-reciprocal property of the MSSW reflects the i-DMI in the system. The i-DMI energy modulation can be calculated from the difference between the S_{21} and S_{12} signals, which correspond to the $+k$ and $-k$ propagation directions, respectively.

3.1.2. Evaluation of magnetic anisotropy field

The interfacial perpendicular magnetic anisotropy field ($\mu_0 H_{int}$) in the Fe/Co/Pd/MgO multilayers for various configurations of materials and thicknesses are summarized in Figure 3.3. In Figure 3.3, the multilayer is not post-annealed. In the inset graph, a slight change in the $\mu_0 H_{cry}$ value from the Co and Pd insertion is observed; the value ranges within 7% of the value for the Fe/MgO sample ($\mu_0 H_{cry} = 66.4 \pm 0.6$ mT). However, $\mu_0 H_{int}$ shows significant changes for different interfaces. For the Fe/Co/MgO system ($t_{Pd} = 0$ nm), increasing t_{Co} decreases $\mu_0 H_{int}$, implying that the perpendicular magnetic anisotropy (i-PMA) in the system is decreased by the presence of Co. Such behavior is consistent with a previous report [96], in which the i-PMA at a Fe/MgO interface was greater than that at Co/MgO.

The Pd thickness dependence is discussed as follows. A few monolayers of interfacial Pd atoms with ferromagnetic metals should be spin-polarized because of ferromagnetic proximity-induced effects [97], [98]. In this regard, in the relatively thin region ($t_{Pd} < 0.4$ nm), Pd atoms at the interface of MgO should be ferromagnetic and the i-PMA energy should come from the Pd/MgO interface. In contrast, in the relatively thick region (~1 nm), Pd atoms at the interface of MgO should be paramagnetic and the interfacial i-PMA energy should not come from the Pd/MgO interface but from the Fe/Pd interface. For Fe/Pd/MgO ($t_{Co} = 0$ nm), $\mu_0 H_{int}$ is almost constant as t_{Pd} increases, suggesting that the i-PMA at the Fe/MgO ($t_{Pd} = 0$ nm), Pd/MgO ($t_{Pd} \sim 0.2$ nm), and Fe/Pd ($t_{Pd} \sim 1$ nm) interfaces are almost identical to each other. For thick Co ($t_{Co} = 0.52$ nm), the interface can be regarded as Co/Pd/MgO. $\mu_0 H_{int}$ is increased from 25 mT (Co/MgO, $t_{Pd} = 0$ nm) to ~100 mT ($t_{Pd} > 0.2$ nm), suggesting that the i-PMA values of the Pd/MgO ($t_{Pd} = 0$ nm) and Co/Pd ($t_{Pd} \sim 1$ nm) interfaces are comparable, but are larger than that of the Co/MgO interface ($t_{Pd} = 0$ nm). For the 0.26-nm Co, the interface may be mixed Co–Fe/Pd/MgO with intermediate i-PMA values. The error bars of $\mu_0 H_{int}$ and $\mu_0 H_{cry}$, originally determined from fitting using Eq. (3.1), represent the standard deviation obtained by the root mean square method.

3.1.3. Evaluation of VCMA and VCDMI

The voltage-induced effect is now discussed. As mentioned earlier, the analyses of the VCMA and VCDMIs were conducted through the spin-wave propagation signals (S_{21} and S_{12}). Figure 3.4(a) and (b) show typical spectra of the real parts of S_{21} and S_{12}, respectively, for the
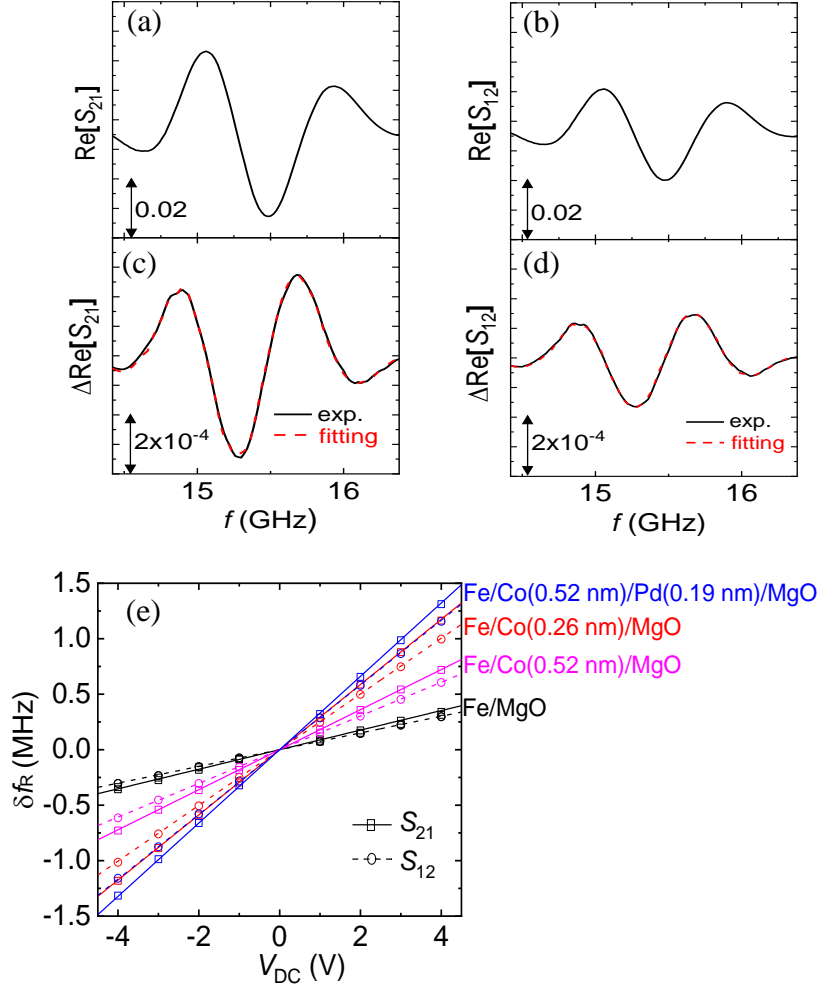
Figure 3.4: (a), (b) Typical spin-wave propagation signals of Fe/Co (0.52 nm)/Pd (0.19 nm)/MgO in +k (S_{21}) and -k (S_{12}) directions under zero bias voltage ($V_{DC} = 0$ V) measured under $H_{ext} = 40$ mT. (c), (d) Typical voltage-induced change in the spin-wave signals, where the S_{21} and S_{12} taken at 0 V are subtracted from those taken at -5 V. The red curve show fitting (Eq. (3.2)). (e) Typical resonant frequency shifts (δf_R) as functions of V_{DC}.

Fe/Co (0.52 nm)/Pd (0.19 nm)/MgO sample taken at $V_{DC} = 0$ V and $\mu_0 H_{ext} = 40$ mT. Afterward, a bias voltage reaching -5 V is applied. Solid lines in Figure 3.4(c) and (d) show the subtracted signal $\Delta \mathrm{Re}[S_{21(12)}] = \mathrm{Re}[S_{21(12)}(\text{-5 V})] - \mathrm{Re}[S_{21(12)}(0 \text{ V})]$, indicating that the signal is modulated by the bias voltage. We define this modulation as the voltage-induced frequency shift (δf_R) and estimate its value by fitting to the function expressed as:

$$\Delta \mathrm{Re}[S_{21(12)}] = -\delta f_{21(12)} \frac{d\,\mathrm{Re}[S_{21(12)}]}{df} \tag{3.2}$$

where $d\mathrm{Re}[S_{21(12)}]/df$ is the numerical differentiation of the experimentally obtained $S_{21(12)}$ spectrum. The intensity difference between S_{21} and S_{12} observed in Figs. 3.4(a) and (b) is

attributed to the mismatch of spatial rotation of the radio frequency field and the MSSW [92]. Figure 3.4(e) shows the voltage-induced frequency shift (δf_R) as a function of the bias voltage (V_{DC}). The solid and dashed lines represent δf_{21} and δf_{12}, respectively. These have similar tendencies, showing increases as functions of V_{DC}, which arises from the VCMA effect. Moreover, a small but significant difference appears between the slopes of δf_{21} and δf_{12}, which originates from the VCDMI in the system. Figure 3.4(e) shows the frequency shifts for several insertion thicknesses. A linear relation is observed between δf and V_{DC}. We obtain the highest slope of δf_{21} = 0.329 ± 0.001 MHz/V for Fe/Co (0.52 nm)/Pd (0.19 nm)/MgO; it is approximately 3.5 times larger than the slope obtained with Fe/MgO. This is discussed later in detail.

The VCMA magnitude is defined as the change of the interfacial perpendicular magnetic anisotropy upon voltage application. For a propagating spin-wave, the resonant frequency (f_R) can be expressed as the contributions of the anisotropy and i-DMI terms [20], [25]:

$$f_{\mathrm{R}} = -\frac{\gamma_0 \mu_0}{2\pi} \sqrt{\begin{aligned} & \left(|H_{\mathrm{ext}}| + H_{\mathrm{cry}}\right)\left(|H_{\mathrm{ext}}| + M_{\mathrm{S}} + H_{\mathrm{cry}} - H_{\mathrm{int}}(V_{\mathrm{DC}})\right) \\ & + \frac{M_{\mathrm{S}}}{4}\left(M_{\mathrm{S}} - H_{\mathrm{int}}(V_{\mathrm{DC}})\right)\left(1 - e\left(-2|k|t_{\mathrm{Fe}}\right)\right) \end{aligned}} \mp \frac{\gamma_0}{\pi}\frac{D(V_{\mathrm{DC}})k}{M_{\mathrm{S}}} \quad (3.3)$$

where D is the i-DMI contribution and $\mp$ denotes the magnetic field direction. When a bias voltage modulates $\mu_0 H_{\mathrm{int}}$, that is, under the VCMA effect, f_R should be shifted. From the shift of f_R (δf), we can calculate the VCMA efficiency from Eq. (3.3) expressed as follows:

$$\xi_{\mathrm{VCMA}} = -\frac{M_{\mathrm{S}}t_{\mathrm{Fe}}}{\mu_0 E_{\mathrm{MgO}}}\frac{\left(\frac{2\pi}{\gamma_0}\right)^2 f_{\mathrm{R}}\left(\dfrac{\delta f_{21} + \delta f_{12}}{2}\right)}{\left(H_{\mathrm{ext}} + H_{\mathrm{cry}} + \dfrac{M_{\mathrm{S}}}{4}\left(1 - e^{-2kt_{\mathrm{Fe}}}\right)\right)} \quad (3.4)$$

where E_{MgO} = 0.008 nm^{-1} × V_{DC} is the electric field in the MgO layer. Here, we modeled the sample as two capacitors in series where the dielectric constants of SiO$_2$ and MgO are 3.9 and 9.6, respectively. The polarity of the voltage is defined as positive (or negative) when electrons (or holes) are induced at the Fe/MgO interface. Moreover, we can calculate the voltage-controlled i-DMI change (VCDMI) by considering the directional dependence of δf:

$$\xi_{\mathrm{iDMI}} = -\frac{\pi}{\gamma_0}\frac{M_{\mathrm{S}}}{E_{\mathrm{MgO}}k}\left(\frac{\delta f_{21} - \delta f_{12}}{2}\right) \quad (3.5)$$

Eq. (3.5) can be derived from Eq. (3.3). For both VCMA and VCDMI, the coefficients are determined by the interface and are independent of the bulk properties. The fitting coefficient for the VCMA ($\delta f_{21} + \delta f_{12}$) and VCDMI ($\delta f_{21} - \delta f_{12}$) are not interdependent. In this study, the error bar for VCMA and VCDMI are determined from the standard error of the δf_R vs. V_{DC} slope (see Figure 3.4 (e)), which can be expressed as:

$$\varepsilon_{\delta f_R / V_{DC}} = \frac{\sqrt{\sum_{i=1}^{n} \left(\delta f_{R_i} - \delta \hat{f}_{R_i} \right)^2 / (n-1)}}{\sqrt{\sum_{i=1}^{n} (V_{DC_i} - \overline{V}_{DC})^2}} \tag{3.6}$$

where, n is the number of data points and $\delta f_R - \delta \hat{f}_R$ denotes the residue of δf_R.

The results of voltage-induced effects, that is, the changes in interfacial magnetic anisotropy energy and Dzyaloshinskii-Moriya interaction energy for as-grown samples, are shown in Figure 3.5 as functions of t_{Pd}. The interfacial Pd atoms with ferromagnetic metals are expected to be spin-polarized because of ferromagnetic proximity-induced effects [97], [98]. First, we discuss the VCMA results shown in Figure 3.5(a). The VCMA tends to decrease as t_{Pd} is increased in Fe/MgO. If the VCMA coefficients at the Fe/MgO and Pd/MgO interfaces with proximity-induced spin-polarization from Fe are opposite to each other, such VCMA decrease with increasing t_{Pd} can be explained. Similarly, it has previously been reported that $L1_0$-FePd/MgO shows a positive VCMA effect [99], which is the same VCMA polarity as that of Fe/Pd/MgO obtained in this study. Compared to the Fe/MgO interface, the VCMA at the Fe/Co (0.52 nm)/MgO interface is increased with increasing t_{Pd}. The highest VCMA efficiency of −180 fJ/Vm is obtained at t_{Pd} = 0.19 nm. This shows that the Pd/MgO interface with proximity-induced spin-polarization from Co has a larger VCMA than the interface of Co/MgO; both VCMAs have the same polarity. Therefore, Pd insertion contributes constructively to the VCMA effect. Interestingly, VCMA effect at the Pd/MgO interface with proximity-induced spin polarization from Fe and that from Co have opposite signs. The tendency for the VCMA effect in the Fe/Co (0.26 nm)/Pd/MgO interface is between that in Fe/Pd/MgO and Fe/Co (0.52 nm)/Pd/MgO.

It was reported that voltage-induced changes in the orbital magnetic moment in the Co/MgO system [93] were larger than those in the Fe/MgO system [33],[34]. Because the orbital magnetic moment mechanism explains the VCMA effect in $3d$ transition metals [93], [35], the observed larger VCMA in the Co/MgO system than that in the Fe/MgO system in this

63
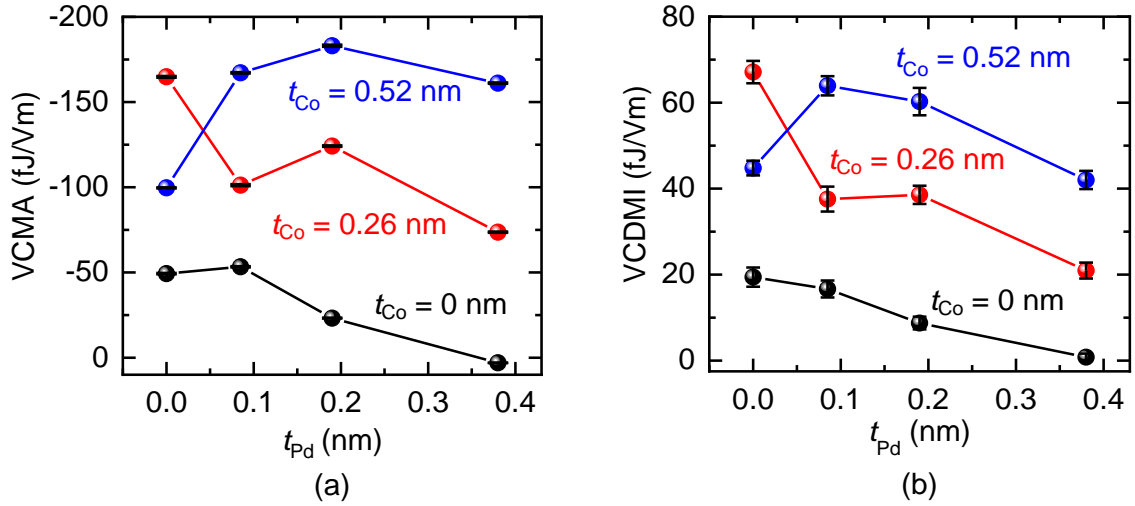
Figure 3.5: The Pd thickness (t_{Pd}) dependence of (a) voltage-controlled magnetic anisotropy (VCMA, Eq. (3.4)) and (b) voltage-controlled interfacial Dzyaloshinskii-Moriya interaction (VCDMI, Eq. (3.5)) change for the as-grown sample. Black plots represent the Fe/MgO interefaces.

study is consistent with the reported larger orbital magnetic moment change. Notably, the voltage-induced change in orbital magnetic moment is estimated to be only 0.1% of the total magnetic moment [93]. Thus, its influences on magnetization change are negligibly small. With Pd insertion, the situation might be different. For the Fe(Co)/Pd/MgO system, the interfacial Pd metal with induced spin-polarization should explain the VCMA. Because of the strong electrostatic screening effect, the electric field is only applied to atoms interfacing with MgO in ferromagnetic materials [52], [93]. The larger VCMA in the Pd/MgO system is attributed to the large spin-orbit interaction coefficient in Pd and/or the existence of the electric quadrupole mechanism, in addition to the orbital magnetic moment mechanism [52]. The source of the difference in the VCMA polarities between the Co/Pd/MgO and Fe/Pd/MgO systems remains an open question. For Fe/Co (0.26 nm)/MgO, the VCMA effect (−165 fJ/Vm) is larger than that of Fe/Co (0.26 nm)/MgO. This may be because of the larger magnetic moment of Co in the Fe/Co (0.26-nm)/MgO system than that in the Fe/Co (0.52-nm)/MgO system [93]. Because the VCMA efficiency is proportional to the orbital magnetic moment change in such a system, a larger magnetic moment can induce a larger VCMA efficiency. For Pd insertion in the Fe/Co (0.26-nm)/MgO sample, the interface with MgO may be mixed FeCo, with VCMA contributions from both Co/Pd/MgO and Fe/Pd/MgO.

Second, we discuss the VCDMI for the as-grown multilayer Fe/Co/Pd/MgO system. The i-DMI energy should exist on the top and bottom layers attached to the ferromagnetic metals. In our study, the VCDMI should be attributed only to the top side, which is attached to the MgO. This is because the bias electric field is applied only to interfacial atoms around MgO [52], [93]. Figure 3.5(b) shows the VCDMI for the as-deposited samples. It shows that the Co/MgO interface has a larger VCDMI than that of Fe/MgO. Moreover, thin Pd insertion in the Co (0.52 nm)/MgO system enhances the VCDMI.

As discussed for the VCMA effect, it was reported that voltage-induced changes in orbital magnetic moment in Co/MgO [93] were larger than those in Fe/MgO [100], [101]. This strongly suggests that the voltage-induced orbital angular momentum is larger at the Co/MgO interface. Because i-DMI is strongly related to the orbital angular momentum in ferromagnetic materials [55], [56], the VCDMI in Co/MgO is larger than that in Fe/MgO. In Figure 3.5(b), the VCDMI is enhanced by Pd insertion, which is probably mediated by the large spin-orbit interaction coefficient of Pd. In this work, the maximum VCDMI of 65 fJ/Vm is obtained in the Fe/Co (0.26 nm)/MgO system. Because the i-DMI is inversely proportional to the ferromagnetic layer thickness [67], [103], the VCDMI of 65 fJ/Vm corresponds to the i-DMI energy density change of ~1.3 mJ/m^2 when the 1-nm-thick ferromagnetic layer and 1 V/nm electric field are employed in MgO. If we use MTJ devices, such conditions can be easily prepared. Therefore, it should be noted that the VCDMI is large enough to stabilize and destabilize chiral magnetic structures such as skyrmion states [61].

3.1.4. Influence of post-annealing

Finally, the post-annealing influence on VCMA and VCDMI is discussed. Figure 3.6(a)-(c) show the VCMA values as functions of the annealing temperature for three different Co thicknesses. For the Fe/MgO and Co (0.52 nm)/MgO interfaces, the impact of post-annealing is not significant. This suggests that post-annealing does not significantly change the materials interfacing with MgO. However, the VCMA in Fe/Co (0.26 nm)/MgO shows a monotonic decrease with post-annealing. This is probably because post-annealing enhances the alloying of Fe and Co at the interface with MgO.

When Pd is introduced at the Fe/MgO and Co/MgO interfaces, the situations differ. Post-annealing slightly increases the VCMA in Fe/Pd/MgO (Figure 3.6(a)) and significantly decreases the VCMA in Co/Pd/MgO (see Figure 3.6(b) and (c)). For Fe/Pd/MgO, because post-
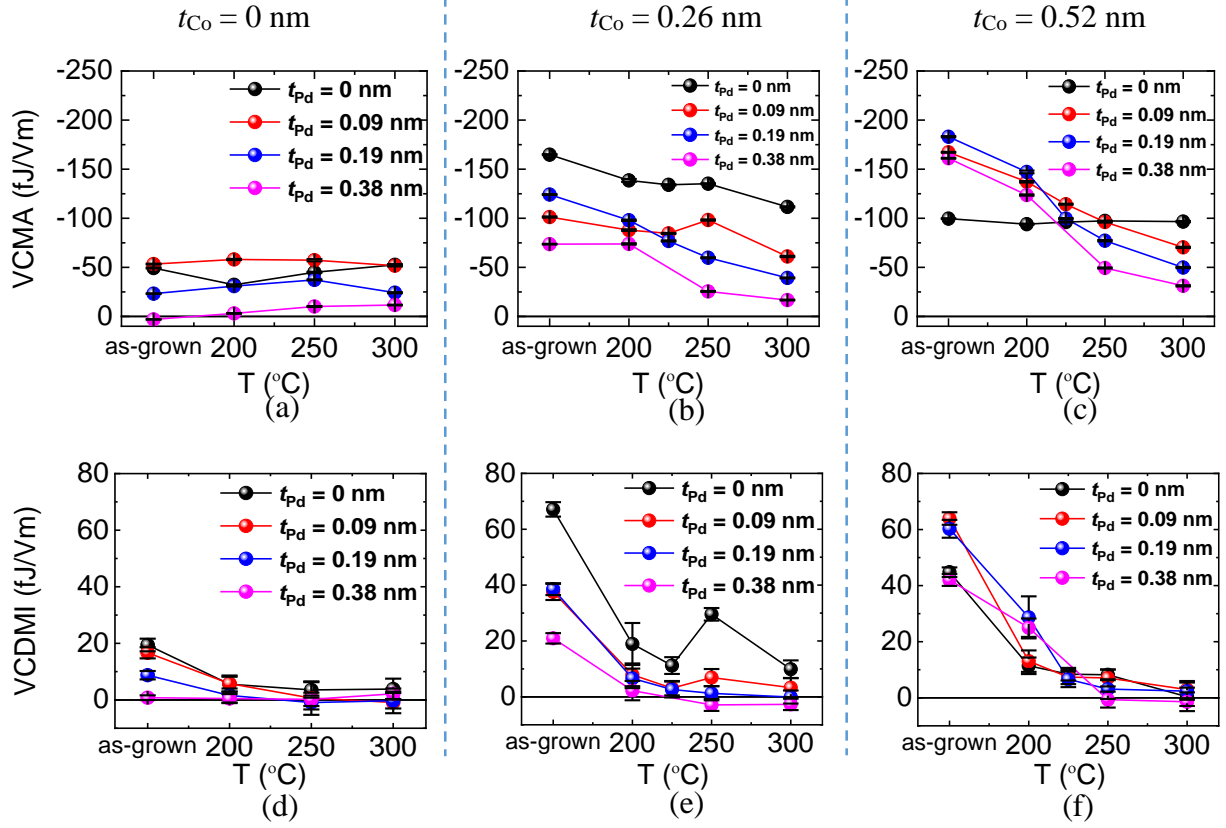
Figure 3.6: VCMA (Eq. (3.4)) and VCDMIs (Eq. (3.5)) as functions of post-annealed temperatures (*T*) for sample 1: Fe/Co/Pd/MgO. (a),(d), (b),(e), and (c),(f) represent Co thicknesses (t_{Co}) of 0 nm, 0.26 nm, and 0.52 nm, respectively.

annealing enhances the Pd diffusion into Fe, we may expect the influence of Pd/MgO on VCMA to decrease. For Fe/Co/Pd/MgO, the decrease of VCMA can be attributed to the change in the chemical order in the Co–Pd alloy located at the interface with MgO. Recently, it was reported that a FeIr alloy/MgO structure showed the large VCMA of −320 fJ/Vm (Ref.[104]), suggesting that a change in the chemical order around the interface with MgO was effective in enhancing the VCMA. This is because changes in the chemical order affect both contributions from the VCMA mechanisms, that is, orbital magnetic moment and electric quadrupole mechanisms [52], [53]. Apart from this, our results show that VCMA in the FePd alloy/MgO system is slightly higher than that in the Fe/Pd/MgO system, whereas that in the CoPd alloy/MgO system is much smaller than that in the Co/Pd/MgO system. Therefore, the chemical order of 1, that is, the layered multilayer realized in the as-deposited sample, is the best condition for the VCMA effect in the Co–Pd/MgO systems.

Now, the influenced of post-annealing to VCDMI for Co/Pd inserted sample will be discussed. Figure 3.6 (d-f) show the VCDMI for $t_{Co} = 0$ nm, 0.26 nm, and 0.52 nm as functions of the post-annealed temperature. The VCDMI decreases as the annealing temperature increases for all systems. To discuss the VCDMI, the following two models of Rashba [105] and spin-current [106] can be employed. As discussed previously [107], [108], the Rashba model is more applicable for ferromagnetic metals with insulating dielectric layers, such as MgO. For both models, i-DMI cannot be explained by either on-site (intra-atomic) magnetic properties, as the VCMA effect can, or inter-atomic ones. A post-annealing induces intermixing around the interface with MgO. Therefore, post-annealing changes the on-site magnetic properties because of the replacement of the materials forming interfaces with MgO. For this reason, the tendencies of VCMA and VCDMIs should be similar, which is experimentally observed for the Pd-inserted samples. However, the tendencies for the changes in VCMA and i-DMI are very different for the case of Fe/MgO and Co/MgO. The VCDMI is sensitive to post-annealing, while the VCMA effect is not. This strongly suggests that the VCDMI is sensitive to slight changes of the in-plane lattice constant and/or dislocations around the interface with MgO, which is not the case for the VCMA effect, governed only by on-site magnetic properties. Similarly, it was reported that post-annealing decreased i-DMI in Pt/Co/AlO$_x$ and Pt/CoFeB/AlO$_x$ systems [109].

3.1.5. Summary

The influence of Co and Pd monolayer insertions at Fe/MgO interfaces on voltage-controlled magnetic anisotropy (VCMA) and voltage-controlled Dzyaloshinskii-Moriya interaction (VCDMI) was investigated. As compared with Fe/MgO, a decreasing of VCMA efficiency was obtained in Fe/Pd/MgO, while in Fe/Co/MgO, a larger VCMA efficiency was obtained. Moreover, Pd insertion at the Co/MgO interface enhanced the VCMA efficiency. We obtained the largest VCMA efficiency of −180 fJ/Vm in the Fe/Co/Pd system. Moreover, the high VCDMI of 65 fJ/Vm was obtained in Fe/Co/MgO. For the Fe/Co/Pd system, the post-annealing process monotonically reduced VCMA and VCDMI with increasing temperature. Therefore, we concluded that layered multilayers, rather than alloys, provide the best conditions for manipulating VCMA and VCDMI in Fe/Co/Pd/MgO systems.

3.2. Artificial alloy formation (Ir location control in Fe)

Contrary to our observation that post-annealing decrease the VCMA and VCDMI in Fe/Co/Pd/MgO, the Ir diffusion into Fe-layer enhanced the VCMA was demonstrated [51]. Nozaki et al, reported the formation of FeIr-alloy/MgO lead to high VCMA efficiency of -320 fJ/Vm. Moreover, from the same report, the first principles calculation revealed that the Ir located in the sub-layer responsible to increase total VCMA in FeIr-alloy/MgO system. Therefore, it is interesting to experimentally investigate the Ir location contribution to VCMA and VCDMI by intentionally control the location of Ir atoms using epitaxial growth. In this section, we fabricated an artificial alloy by controlling the location of Ir atoms in respect to MgO layer. We referred this sample as sample 1. Moreover, we also fabricated another Fe/Ir/MgO sample and investigated the post-annealing influence to VCMA and VCDMI by using spin-wave spectroscopy. We referred this sample as sample 2.

3.2.1. Experimental

The schematic of multilayer structure of artificial alloy sample is depicted in Figure 3.7(a). The multilayers consisting of MgO(001) buffers (5 nm)/bcc-V(001) (20 nm)/bcc-
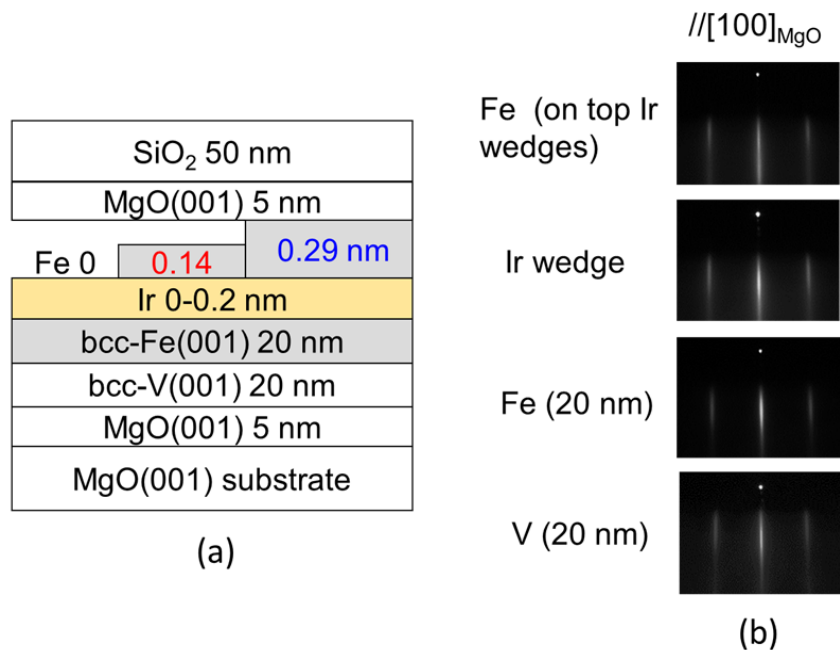
Figure 3.7: (a) Schematic of sample 1; artificial alloy formation of Fe/Ir/Fe/MgO. On top of Ir wedge (0-0.2 nm), we deposited Fe (0.14 nm ~ 1 ML) and Fe (0.29 nm). By this way, the Ir location respect to MgO layer was controlled. (b) the reflection high-energy electron diffraction (RHEED) image from the top surfaces of the V, Fe, Ir, and Fe (top), where the incident beam is aligned with the [100] direction of the MgO(001) substrate.
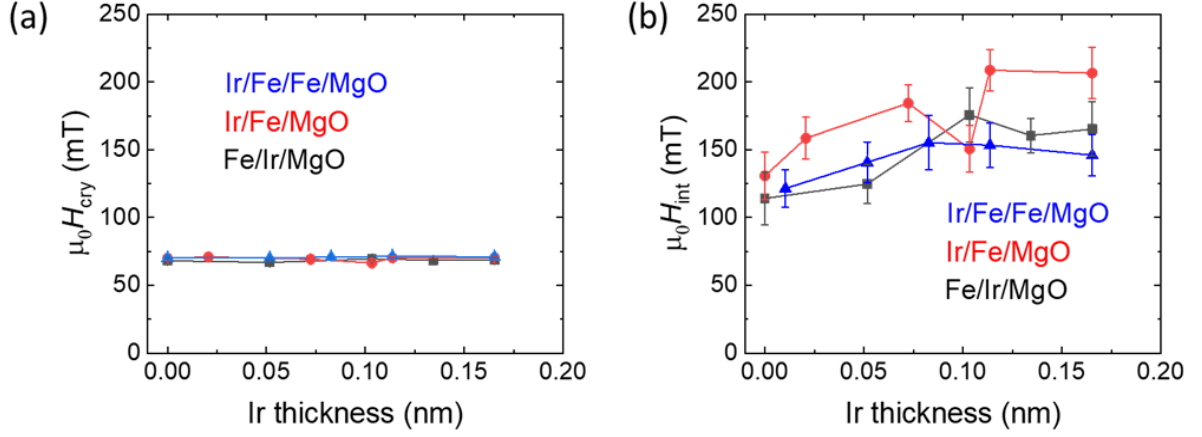
Figure 3.8: (a) The fourfold crystalline anisotropy field ($\mu_0 H_{cry}$) and (b) Interfacial perpendicular magnetic anisotropy field ($\mu_0 H_{int}$) as a function of Ir thickness for three different Ir atoms locations in respect to MgO.

Fe(001) (20 nm)/Ir wedges (0-0.2 nm)/Fe (0, 0.14 nm and 0.29 nm)/MgO(001) barriers (5 nm) were grown onto NaCl-type single-crystal MgO(001) substrates by using the electron-beam deposition technique of molecular beam epitaxy under ultrahigh vacuum (base-pressure ~10^8 Pa). Through this configuration, the Ir location in respect to MgO layer was controlled. Figure 3.7(b) shows the reflection high-energy electron diffraction pattern for the V, Fe, Ir, and Fe top layers for the incident beam parallel to MgO [100] direction. Streak patterns indicate the formation of epitaxial and flat interfaces at each layer. The Ir wedge and the top Fe-layer are confirmed to have grown coherently onto the bcc-Fe(001) surface. The sample then was taken out from vacuum and 50-nm SiO$_2$ is deposited as additional insulating layer. Then, two micro-sized antennas were fabricated through microfabrication process. The evaluation of magnetic anisotropy field, VCMA and VCDMI was carried out through spin-wave spectroscopy, same as the previous section 3.1.1

3.2.2. Evaluation of magnetic anisotropy field

The fourfold-crystalline magnetic anisotropy field ($\mu_0 H_{cry}$) and interfacial perpendicular magnetic anisotropy field ($\mu_0 H_{int}$) are summarized in Figure 3.8(a) and (b), respectively. It can be seen than H_{cry} is almost constant while the H_{int} is changing with Ir thickness. Moreover, the H_{int} in Ir/Fe/MgO was higher than the Fe/Ir/MgO suggests the higher i-PMA when Ir was located in the second layer. This observation is qualitatively consistent with the previous report of the PMA energy in FeIr-alloy/MgO supercell structure, studied by first principles calculation [51]. Higher PMA energy was obtained when the FeIr alloy located in second layer compared to the first layer from MgO.

69

3.2.3. Evaluation of VCMA and VCDMI
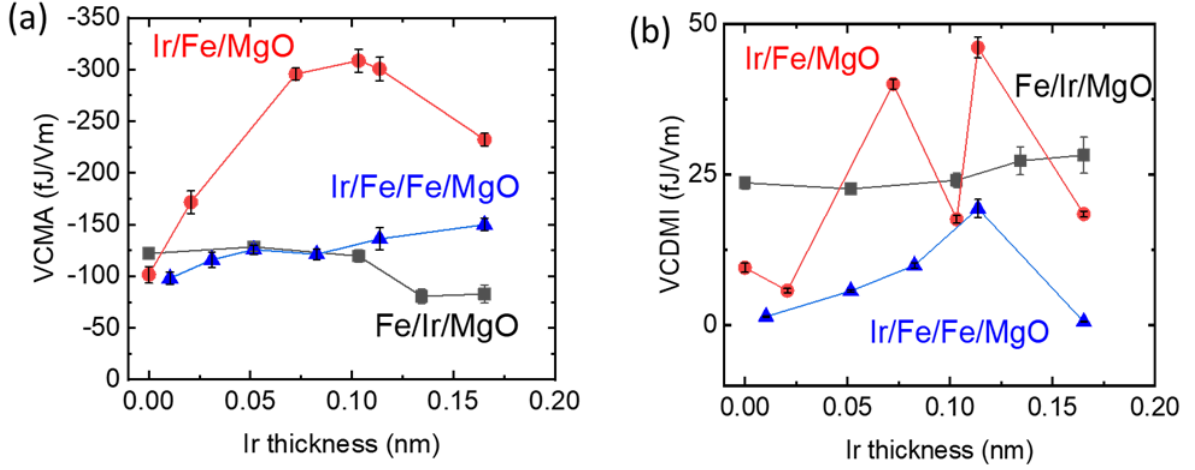
Figure 3.9: Ir thickness dependence of (a) VCMA and (b) VCDMI for three different location of inserting Ir atoms.

Next, VCMA and VCDMI for will be discussed. Figure 3.9 (a) shows the Ir thickness dependence of VCMA for three inserted-Ir locations. It can be seen, the different location of Ir, strongly affected the VCMA value. When the Ir was inserted in between the Fe/MgO interface (black line), the VCMA is almost constant as the Ir thickness increased, before its decrease after Ir thickness more than 0.1 nm. It suggested the Ir layer with proximity induced spin-polarization of Fe has low VCMA. Moreover, VCMA value was almost constant in Ir/Fe/Fe/MgO (blue line). The increasing of Ir thickness strongly enhanced the VCMA in Ir/Fe/MgO (red line). The VCMA peaked around Ir thickness of 0.1 nm (0.5 ML coverage). This result suggests the Ir atoms placed in the second layer respect to MgO has large contribution to total VCMA. This observation can be understood local densities of states (LDOS) from previous report in MgO/(FeIr)$_5$/MgO system [110]. Miwa et al., compare the LDOS of Ir first layer and second layer contribution to the PMA energy. When Ir is located in the first layer, the $d_{z^2-r^2}$ orbital is presence around the fermi level (E_F) due to hybridization of with p_z orbital of oxygen from MgO. Since the $d_{z^2-r^2}$ orbital prefer in-plane magnetization, its lead to low PMA energy for Ir in the first layer. On the other hand, $d_{z^2-r^2}$ orbital is absence around the fermi level (E_F) for Ir in the second layer lead to higher PMA energy induced by other orbital such as xy and x^2-y^2 orbitals. A small shift in the fermi level (E_F) due to the application of voltage will drastically modify the PMA energy. Therefore, we obtained high VCMA when Ir was located in the second layer. Figure 3.9 (b) shows the VCDMI results. It can be seen that the VCDMI was altered by thickness of Ir suggest the VCMA and VCDMI is
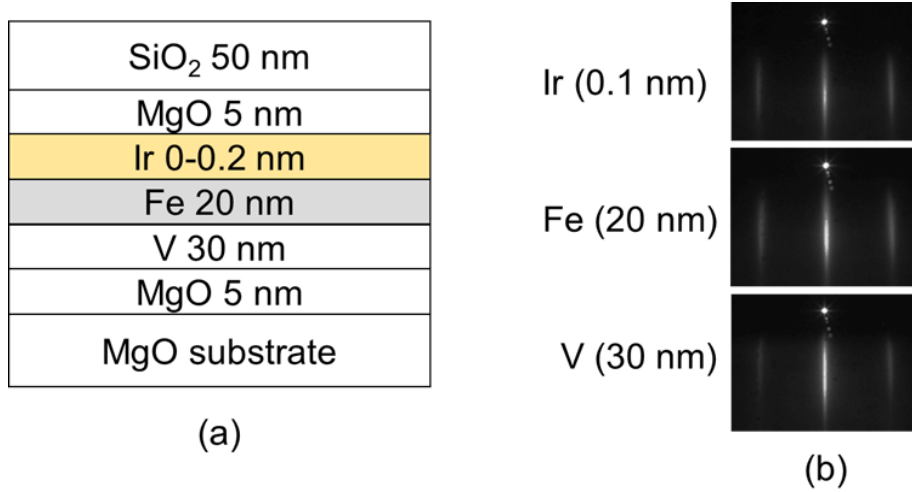
70

Figure 3.10: (a) Schematic of sample 2: Fe/Ir/MgO multilayers (b) the reflection high-energy electron diffraction (RHEED) image from the top surfaces of the V, Fe, and Ir, where the incident beam is aligned with the [100] direction of the MgO(001) substrate

not directly correlated. One might be interesting to see, the VCDMI of Ir/Fe/MgO exceed the Fe/Ir/MgO for some Ir thickness. First-principles calculation is required to revealed the origin of the observed result on VCDMI.

3.2.4. Influence of post-annealing on Fe/Ir/MgO

To investigate the influence of post-annealing to VCMA involving Fe and Ir, we prepared another sample with Ir insertion layer at Fe/MgO interface (sample 2). The schematic of multilayer structure is illustrated in Figure 3.10: (a). Streak patterns confirmed that the Ir layer has grown coherently onto the bcc-Fe(001) surface as depicted in Figure 3.10: (b). The sample then formed into spin wave device by microfabrication process to conduct VCMA and VCDMI characterization through spin wave spectroscopy.

The results of VCMA as a function of Ir thickness for different post-annealing temperature are summarized in Figure 3.11: The sample without annealing, represent by black line, showed the decreasing in VCMA as Ir thickness increase. On the other hand, by post-annealing treatment, the VCMA was enhanced at Ir thickness of 0.1 nm (0.5~ ML coverage). Increasing the annealing temperature from 250 to 300 °C increase the VCMA. These results suggest, the Ir diffusion into Fe layer due to annealing is responsible for VCMA enhancement. These observations qualitatively support the results from sample 1 when Ir intentional grown in the sublayer. Moreover, it is noteworthy, from these two samples (sample 1 and sample 2), the maximum VCMA was obtained at 0.1 nm Ir (0.5 ML coverage). Figure 3.11 (b) showed
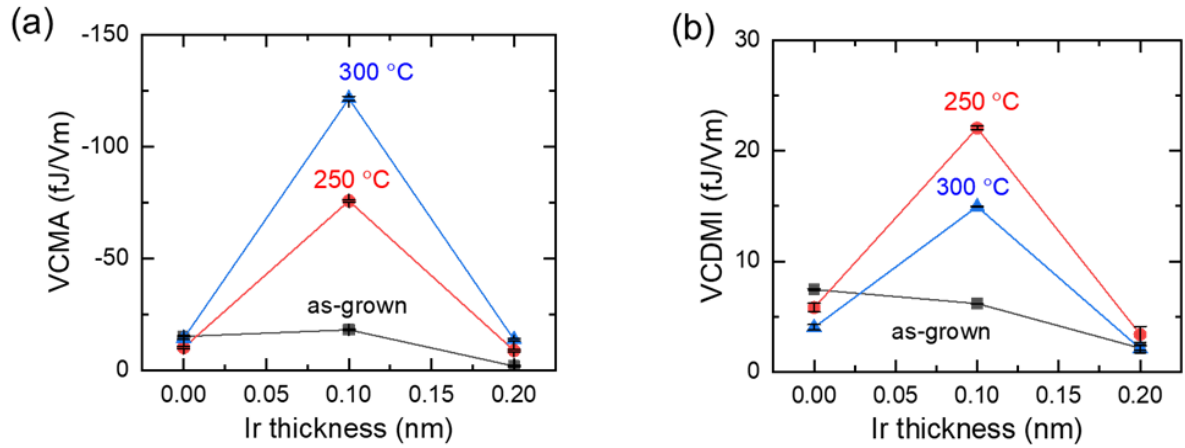
Figure 3.11: Ir thickness dependence of (a) VCMA and (b) VCDMI for Fe/Ir/MgO multilayer structure (Figure 3.10**:** (a) Schematic of sample 2: Fe/Ir/MgO multilayers (b) the reflection high-energy electron diffraction (RHEED) image from the top surfaces of the V, Fe, and Ir, where the incident beam is aligned with the [100] direction of the MgO(001) substrate a)) at different post-annealing temperature.

the VCDMI result of sample 2 for different annealing temperatures. As in VCMA, we observed the enhancement of VCDMI at Ir (0.1 nm) after post-annealing. However, the VCDMI might be very sensitive to Ir diffusion level, where the decreasing was observed when the annealing temperature increase from 250 to 300 °C. Nevertheless, to the best of our knowledge, this is the first observation the VCDMI magnitude that can be enhanced by post-annealing treatment.

3.2.5. Summary

We experimentally demonstrated the influence of Ir atoms location to voltage-controlled magnetic anisotropy (VCMA) and voltage-controlled Dzyaloshinskii-Moriya interaction (VCDMI). We obtained that the Ir placed in the second layer respect to MgO is effective to increase the VCMA efficiency. We obtained the maximum VCMA of -300 fJ/Vm in Ir(0.1 nm)/Fe/MgO. Moreover, the VCDMI was altered Ir thickness and location.

We investigated the influenced of post-annealing to VCMA and VCMDI in Fe/Ir/MgO by spin-wave spectroscopy measurement. The VCMA and VCDMI increase upon annealing due to the diffusion of Ir atoms to Fe layer. These two results from two different sample are qualitatively support each other, where the Ir atoms in the sublayer have large contribution to total VCMA and VCDMI in Fe(Ir)/MgO systems.

3.3. Control of the number of d-electron (Ni fraction dependence in Co$_{1-x}$Ni$_x$ layer)

In ferromagnetic metal, the VCMA effect arises from the charge accumulation [93], [102] and/or redistribution [52], [111], [112] at the ferromagnet/dielectric interface. Specifically, in $3d$-ferromagnets, the charge accumulation effect should be the dominant factor influencing VCMA. Therefore, controlling the number of $3d$ electrons (n) at the ferromagnet/MgO interface is important. It has been reported that the insertion of a monatomic layer of Co at the Fe/MgO interface increased the VCMA from 30 fJ/Vm to 80 fJ/Vm [93]. Moreover, a theoretical study predicted the VCMA in $3d$-ferromagnetic metals (Fe, Co, and Ni) as function of orbital filling, where the high VCMA obtained in Co-Ni alloy region [54]. Thus, we investigated the influence of changes in the number of $3d$ electrons, induced by Ni doping, on VCMA as well as voltage-controlled Dzyaloshinskii-Moriya interaction (VCDMI) at Co$_{1-x}$Ni$_x$/MgO interface. We deposited epitaxial Co$_{1-x}$Ni$_x$ film by sandwiching the Co wedges and Ni wedges in different direction which growth on top of bcc-Fe(001). The wedge was kept below 1 ML coverage, therefore, the Co and Ni wedges were forced to form the alloying. This way of growth was repeated two times lead to total about 2 ML coverage of Co$_{1-x}$Ni$_x$ layer on top of bcc-Fe. Moreover, to investigate the influence of the number of $3d$ electrons (n) on Pd/MgO interface, we also deposited Pd in some region. These results had been published in Japanese journal of applied physics.

3.3.1. Experimental

The structure of the multilayer is depicted in Figure 3.12 (a). Epitaxial layers of MgO(001) buffers /bcc-V(001)/bcc-Fe(001)/Co$_{1-x}$Ni$_x$/(Pd)/MgO (001) barriers were grown sequentially onto NaCl-type single-crystal MgO(001) substrates by molecular beam epitaxy under ultrahigh vacuum (base pressure ~10^{-8} Pa). To avoid intermixing, the MgO buffer was deposited at 150 °C. Then the V layer was deposited at 150 °C while the other layers were deposited at room temperature. In situ post annealing for the V and Fe layers were performed at 500 °C and 250 °C, respectively. A relatively thick 20 nm Fe layer is necessary for a high signal-to-noise ratio [69] in the microwave response of the spin-wave. The Co$_{1-x}$Ni$_x$ layer consisted of two alternating wedge-shaped layers of Co (max. thickness 0.14 nm corresponding to 1 monolayer coverage) and Ni (max. thickness 0.13 nm corresponding to 1 monolayer coverage), grown in opposite directions. By this way, Co and Ni are forced to form alloy on top of bcc-Fe. After that, some region is covered by Pd (0.18 nm). After the deposition of

another MgO barrier, the sample was removed from the vacuum. Finally, an additional layer of dielectric SiO_2 was deposited by RF sputtering.

The quality of each deposited layer was examined by in situ reflection high-energy electron diffraction. Figure 3.12(b) shows the reflection high-energy electron diffraction patterns from Fe (20 nm) and $Co_{1-x}Ni_x$ (x = 0, 0.5 and 1) surfaces, parallel to the MgO[100] direction. A streak reflection high-energy electron diffraction pattern is observed for $Co_{1-x}Ni_x$ and Pd on top of the bcc-Fe layer, indicating coherent growth. This is consistent with the X-ray photoelectron diffraction studies in [113], where bcc-Ni and Co monolayers are grown epitaxially on a bcc-Fe(001) substrate. Moreover, similar reflection high-energy electron diffraction patterns observed in all the region (x = 0, 0.5 and 1) indicate that the crystal structure of $Co_{1-x}Ni_x$ is independent of the Ni fraction x. There was no change in lattice spacing was observed, suggesting the bcc-lattice formation in all region $Co_{1-x}Ni_x$.

Evaluation of VCMA is primarily performed in ultra-thin ferromagnetic layers (typically 1-2 nm) by employing magnetic-tunnel junction structures. However, to study
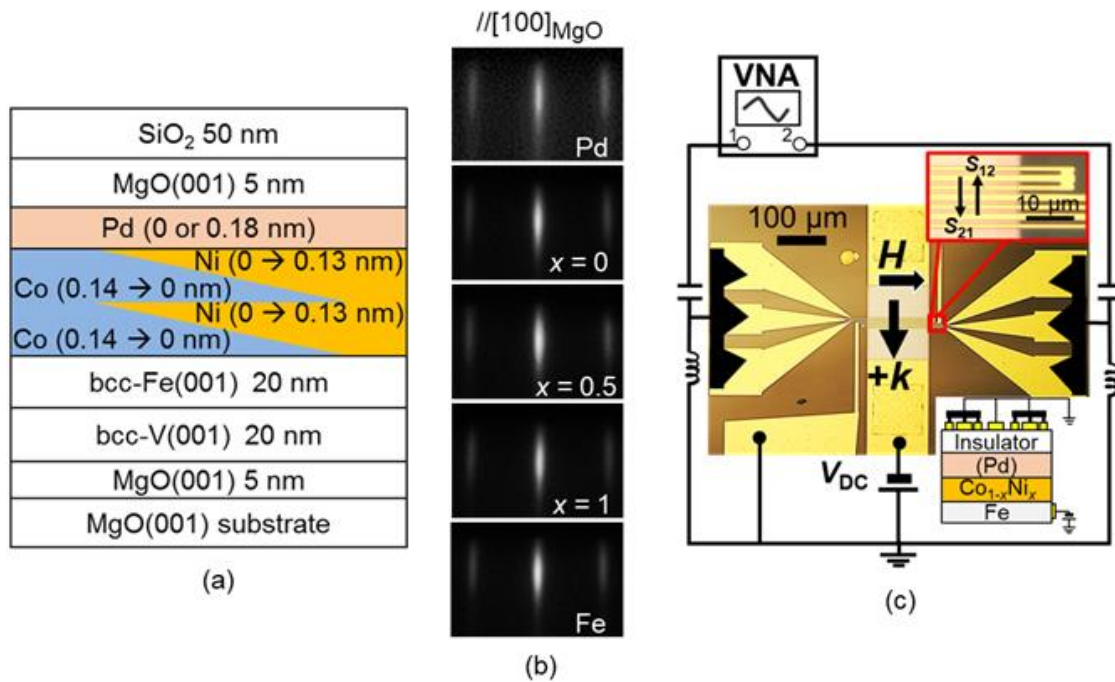
Figure 3.12: (a) Schematic representation of the multilayer structure. (b) In situ reflection high-energy electron diffraction images parallel to the MgO [100] direction acquired on top of the grown layer. From bottom to top: annealed Fe (20nm), $Co_{1-x}Ni_x$ (x = 0, 0.5 and 1), and Pd (0.2 nm) layer. (c) Top view of the spin-wave measurement sample and schematic measurement circuit.

VCMA for various thicknesses, spin-wave spectroscopy is advantageous in that it can be applied to systems having a wide-range of perpendicular magnetic anisotropy (i-PMA) [69], [114]. The multilayer was patterned into a 100×400 μm^2 rectangular sample by electron-beam lithography and ion-milling with the longer side parallel to the Fe[100] direction. Following this, micron-sized antennas (consisting of Cr (5 nm)/Au (200 nm)) acting as a coplanar waveguide and an intermediate gate electrode were fabricated. Figure 3.12(c) shows the schematic of the sample with the measurement circuit. The inset in Figure 3.12(c) depicts the two shorted-end antennas which consist of a 2 μm signal line between two 1 μm ground lines and an intermediate gate electrode. An external magnetic field ($\mu_0 H_{ext}$) was applied along the in-plane direction. To excite the magneto-static surface spin-wave (MSSW), we applied a -15 dBm (32 μW) radio frequency (RF) signal to the antennas. An external bias voltage (V_{dc}) was applied across the contact pad (connected to Fe-layer) and the intermediate gate electrode. The external bias voltage (V_{dc}) is positive (negative) when electron (hole) accumulated at ferromagnet/dielectric interface. This definition is same as in Ref.[7] for VCMA in magnetic tunnel junction. The interfacial PMA field ($\mu_0 H_{int}$), VCMA and VCDMI were characterized by analyzing the microwave response (S-parameters) using a vector network analyzer. The detailed analysis procedure to determine i-PMA field, VCMA and VCDMI from the MSSW signal can be found in previous section 3.1.1.
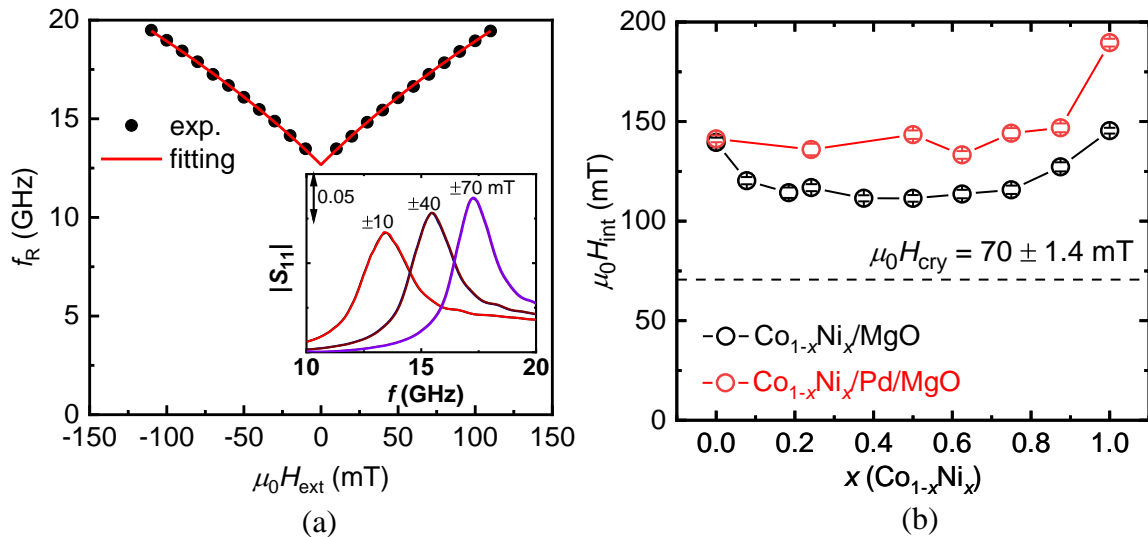
Figure 3.13: (a) Magneto-static surface spin-wave (MSSW) resonant-frequency (f_R) at various applied external magnetic fields ($\mu_0 H_{ext}$) for the Co$_{1-x}$Ni$_x$/MgO sample with $x = 0$. Inset shows the $|S_{11}|$ spectra from spin-wave spectroscopy measurement. (b) Interfacial perpendicular magnetic anisotropy ($\mu_0 H_{int}$) as function of Ni fraction x for Co$_{1-x}$Ni$_x$/MgO and Co$_{1-x}$Ni$_x$/Pd/MgO samples.

3.3.2. Evaluation of magnetic anisotropy field

The interfacial anisotropy field ($\mu_0 H_{int}$) and fourfold-crystalline anisotropy field ($\mu_0 H_{cry}$) of $Co_{1-x}Ni_x$/MgO and $Co_{1-x}Ni_x$/Pd/MgO are summarized in Figure 3.13(b). Due to large thickness difference of the insertion layer (Co, Ni, and Pd, <1 nm) in comparisons to Fe-layer (20 nm), their influences to saturation magnetization (M_s) and gyromagnetic ratio (γ_0) will be negligible. The $\mu_0 M_s$ and $\gamma_0/2\pi$ are the value for bulk-Fe and set to be constant 2.16 T and 2.94 $\times 10^{10}$ (Ts)$^{-1}$, respectively. Furthermore, we assume that $\mu_0 H_{cry}$ is almost constant (estimated to be 70 $\pm$ 1.4 mT), while $\mu_0 H_{int}$ is altered by changing the Ni fraction x. Positive values represent interfacial fields with a perpendicular orientation. In the $Co_{1-x}Ni_x$/MgO sample, the perpendicular anisotropy field $\mu_0 H_{int}$ decreases approximately 20% for $0.1 < x < 0.8$, while it increases for $x > 0.8$. Moreover, Co (0.28 nm)/MgO and Ni (0.26 nm)/MgO possess a similar i-PMA field $\mu_0 H_{int}$.

Upon introduction of a Pd layer between the $Co_{1-x}Ni_x$ and MgO layers, the scenario changes. Increasing the Ni concentration up to 80% now results in nearly the same $\mu_0 H_{int}$ as the pure Co sample. Interestingly, the $\mu_0 H_{int}$ shows enhancement in Ni/Pd/MgO ($x =1$), while for Co/Pd/MgO remains the same as in Co/MgO.
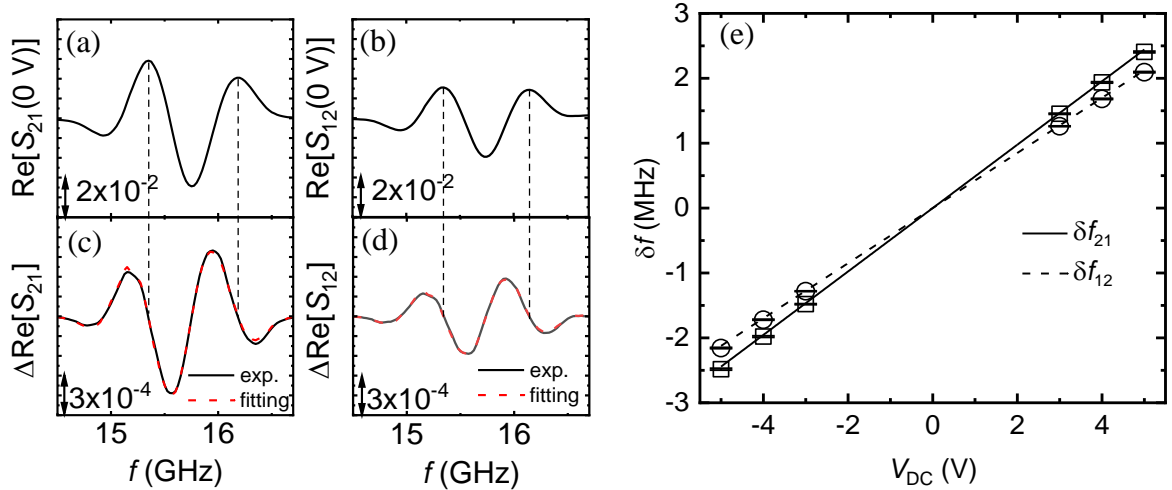
Figure 3.14: (a)-(b) Real part of propagating MSSW signal at 0 *V* for +k (S_{21}) and –k (S_{12}) propagation directions. (c)-(d) Solid black curve shows the subtracted propagating MSSW spectrum at bias-voltage V_{dc} = -5 V from 0 V when $\mu_0 H_{ext}$ = 40 mT is applied. Red dashed curve represents the voltage-induced frequency shift (δf) fitting by Eq (2). (e) Voltage-

induced frequency shift (δf) at various applied V_{dc}. Solid and dashed lines represent linear fitting of δf_{21} and δf_{12}, respectively.

3.3.3. Evaluation of VCMA and VCDMI

To analyze VCMA and VCDMI, spin-wave spectroscopy measurement was performed at $\mu_0 H_{ext} = 40$ mT by sweeping the external bias-voltage V_{dc} between ±5 V. The sample was modeled as two capacitors in series with dielectric constant of SiO$_2$ and MgO are $\varepsilon_{SiO2} = 3.9$ and $\varepsilon_{MgO} = 9.6$, respectively. The electric field in the MgO layer estimated by $E_{MgO} = (\varepsilon_{SiO2}/V)/(\varepsilon_{SiO2}d_{MgO} + \varepsilon_{MgO}d_{SiO2})$ to be 8 mV/nm at $V_{dc} = 1$ V. Figure 3.14(a-d) show the propagating spin-wave spectra of the Co$_{1-x}$Ni$_x$/MgO sample with $x = 0$. The difference in intensity between the real parts Re[S_{21}] and Re[S_{12}] occurred due to spatial rotation mismatch of the RF-field and the MSSW [92]. The upper figures (see Figure 3.14(a-b)) show Re[$S_{21(12)}$] spectra at $V_{dc} = 0$ V, while the ones below (Figure 3.14(c-d)) represent the subtracted signal ΔRe[$S_{21(12)}$] = Re[$S_{21(12)}$(-5 V)] - Re[$S_{21(12)}$(0 V)]. The subtracted signal ΔRe[$S_{21(12)}$] shifts to lower frequencies, indicating that the application of an external voltage affects the magnetic properties of the sample. This voltage-induced frequency shift (δf) can be expressed as:

$$\Delta \text{Re}[S_{21(12)}] = -\delta f_{21(12)} \frac{d\,\text{Re}[S_{21(12)}]}{df} \tag{3.7}$$

where dRe[$S_{21(12)}$(0 V)]/df represents the numerical differentiation of Re[$S_{21(12)}$] signal at $V_{dc} = 0$ V. This equation was used to fit the subtracted signal to quantize δf and the well-matched fitting, as shown in Figs. 3(c-d), was obtained. δf at different values of V_{dc} for Co$_{1-x}$Ni$_x$/MgO sample with $x = 0$ is summarized in Figure 3.14(e). As one can see, δf increases linearly with increase in the magnitude of V_{dc}. Furthermore, the differences observed in δf_{21} and δf_{12} suggest the occurrence of VCDMI in the sample.

Figure 3.15 shows VCMA and VCDMI as a function of x for Co$_{1-x}$Ni$_x$/MgO and Co$_{1-x}$Ni$_x$/Pd/MgO samples. For both samples, it can be seen that increasing the Ni fraction x decreased the VCMA. The highest VCMA of -270 fJ/Vm was obtained in the Co$_{1-x}$Ni$_x$ sample at $x = 0$ (pure Co/MgO interface). The VCMA polarities of Co/MgO and Ni/MgO are negative. This implies that the i-PMA energy decreases upon adding electrons. Zhang et al.[54] discussed the i-PMA energy in 3d-ferromagentic metals in terms of splitting of 3d-orbitals in a tetragonal crystal field. They discussed the i-PMA energy as a function of orbital band filling n, and predicted that the VCMA polarities in Fe, Co, and Ni are negative. Moreover, when the orbital band filling increases beyond $n = 6$ (Fe), the VCMA initially increase and then decreases,
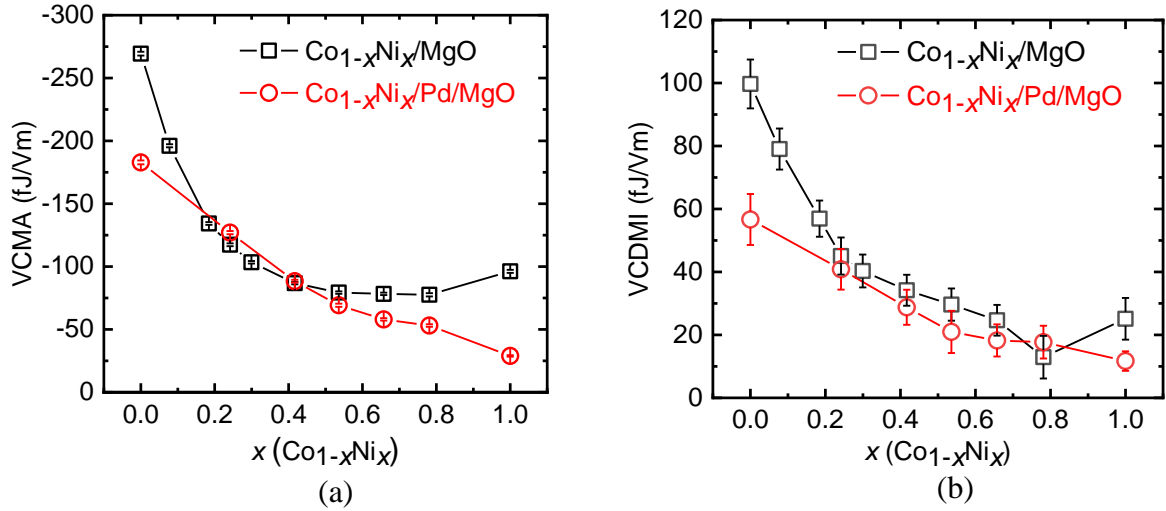
Figure 3.15: (a) VCMA and (b) VCDMI as a function of Ni fraction x in $Co_{1-x}Ni_x$/MgO and $Co_{1-x}Ni_x$/Pd/MgO system.

nearly vanishing around $n = 8.5$. Throughout this range, however, the VCMA polarity does not change. These observations are qualitatively consistent with our results, where the VCMA effect is maximum for a pure Co/MgO interface ($n = 7$).

In the $Co_{1-x}Ni_x$/Pd/MgO sample, due to electrostatic screening effects, the VCMA is attributed mainly to the Pd/MgO interface. Upon increase in the Ni fraction x, the VCMA of $Co_{1-x}Ni_x$/Pd/MgO decreases. It has been reported that the spin polarization in Pd induced by Ni is smaller than that induced by Co [115], [116]. This decrease of the magnetic moment in Pd could result in a decrease in VCMA effect when x increases. While the VCMA in both $Co_{1-x}Ni_x$/MgO and $Co_{1-x}Ni_x$/Pd/MgO systems decreases as a function of x, it is interesting to note that this decrease is more gradual in $Co_{1-x}Ni_x$/Pd/MgO compared to $Co_{1-x}Ni_x$/MgO. It has been reported that the VCMA effect is proportional to the voltage-induced change of the anisotropy of spin-orbit interaction energy, which is proportional to the voltage-induced changes of the anisotropies in orbital magnetic moment and a part of magnetic dipole T_z term [52]. Here, the magnetic dipole T_z term is an expectation value of the magnetic dipole operator: $\langle \mathbf{T} \rangle \equiv \langle \mathbf{Q} \cdot \mathbf{S} \rangle$, where $\mathbf{Q}$ and $\mathbf{S}$ are dimension-less charge-quadrupole operator and spin angular momentum, respectively. Note that both anisotropy and its voltage-induced changes of $\mathbf{T}$ mainly originate from $\mathbf{Q}$ because $\mathbf{S}$ is isotropic and is insensitive to voltage application. Therefore, voltage-induced changes of the magnetic dipole T_z term is roughly proportional to the magnitude of spin magnetic moment. From the discussion above, the VCMA effect would be larger when the size of the magnetic moments is larger. The changes of the VCMA effect in $Co_{1-x}Ni_x$/Pd/MgO might be correlated to the size of the induced magnetic moment in Pd. Here, the

aforementioned discussion about the magnetic dipole T_z term might be applicable only for $4d$ and $5d$, not for $3d$ transition metals.

Figure 3.15 (b) shows the Ni fraction dependence of VCDMI for $Co_{1-x}Ni_x$/MgO and $Co_{1-x}Ni_x$/Pd/MgO. Interfacial DMI (i-DMI), which is an antisymmetric exchange interaction, mainly occurs at the interface between a FM metal and a heavy metal [67], [103], [117]. Recently, it has been demonstrated through ab-initio calculations [107] and experiments [108], [118], [119] that the Co/oxide interface also features i-DMI. In our system, the i-DMI effect should be present in the top and bottom layers of FM layer interface. However, as in VCMA, the VCDMI is attributed to a change in magnetic properties only in the interface between the FM layer and MgO. For VCDMI, a value comparable to the VCMA coefficient was obtained, where the maximum value of 100 fJ/Vm was found in the $Co_{1-x}Ni_x$/MgO sample at $x = 0$ (see Figure 3.15(b)). One can see that the behavior of VCDMI is similar to that of VCMA in CoNi(Pd)/MgO multilayer system while such tendency is not always the case for other systems.

3.3.4. Summary

In summary, we conducted spin-wave spectroscopy in $Co_{1-x}Ni_x$/MgO and $Co_{1-x}Ni_x$/Pd/MgO multilayers to investigate VCMA and VCDMI. We found that pure Co as the $3d$ ferromagnetic layer has the maximum VCMA and VCDMI. Moreover, the VCMA and VCDMI have a comparable magnitude and can be simultaneously tuned by voltage. Our findings can pave way for the development of (Co, Ni)/MgO based voltage-driven spintronic devices utilizing VCMA [41] and VCDMI [64] effects.

Chapter 4 Conclusion

In conclusion, by engineered the interface of Fe/MgO, voltage-controlled magnetic anisotropy (VCMA) and voltage-controlled Dzyaloshinskii-Moriya interaction (VCDMI) were controlled and/or enhanced. In details, by three interface engineering approaches:

1. Atomic layer insertion (Co/Pd combination),

I have utilized the Co/Pd atomic layer insertion with various thicknesses. It was found that the presence of Pd decreases the VCMA in Fe/MgO but increase in Co/MgO interface. Maximum VCMA of -180 fJ/Vm was obtained in Fe/Co/Pd/MgO, (Pd thickness about one-monolayer coverage) which is more than three times higher than VCMA in Fe/MgO. Moreover, the VCDMI was increased simultaneously and having a comparable value to VCMA. The maximum VCDMI of 65 fJ/Vm was obtained in Fe/Co/MgO. Furthermore, the post-annealing process monotonically reduced VCMA and VCDMI. Therefore, I concluded that layered multilayers, rather than alloys, provide the best conditions for manipulating VCMA and VCDMI in Fe/Co/Pd/MgO systems.

2. Artificial alloy-formation (Ir location control in Fe layer), and

I investigated the Ir location influenced by controlling Ir growth in between Fe atoms. I experimentally demonstrated that placing the Ir in the second layer from MgO was effective to enhance the VCMA. Maximum VCMA of -300 fJ/Vm was obtained in Ir/Fe/MgO with Ir thickness of 0.1-nm (0.5 monolayer). Moreover, the VCDMI was also altered Ir thickness and locations.

3. Control of the number of d-electron (Ni fraction dependence in $Co_{1-x}Ni_x$ layer)

I studied the influence of the number of d-electron by changing the composition in $Co_{1-x}Ni_x$ alloy which deposited on top of body-centered cubic (bcc)-Fe. Increasing the Ni fraction x decreased the VCMA and VCDMI in the systems. These results reflected the occupancy of d-band electron. I found that pure-Co as the $3d$ ferromagnetic layer has the maximum VCMA (-270 fJ/Vm) and VCDMI (-100 fJ/Vm).

These results might be important for the development of voltage-driven MRAM.

Acknowledgments

Reference

[1] J. A. Katine, F. J. Albert, R. A. Buhrman, E. B. Myers, and D. C. Ralph, "Current-Driven Magnetization Reversal and Spin-Wave Excitations in Co/Cu/Co Pillars," *Phys. Rev. Lett.*, vol. 84, no. 14, p. 3149, 2000.

[2] K. Ando, S. Fujita, J. Ito, S. Yuasa, Y. Suzuki, Y. Nakatani, T. Miyazaki, and H. Yoda, "Spin-transfer torque magnetoresistive random-access memory technologies for normally off computing (invited)," *J. Appl. Phys.*, vol. 115, p. 172607, 2014.

[3] R. Landauer, "Irreversibility and Heat Generation in the Computing Process," *IBM J. Res. Dev.*, vol. 44, no. 1/2, pp. 261–269, 2000.

[4] M. Weisheit, S. Fahler, A. Marty, Y. Souche, C. Poinsignon, and D. Givord, "Electric Field-Induced Modification of Magnetism in Thin-Film Ferromagnets," *Science (80-.).*, vol. 315, no. 5810, pp. 349–351, 2007.

[5] T. Maruyama, Y. Shiota, T. Nozaki, K. Ohta, N. Toda, M. Mizuguchi, A. A. Tulapurkar, T. Shinjo, M. Shiraishi, S. Mizukami, Y. Ando, and Y. Suzuki, "Large voltage-induced magnetic anisotropy change in a few atomic layers of iron," *Nat. Nanotechnol.*, vol. 4, no. 3, pp. 158–161, 2009.

[6] P. K. Amiri, J. G. Alzate, X. Q. Cai, F. Ebrahimi, Q. Hu, K. Wong, C. Grèzes, H. Lee, G. Yu, X. Li, M. Akyol, Q. Shao, J. A. Katine, J. Langer, B. Ocker, and K. L. Wang, "Electric-Field-Controlled Magnetoelectric RAM: Progress, Challenges, and Scaling," *IEEE Trans. Magn.*, vol. 51, no. 11, p. 3401507, 2015.

[7] T. Nozaki, Y. Shiota, M. Shiraishi, T. Shinjo, and Y. Suzuki, "Voltage-induced perpendicular magnetic anisotropy change in magnetic tunnel junctions," *Appl. Phys. Lett.*, vol. 96, p. 022506, 2010.

[8] Y. Shiota, T. Nozaki, F. Bonell, S. Murakami, T. Shinjo, and Y. Suzuki, "Induction of coherent magnetization switching in a few atomic layers of FeCo using voltage pulses," *Nat. Mater.*, vol. 11, no. 1, pp. 39–43, 2012.

[9] S. Kanai, M. Yamanouchi, S. Ikeda, Y. Nakatani, F. Matsukura, and H. Ohno, "Electric field-induced magnetization reversal in a perpendicular-anisotropy CoFeB-MgO magnetic tunnel junction," *Appl. Phys. Lett.*, vol. 101, p. 122403, 2012.

[10] C. Grezes, F. Ebrahimi, J. G. Alzate, X. Cai, J. A. Katine, J. Langer, B. Ocker, P. Khalili Amiri, and K. L. Wang, "Ultra-low switching energy and scaling in electric-field-controlled nanoscale magnetic tunnel junctions with high resistance-area product," *Appl. Phys. Lett.*, vol. 108, p. 012403, 2016.

[11] T. Nozaki, Y. Shiota, S. Miwa, S. Murakami, F. Bonell, S. Ishibashi, H. Kubota, K. Yakushiji, T. Saruya, A. Fukushima, S. Yuasa, T. Shinjo, and Y. Suzuki, "Electric-field-induced ferromagnetic resonance excitation in an ultrathin ferromagnetic metal layer," *Nat. Phys.*, vol. 8, no. 6, pp. 491–496, 2012.

[12] J. Zhu, J. A. Katine, G. E. Rowlands, Y. J. Chen, Z. Duan, J. G. Alzate, P. Upadhyaya, J. Langer, P. K. Amiri, K. L. Wang, and I. N. Krivorotov, "Voltage-induced ferromagnetic resonance in magnetic tunnel junctions," *Phys. Rev. Lett.*, vol. 108, p. 197203, 2012.

[13] M. N. Baibich, J. M. Broto, A. Fert, F. N. Van Dau, F. Petroff, P. Eitenne, G. Creuzet, A. Friederich, and J. Chazelas, "[Nanoscale Combination] Giant magnetoresistance of (001)Fe/(001)Cr magnetic superlattices," *Phys. Rev. Lett.*, vol. 61, no. 21, pp. 2472–2475, 1988.

[14] S. A. Wolf, D. D. Awschalom, R. A. Buhrman, J. M. Daughton, S. von Molnár, M. L. Roukes, A. Y. Chtchelkanova, and D. M. Treger, "Spintronics: A Spin-Based Electronics Vision for the Future," *Science (80-.).*, vol. 294, p. 1488, 2001.

[15] T. Miyazaki and N. Tezuka, "Giant Magnetic Tunneling Effect in Fe/Al2O3/Fe Junction," *J. Magn. Magn. Mater.*, vol. 139, pp. L231–L234, 1995.

[16] J. S. Moodera, L. R. Kinder, M. T. Wong, and R. Meservey, "Large magnetoresistance at room temperature in ferromagnetic thin film tunnel junctions," *Phys. Rev. Lett.*, vol. 74, no. 16, p. 3273, 1995.

[17] W. H. Butler, X. Zhang, and T. C. Schulthess, "Spin-dependent tunneling conductance of Fe|MgO|Fe sandwiches," *Phys. Rev. B*, vol. 63, p. 054416, 2001.

[18] J. Mathon and A. Umerski, "J. Mathon and A. Umerski," *Phys. Rev. B*, vol. 63, p. 220403(R), 2001.

[19] S. Yuasa, T. Nagahama, A. Fukushima, Y. Suzuki, and K. Ando, "Giant room-temperature magnetoresistance in single-crystal Fe/MgO/Fe magnetic tunnel junctions,"

Nat. Mater., vol. 3, no. 12, pp. 868–871, 2004.

[20] S. S. P. Parkin, C. Kaiser, A. Panchula, P. M. Rice, B. Hughes, M. Samant, and S. H. Yang, "Giant tunnelling magnetoresistance at room temperature with MgO (100) tunnel barriers," *Nat. Mater.*, vol. 3, no. 12, pp. 862–867, 2004.

[21] D. D. Djayaprawira, K. Tsunekawa, M. Nagai, H. Maehara, S. Yamagata, N. Watanabe, S. Yuasa, Y. Suzuki, and K. Ando, "Room-temperature magnetoresistance in CoFeB/MgO/CoFeB magnetic tunnel junctions," *J. Magn. Magn. Mater.*, vol. 86, p. 092502, 2005.

[22] S. Ikeda, J. Hayakawa, Y. Ashizawa, Y. M. Lee, K. Miura, H. Hasegawa, M. Tsunoda, F. Matsukura, and H. Ohno, "Tunnel magnetoresistance of 604% at 300 K by suppression of Ta diffusion in CoFeB/MgO/CoFeB pseudo-spin-valves annealed at high temperature," *Appl. Phys. Lett.*, vol. 93, p. 082508, 2008.

[23] S. Tehrani, B. Engel, E. Chen, M. DeHerrera, M. Durlam, and J. M. Slaughter, "Recent developments in magnetic tunnel junction MRAM," *IEEE Trans. Magn.*, vol. 36, no. 5, p. 2752, 2000.

[24] S. Bhatti, R. Sbiaa, A. Hirohata, H. Ohno, S. Fukami, and S. N. Piramanayagam, "Spintronics based random access memory: a review," *Mater. Today*, vol. 20, no. 9, pp. 530–548, 2017.

[25] D. C. Ralph and M. D. Stiles, "Spin transfer torques," *J. Magn. Magn. Mater.*, vol. 320, pp. 1190–1216, 2008.

[26] T. Nozaki, T. Yamamoto, S. Miwa, and M. Tsujikawa, "Recent Progress in the Voltage-Controlled Magnetic Anisotropy E ff ect and the Challenges Faced in Developing Voltage-Torque MRAM," *micromachines*, vol. 10, p. 327, 2019.

[27] P. F. Carcia, A. D. Meinhaldt, and A. Suna, "Perpendicular magnetic anisotropy in Pd/Co thin film layered structures," *Appl. Phys. Lett.*, vol. 47, no. 2, pp. 178–180, 1985.

[28] L. L. Néel, "Anisotropie superficielle des substances ferromagnetiques," *C.R. Acad. Sci. Paris*, vol. 237, p. 1468, 1953.

[29] M. T. Johnson, P. J. H. Bloemen, F. J. A. den Broeder, and J. J. De Vries, "Magnetic anistoropy in metallic multilayers," *Rep. Prog. Phys.*, vol. 59, p. 1409, 1996.

[30] B. Dieny and M. Chshiev, "Perpendicular magnetic anisotropy at transition metal/oxide interfaces and applications," *Rev. Mod. Phys.*, vol. 89, p. 025008, 2017.

[31] P. F. Carcia, "Perpendicular magnetic anisotropy in Pd/Co and Pt/Co thin-film layered structures," *J. Appl. Phys.*, vol. 63, no. 10, p. 5066, 1988.

[32] S. Monso, B. Rodmacq, S. Aufrret, G. Casali, F. Fettar, B. Gilles, B. Dieny, and P. Boyer, "Crossover from in-plane to perpendicular anisotropy in Pt/CoFe/AlO$_x$ sandwiches as a function of Al oxidation : A very accurate control of the oxidation of tunnel barriers," vol. 80, p. 4157, 2002.

[33] C. H. Lambert, A. Rajanikanth, T. Hauet, S. Mangin, E. E. Fullerton, and S. Andrieu, "Quantifying perpendicular magnetic anisotropy at the Fe-MgO(001) interface," *Appl. Phys. Lett.*, vol. 102, p. 122410, 2013.

[34] V. Novosad, Y. Otani, A. Ohsawa, S. G. Kim, K. Fukamichi, J. Koike, K. Maruyama, O. Kitakami, and Y. Shimada, "Novel magnetostrictive memory device," *J. Appl. Phys.*, vol. 87, no. 9, pp. 6400–6402, 2002.

[35] H. Ohno, D. Chiba, F. Matsukura, T. Omiya, E. Abe, T. Dietl, Y. Ohno, and K. Ohtani, "Electric-field control of ferromagnetism," *Nature*, vol. 408, pp. 944–946, 2000.

[36] D. Chiba, S. Fukami, K. Shimamura, N. Ishiwata, K. Kobayashi, and T. Ono, "Electrical control of the ferromagnetic phase transition in cobalt at room temperature," *Nat. Mater.*, vol. 10, no. 11, pp. 853–856, 2011.

[37] N. A. Spaldin and F. Manfred, "The Renaissance of Magnetoelectric Multiferroics," *Science (80-.).*, vol. 309, pp. 391–392, 2005.

[38] Y. Shiota, S. Murakami, F. Bonell, T. Nozaki, T. Shinjo, and Y. Suzuki, "Quantitative evaluation of voltage-induced magnetic anisotropy change by magnetoresistance measurement," *Appl. Phys. Express*, vol. 4, no. 4, pp. 2–5, 2011.

[39] W. Wang, M. Li, S. Hageman, and C. L. Chien, "Electric-field-assisted switching in magnetic tunnel junctions," *Nat. Mater.*, vol. 11, no. 1, pp. 64–68, 2011.

[40] S. Kanai, Y. Nakatani, M. Yamanouchi, S. Ikeda, H. Sato, F. Matsukura, and H. Ohno, "Magnetization switching in a CoFeB/MgO magnetic tunnel junction by combining spin-transfer torque and electric field-effect," *Appl. Phys. Lett.*, vol. 104, p. 212406, 2014.

[41]   S. Miwa, M. Suzuki, M. Tsujikawa, T. Nozaki, T. Nakamura, S. Masafumi, S. Yuasa, and Y. Suzuki, "Perpendicular magnetic anisotropy and its electric-field-induced change at metal-dielectric interfaces," *J. Phys. D. Appl. Phys.*, vol. 52, p. 063001, 2019.

[42]   W. Skowronski, T. Nozaki, Y. Shiota, S. Tamaru, K. Yakushiji, H. Kubota, A. Fukushima, S. Yuasa, and S. Yoshishige, "Perpendicular magnetic anisotropy of Ir/CoFeB/MgO trilayer system tuned by electric fields," *Appl. Phys. Express*, vol. 8, p. 053003, 2015.

[43]   X. Li, K. Fitzell, D. Wu, C. T. Karaba, A. Buditama, G. Yu, K. L. Wong, N. Altieri, C. Grezes, N. Kioussis, S. Tolbert, Z. Zhang, J. P. Chang, P. Khalili Amiri, and K. L. Wang, "Enhancement of voltage-controlled magnetic anisotropy through precise control of Mg insertion thickness at CoFeB|MgO interface," *Appl. Phys. Lett.*, vol. 110, p. 052401, 2017.

[44]   C. G. Duan, J. P. Velev, R. F. Sabirianov, Z. Zhu, J. Chu, S. S. Jaswal, and E. Y. Tsymbal, "Surface magnetoelectric effect in ferromagnetic metal films," *Phys. Rev. Lett.*, vol. 101, p. 137201, 2008.

[45]   K. Nakamura, R. Shimabukuro, Y. Fujiwara, T. Akiyama, and T. Ito, "Giant Modification of the Magnetocrystalline Anisotropy in Transition-Metal Monolayers by an External Electric Field," vol. 102, p. 187201, 2009.

[46]   M. Tsujikawa and T. Oda, "Finite Electric Field Effects in the Large Perpendicular Magnetic Anisotropy Surface Pt/Fe/Pt (001) : A First-Principles Study," vol. 102, p. 247203, 2009.

[47]   S. E. Barnes, J. Ieda, and S. Maekawa, "Rashba Spin-Orbit Anisotropy and the Electric Field Control of Magnetism," *Sci. Rep.*, vol. 4, p. 4105, 2014.

[48]   P. V. Ong, N. Kioussis, D. Odkhuu, P. Khalili Amiri, K. L. Wang, and G. P. Carman, "Giant voltage modulation of magnetic anisotropy in strained heavy metal/magnet/insulator heterostructures," *Phys. Rev. B - Condens. Matter Mater. Phys.*, vol. 92, p. 020407(R), 2015.

[49]   K. Nakamura, T. Nomura, A.-M. Pradipto, K. Nawa, T. Akiyama, and T. Ito, "Effect of heavy-metal insertions at Fe/MgO interfaces on electric-field-induced modification of magnetocrystalline anisotropy," *J. Magn. Magn. Mater.*, vol. 429, pp. 214–220, 2017.

[50] T. Bonaedy, J. W. Choi, C. Jang, B. C. Min, and J. Chang, "Enhancement of electric-field-induced change of magnetic anisotropy by interface engineering of MgO magnetic tunnel junctions," *J. Phys. D. Appl. Phys.*, vol. 48, no. 22, 2015.

[51] T. Nozaki, A. Kozioł-Rachwał, M. Tsujikawa, Y. Shiota, X. Xu, T. Ohkubo, T. Tsukahara, S. Miwa, M. Suzuki, S. Tamaru, H. Kubota, A. Fukushima, K. Hono, M. Shirai, Y. Suzuki, and S. Yuasa, "Highly efficient voltage control of spin and enhanced interfacial perpendicular magnetic anisotropy in iridium-doped Fe/MgO magnetic tunnel junctions," *NPG Asia Mater.*, vol. 9, no. 12, pp. 1–10, 2017.

[52] S. Miwa, M. Suzuki, M. Tsujikawa, K. Matsuda, T. Nozaki, K. Tanaka, T. Tsukahara, K. Nawaoka, M. Goto, Y. Kotani, T. Ohkubo, F. Bonell, E. Tamura, K. Hono, T. Nakamura, M. Shirai, S. Yuasa, and Y. Suzuki, "Voltage controlled interfacial magnetism through platinum orbits," *Nat. Commun.*, vol. 8, p. 15848, 2017.

[53] P. Kamp, A. Marty, B. Gilles, R. Hoffmann, S. Marchesini, M. Belakhovsky, C. Boeglin, H. A. Durr, S. S. Dhesi, G. van der Laan, and A. Rogalev, "Correlation of spin and orbital anisotropies with chemical order in $Fe_{0.5}Pd_{0.5}$ alloy films using magnetic circular x-ray dichroism," *Phys. Rev. B*, vol. 59, no. 2, pp. 1105–1112, 1999.

[54] J. Zhang, P. V. Lukashev, S. S. Jaswal, and E. Y. Tsymbal, "Model of orbital populations for voltage-controlled magnetic anisotropy in transition-metal thin films," *Phys. Rev. B*, vol. 96, p. 014435, 2017.

[55] I. E. Dzialoshinkskii, "Thermodynamic theory of 'Weak' Ferromagnetism in antiferromagnetic substance," *Sov. Phys. JETP*, vol. 5, no. 6, pp. 1259–1272, 1957.

[56] T. Moriya, "Anisotropic superexchange interaction and weak ferromagnetism," *Phys. Rev.*, vol. 120, no. 1, p. 91, 1960.

[57] A. Fert and P. M. Levy, "Role of anisotropy exchange interaction in determining the properties of spin-glasses," *Phys. Rev. Lett.*, vol. 44, no. 23, p. 1538, 1980.

[58] J. Z. Zhao, X. Q. Wang, T. Xiang, Z. B. Su, and L. Yu, "Effects of the Dzyaloshinskii-Moriya Interaction on Low-Energy Magnetic Excitations in Copper Benzoate," *Phys. Rev. Lett.*, vol. 90, no. 20, p. 207204, 2003.

[59] D. Coffey, T. M. Rice, and F. C. Zhang, "Dzyaloshinskii-Moriya interaction in the cuprates," *Phys. Rev. B*, vol. 44, no. 18, pp. 10112–10116, 1991.

[60] I. A. Sergienko and E. Dagotto, "Role of the Dzyaloshinskii-Moriya interaction in multiferroic perovskites," *Phys. Rev. B - Condens. Matter Mater. Phys.*, vol. 73, p. 094434, 2006.

[61] S. Mühlbauer, B. Binz, F. Jonietz, C. Pfleiderer, A. Rosch, A. Neubauer, R. Georgii, and P. Böni, "Skyrmion Lattice in a Chiral Magnet," *Science (80-.).*, vol. 232, no. 5916, pp. 915–919, 2009.

[62] A. Fert, V. Cros, and J. Sampaio, "Skyrmions on the track," *Nat. Nanotechnol.*, vol. 8, pp. 152–156, 2013.

[63] A. Fert, N. Reyren, and V. Cros, "Magnetic skyrmions: Advances in physics and potential applications," *Nat. Rev. Mater.*, vol. 2, 2017.

[64] H. Imamura, T. Nozaki, S. Yuasa, and Y. Suzuki, "Deterministic Magnetization Switching by Voltage Control of Magnetic Anisotropy and Dzyaloshinskii-Moriya Interaction under an In-Plane Magnetic Field," *Phys. Rev. Appl.*, vol. 10, p. 054039, 2018.

[65] K. Di, V. L. Zhang, H. S. Lim, S. C. Ng, and M. H. Kuok, "Direct Observation of the Dzyaloshinskii-Moriya Interaction in a Pt / Co / Ni Film," vol. 114, p. 047201, 2015.

[66] K. Zakeri, Y. Zhang, J. Prokop, T. H. Chuang, N. Sakr, W. X. Tang, and J. Kirschner, "Asymmetric spin-wave dispersion on Fe(110): Direct evidence of the dzyaloshinskii-moriya interaction," *Phys. Rev. Lett.*, vol. 104, p. 137203, 2010.

[67] J. Cho, N. H. Kim, S. Lee, J. S. Kim, R. Lavrijsen, A. Solignac, Y. Yin, D. S. Han, N. J. J. Van Hoof, H. J. M. Swagten, B. Koopmans, and C. Y. You, "Thickness dependence of the interfacial Dzyaloshinskii-Moriya interaction in inversion symmetry broken systems," *Nat. Commun.*, vol. 6, p. 7635, 2015.

[68] J. M. Lee, C. Jang, B. C. Min, S. W. Lee, K. J. Lee, and J. Chang, "All-Electrical Measurement of Interfacial Dzyaloshinskii-Moriya Interaction Using Collective Spin-Wave Dynamics," *Nano Lett.*, vol. 16, no. 1, pp. 62–67, 2016.

[69] K. Nawaoka, S. Miwa, Y. Shiota, N. Mizouchi, and Y. Suzuki, "Voltage induction of interfacial Dzyaloshinskii–Moriya interaction in Au/Fe/MgO artificial multilayer," *Appl. Phys. Express*, vol. 8, p. 063004, 2015.

[70] A. Thiaville, S. Rohart, É. Jué, V. Cros, and A. Fert, "Dynamics of Dzyaloshinskii

domain walls in ultrathin magnetic films," *Epl*, vol. 100, no. 5, 2012.

[71]   A. Hubert and R. Schafer, *Magnetic Domain : the analysis and magnetic microstructures*. Berlin: Springer Berlin Heidelberg, 1998.

[72]   W. Heisenberg, "Zur Theorie des Ferromagnetismus," *Z. Phys.*, vol. 49, p. 619, 1928.

[73]   S. Chikazumi, *Physics of Ferromagnetism*, 2nd ed. New York: Oxford University Press, 1997.

[74]   J. M. D. Coey, *Magnetism and magnetic materials*. New York: Cambridge University Press, 2009.

[75]   B. D. Cullity and C. D. Graham, *Introduction to magnetic materials*, 2nd ed. New Jersey: John Wiley & Sons, 2009.

[76]   D. L. Landau and E. Lifshitz, "On the theory of damping in ferromagnetic bodies," *Phys. Z. Sowjetunion*, vol. 8, p. 153, 1935.

[77]   A. Barman and A. Haldar, "Time-domain study of magnetization dynamics in magnetic thin films and micro- and nanostructures," in *Solid-State Physics*, 65th ed., R. E. Camley and R. L. Stamps, Eds. Elsevier, 2014, p. 16.

[78]   D. D. Stancil and A. Prabhakar, *Spin Waves : Theory and Applications*. New York: Springer, 2009.

[79]   M. S. Sodha and N. C. Srivastava, *Microwave Propagation in Ferrimagnetics*. New York, 1981.

[80]   K. Nawaoka, "Voltage modulation of interfacial Dyzaloshinkii-Moriya interaction in artificial multilayer," Osaka University, 2017.

[81]   J. H. Moon, S. M. Seo, K. J. Lee, K. W. Kim, J. Ryu, H. W. Lee, R. D. McMichael, and M. D. Stiles, "Spin-wave propagation in the presence of interfacial Dzyaloshinskii-Moriya interaction," *Phys. Rev. B*, vol. 88, p. 184404, 2013.

[82]   P. Karen, A. Kjekshus, Q. Huang, and V. L. Karen, "The crystal structure of magnesium dicarbide," *J. Alloys Compd.*, vol. 282, pp. 72–75, 1999.

[83]   R. Kuentzler and H. R. Khan, "Low temperature spesific heat and superconductivity measurement of $V_{1-x}Ti_x$: T=Ti, Zr, Hf and x =0.013 and 0.05," *Phys. Lett.*, vol. 113A, pp. 89–92, 1985.

[84] E. P. Yelsukov, E. V. Voronina, and V. A. Barinov, "Mössbauer study of magnetic properties formation in disordered Fe-Al alloys," *J. Magn. Magn. Mater.*, vol. 115, pp. 271–280, 1992.

[85] T. Pan, G. W. D. Spratt, L. Tang, and D. E. Laughlin, "Magnetic properties and microstructure of evaporated Co oxide tape media," *J. Magn. Magn. Mater.*, vol. 155, pp. 309–311, 1996.

[86] van R. P. Ingen, R. H. J. Fastenau, and E. J. Mittemeijer, "Laser ablation deposition of Cu-Ni and Ag-Ni films: Nonconservation of alloy composition and film microstructure," *J. Appl. Phys.*, vol. 76, p. 1871, 1994.

[87] Y. Sakamoto, F. L. Chen, and R. A. McNicholl, "Thermodynamic studies of hydrogen solution in palladium-scandium alloys.," *J. Alloys Compd.*, vol. 192, pp. 145–148, 1993.

[88] M. Ellner, K. Kolatschek, and B. Predel, "On the partial atomic volume and the partial molar enthalpy of aluminium in some phases with Cu and Cu_3Au structures," *J. Less-Common Met.*, vol. 170, pp. 171–184, 1991.

[89] A. Kozioł-Rachwał, T. Nozaki, V. Zayets, H. Kubota, A. Fukushima, S. Yuasa, and Y. Suzuki, "The effect of the MgO buffer layer thickness on magnetic anisotropy in MgO/Fe/Cr/MgO buffer/MgO(001)," *J. Appl. Phys.*, vol. 120, p. 085303, 2016.

[90] A. Technologies., "Application Note 1287-1: Understanding the Fundamental Principles of Vector Network Analysis.," *Agil. U.S.A., 2000*.

[91] F. Gardiol, *Microstrip circuits*. New York: Wiley, 1994.

[92] V. E. Demidov, M. P. Kostylev, K. Rott, P. Krzysteczko, G. Reiss, and S. O. Demokritov, "Excitation of microwaveguide modes by a stripe antenna," *Appl. Phys. Lett.*, vol. 95, p. 112509, 2009.

[93] T. Kawabe, K. Yoshikawa, M. Tsujikawa, T. Tsukahara, K. Nawaoka, Y. Kotani, K. Toyoki, M. Goto, M. Suzuki, T. Nakamura, M. Shirai, Y. Suzuki, and S. Miwa, "Electric-field-induced changes of magnetic moments and magnetocrystalline anisotropy in ultrathin cobalt films," *Phys. Rev. B*, vol. 96, p. 220412(R), 2017.

[94] Y. Hibino, T. Koyama, A. Obinata, K. Miwa, S. Ono, and D. Chiba, "Electric field modulation of magnetic anisotropy in perpendicularly magnetized Pt/Co structure with a Pd top layer," *Appl. Phys. Express*, vol. 8, p. 113002, 2015.

[95] Y. Hibino, T. Koyama, A. Obinata, T. Hirai, S. Ota, K. Miwa, S. Ono, F. Matsukura, H. Ohno, and D. Chiba, "Peculiar temperature dependence of electric-field effect on magnetic anisotropy in Co/Pd/MgO system," *Appl. Phys. Lett.*, vol. 109, p. 082403, 2016.

[96] H. X. Yang, M. Chshiev, B. Dieny, J. H. Lee, A. Manchon, and K. H. Shin, "First-principles investigation of the very large perpendicular magnetic anisotropy at Fe|MgO and Co|MgO interfaces," *Phys. Rev. B*, vol. 84, p. 054401, 2011.

[97] U. Gradmann and R. Bergholz, "Magnetization of Pd(111) Films by Contact with Ferromagnetic Ni(111) Films," *Phys. Rev. Lett.*, vol. 52, no. 9, pp. 771–774, 1984.

[98] F. J. A. Den Broeder, H. C. Donkersloot, H. J. G. Draaisma, and W. J. M. De Jonge, "Magnetic properties and structure of Pd/Co and Pd/Fe multilayers," *J. Appl. Phys.*, vol. 61, pp. 4317–4319, 1987.

[99] F. Bonell, S. Murakami, Y. Shiota, T. Nozaki, T. Shinjo, and Y. Suzuki, "Large change in perpendicular magnetic anisotropy induced by an electric field in FePd ultrathin films," *Appl. Phys. Lett.*, vol. 98, p. 232510, 2011.

[100] S. Miwa, K. Matsuda, K. Tanaka, Y. Kotani, M. Goto, T. Nakamura, and Y. Suzuki, "Voltage-controlled magnetic anisotropy in Fe|MgO tunnel junctions studied by x-ray absorption spectroscopy," *Appl. Phys. Lett.*, vol. 107, p. 162402, 2015.

[101] T. Tsukahara, T. Kawabe, K. Shimose, T. Furuta, R. Miyakaze, K. Nawaoka, M. Goto, T. Nozaki, S. Yuasa, Y. Kotani, K. Toyoki, M. Suzuki, T. Nakamura, Y. Suzuki, and S. Miwa, "Characterization of the magnetic moments of ultrathin Fe film in an external electric field via high-precision X-ray magnetic circular dichroism spectroscopy," *Jpn. J. Appl. Phys.*, vol. 56, p. 060304, 2017.

[102] P. Bruno, "Tight-binding approach to the orbital magnetic moment and magnetocrystalline anisotropy of transition-metal monolayers," *Phys. Rev. B*, vol. 39, no. 1, pp. 865–868, 1989.

[103] H. Yang, A. Thiaville, S. Rohart, A. Fert, and M. Chshiev, "Anatomy of Dzyaloshinskii-Moriya Interaction at Co/Pt Interfaces," *Phys. Rev. Lett.*, vol. 115, p. 267210, 2015.

[104] T. Nozaki, A. Kozioł-Rachwał, M. Tsujikawa, Y. Shiota, X. Xu, T. Ohkubo, T. Tsukahara, S. Miwa, M. Suzuki, S. Tamaru, H. Kubota, A. Fukushima, K. Hono, M.

Shirai, Y. Suzuki, and S. Yuasa, "Highly efficient voltage control of spin and enhanced interfacial perpendicular magnetic anisotropy in iridium-doped Fe/MgO magnetic tunnel junctions," *NPG Asia Mater.*, vol. 9, p. e451, 2017.

[105] A. Kundu and S. Zhang, "Dzyaloshinskii-Moriya interaction mediated by spin-polarized band with Rashba spin-orbit coupling," *Phys. Rev. B*, vol. 92, p. 094434, 2015.

[106] H. Katsura, N. Nagaosa, and A. V. Balatsky, "Spin current and magnetoelectric effect in noncollinear magnets," *Phys. Rev. Lett.*, vol. 95, p. 057205, 2005.

[107] H. Yang, O. Boulle, V. Cros, A. Fert, and M. Chshiev, "Controlling Dzyaloshinskii-Moriya Interaction via Chirality Dependent Atomic-Layer Stacking, Insulator Capping and Electric Field," *Sci. Rep.*, vol. 8, p. 12356, 2018.

[108] A. Cao, X. Zhang, B. Koopmans, S. Peng, Y. Zhang, Z. Wang, S. Yan, H. Yang, and W. Zhao, "Tuning the Dzyaloshinskii-Moriya interaction in Pt/Co/MgO heterostructures through the MgO thickness," *Nanoscale*, vol. 10, no. 25, pp. 12062–12067, 2018.

[109] J. Cho, N.-H. Kim, J. Jung, D.-S. Han, H. J. M. Swagten, J. S. Kim, and C.-Y. You, "Thermal Annealing Effects on the Interfacial Dzyaloshinskii-Moriya Interaction Energy Density and Perpendicular Magnetic Anisotropy," *IEEE Trans. Magn.*, vol. 54, no. 6, p. 1500104, 2018.

[110] S. Miwa, T. Nozaki, M. Tsujikawa, M. Suzuki, T. Tsukahara, T. Kawabe, Y. Kotani, K. Toyoki, M. Goto, T. Nakamura, M. Shirai, S. Yuasa, and Y. Suzuki, "Microscopic origin of large perpendicular magnetic anisotropy in an FeIr/MgO system," *Phys. Rev. B*, vol. 99, p. 184421, 2019.

[111] G. van der Laan, "Related content Microscopic origin of magnetocrystalline anisotropy in transition metal thin films Microscopic origin of magnetocrystalline anisotropy in transition metal thin films," *J. Phys. Condens. Matter*, vol. 10, pp. 3239–3253, 1998.

[112] Y. Suzuki and S. Miwa, "Magnetic anisotropy of ferromagnetic metals in low symmetry systems," *Phys. lett. A*, vol. 383, no. 11, pp. 1203–0206, 2019.

[113] J. Zhang, Z.-L. Han, S. Varma, and B. P. Tonner, "Epitaxy of fcc and bcc Co, Ni, and Cu studied by X-ray photoelectron diffraction," *Surf. Sci.*, vol. 298, pp. 351–361, 1993.

[114] A. K. Shukla, M. Goto, X. Xu, K. Nawaoka, J. Suwardy, T. Ohkubo, K. Hono, M. Shinji, and Y. Suzuki, "Voltage-Controlled Magnetic Anisotropy in $Fe_{1-x}Co_x$/Pd/MgO

system," *Sci. Rep.*, vol. 8, p. 10362, 2018.

[115] J. S. Lee, J. Y. Kim, J. H. Shim, B. I. Min, K. B. Lee, and J. H. Park, "Microscopic aspect of interface magnetic anisotropy induced by a Pd adlayer on NiCu(001) films," *Phys. Rev. B - Condens. Matter Mater. Phys.*, vol. 76, no. 6, p. 060403(R), 2007.

[116] J. Okabayashi, Y. Miura, and H. Munekata, "Anatomy of interfacial spin-orbit coupling in Co / Pd multilayers using X-ray magnetic circular dichroism and first-principles calculations," *Sci. Rep.*, vol. 8, p. 8303, 2018.

[117] M. Bode, M. Heide, K. Von Bergmann, P. Ferriani, S. Heinze, G. Bihlmayer, A. Kubetzka, O. Pietzsch, S. Blügel, and R. Wiesendanger, "Chiral magnetic order at surfaces driven by inversion asymmetry," *Nature*, vol. 447, pp. 190–193, 2007.

[118] O. Boulle, J. Vogel, H. Yang, S. Pizzini, D. De Souza Chaves, A. Locatelli, T. O. Menteş, A. Sala, L. D. Buda-Prejbeanu, O. Klein, M. Belmeguenai, Y. Roussigné, A. Stashkevich, S. Mourad Chérif, L. Aballe, M. Foerster, M. Chshiev, S. Auffret, I. M. Miron, and G. Gaudin, "Room-temperature chiral magnetic skyrmions in ultrathin magnetic nanostructures," *Nat. Nanotechnol.*, vol. 11, p. 449, 2016.

[119] T. Srivastava, M. Schott, R. Juge, V. Křižáková, M. Belmeguenai, Y. Roussigné, A. Bernand-Mantel, L. Ranno, S. Pizzini, S. M. Chérif, A. Stashkevich, S. Auffret, O. Boulle, G. Gaudin, M. Chshiev, C. Baraduc, and H. Béa, "Large-Voltage Tuning of Dzyaloshinskii-Moriya Interactions: A Route toward Dynamic Control of Skyrmion Chirality," *Nano Lett.*, vol. 18, pp. 4871–4877, 2018.

List of Publication

Name written in underline represents the thesis author
(① Authors, ② Title, ③ Journal, ④ **Vol**, No, pp.-, and Year)

1. ① <u>Joko Suwardy</u>, Minori Goto, Yoshishige Suzuki, and Shinji Miwa
   ② Voltage-controlled magnetic anisotropy and Dzyaloshinskii-Moriya interaction at CoNi/MgO and CoNi/Pd/MgO
   ③ Japanese Journal of Applied Physics (Rapid Communication)
   ④ **58**, 060917 (2019)

2. ① <u>Joko Suwardy</u>, Kohei Nawaoka, Jaehun Cho, Minori Goto, Yoshishige Suzuki, and Shinji Miwa
   ② Voltage-controlled magnetic anisotropy and voltage-induced Dyzaloshinskii-Moriya interaction change at the epitaxial Fe(001)/Mg(001) interface engineered by Co and Pd atomic-layer-insertion
   ③ Physical Review B
   ④ **98**,144432 (2018)

3. ① Amit Kumar Shukla, Minori Goto, Xiandong Xu, Kohei Nawaoka, <u>Joko Suwardy</u>, Tadakatsu Ohkubo, Kazuhiro Hono, Shinji Miwa and Yoshishige Suzuki
   ② Voltage-controlled magnetic anisotropy in $Fe_{1-x}Co_x$/Pd/MgO system
   ③ Scientific Reports
   ④ **8**, 10362 (2018)

4. ① Junyi Chen*, <u>Joko Suwardy*</u>, Thiyagu Subramani, Wipakorn Jevasuwan, Toshiaki Takei, Kaoru Toko, Takeshi Suemasu and Naoki Fukata
   ② Control of grain size and crystallinity of poly-Si films on quartz by Al-induced crystallization
   ③ Crystal Engineering Communication
   ④ **19**, 2305 (2017)

5. ① Ken C. Pradel, Wipakorn Jevasuwan, <u>Joko Suwardy</u>, Yoshio Bando, Naoki Fukata, and Zhong Lin Wang

    ② Solution derived p-ZnO/n-Si nanowire heterojunctions for photodetection

    ③ Chemical Physics Letters

    ④ **658**, 158 (2016)

6. ① <u>Joko Suwardy</u> and Yudi Darma

    ② Thermal annealing effects of SrTiO3 film on Si (100)

    ③ AIP Conference Proceedings

    ④ **1554**, 112 (2013)

7. ① Pia Dinari, Christian Chandra, <u>Joko Suwardy</u>, Salim Mustofa, and Yudi Darma

    ② SrTiO$_3$ thin films deposition using pulsed laser deposition technique

    ③ Advanced Material Research

    ④ **789**, 72 (2013)

* equally contributed first authors

List of Conference Presentation

Name written in underline represents the thesis author
(① Authors, ② Title, ③ Conference name, ④ Place, Number and Date)

2019

1. (Oral presentation)
   ① <u>Joko Suwardy</u>, Kohei Nawaoka, Minori Goto, Yoshishige Suzuki, and Shinji Miwa
   ② Voltage-controlled magnetic anisotropy and Dzyaloshinskii-Moriya interaction change in Fe, Co, Ni and Pd
   ③ 2019 Joint MMM-Intermag Conference
   ④ Washington Marriott Wardman Park, Washington-DC, USA, DA-04, Jan. 2019

2018

2. (Poster presentation)
   ① <u>Joko Suwardy</u>, Minori Goto, Yoshishige Suzuki, and Shinji Miwa
   ② Voltage-controlled magnetic anisotropy of $Co_{1-x}Ni_x$ ultrathin alloy at the interface with MgO
   ③ The 79th JSAP Autumn Meeting
   ④ Nagoya Congress Center, Nagoya, Japan, 18p-PB1-19, Sep. 2018

3. (Oral presentation)
   ① <u>Joko Suwardy</u>, Kohei Nawaoka, Minori Goto, Yoshishige Suzuki, and Shinji Miwa,
   ② Voltage-controlled magnetic anisotropy of Fe/Co/Pd/MgO epitaxial multilayer
   ③ The 65th JSAP Spring Meeting
   ④ Waseda University, Tokyo, Japan, 19a-D104-3, Mar. 2018

4. (Poster presentation)
   ① <u>Joko Suwardy</u>, Kohei Nawaoka, Minori Goto, Yoshishige Suzuki, and Shinji Miwa
   ② Voltage-controlled magnetic anisotropy of Fe/Co/Pd/MgO epitaxial multilayer characterized by spin wave spectroscopy

③ 2017 Spin Conversion Annual Meeting

④ Kyoto Univ., Katsura, Japan, Mar. 2018

2017

5. (Oral presentation)

    ① Joko Suwardy, Kohei Nawaoka, Minori Goto, Yoshishige Suzuki, and Shinji Miwa

    ② Voltage-controlled magnetic anisotropy of Fe /Pd/MgO system

    ③ The 78th JSAP Autumn Meeting

    ④ Fukuoka Convention Center, Fukuoka, Japan, 5p-C18-11, Sep. 2017

6. (Poster presentation)

    ① Joko Suwardy, Kohei Nawaoka, Minori Goto, Yoshishige Suzuki, and Shinji Miwa

    ② Interface magnetism of epitaxial Fe/Pd/MgO multilayer characterized by spin-wave spectroscopy

    ③ 2016 Spin Conversion Annual Meeting

    ④ Tokyo Institute of Technology, Tokyo, Japan, PF-49, Mar. 2017

7. (Poster presentation)

    ① Joko Suwardy, Kohei Nawaoka, Minori Goto, Yoshishige Suzuki, and Shinji Miwa

    ② Influence of Pd layer insertion at Fe/MgO interface on spin-wave dynamics

    ③ The 64th JSAP Spring Meeting

    ④ PACIFICO Yokohama, Yokohama, Japan, Mar. 2017

2016

8. (Poster presentation)

    ① Joko Suwardy, Thiyagu subramani, Wipakorn Jevasuwan, Kaoru Toko, Takeshi Suemasu, and Naoki Fukata

    ② Formation of large-grain polycrystalline Si layer on Quartz by Al-induced crystallization for thin-film solar cells

    ③ The 63rd JSAP spring meeting

    ④ Tokyo Institute of Technology, Tokyo, Japan, 21p-P9-9, Mar. 2016

2015

9. (Poster presentation)
   ① Joko Suwardy, Wipakorn Jevasuwan, Kaoru Toko, Takeshi Suemasu, and Naoki Fukata
   ② Solid phase expitaxy of Si film on poly-Si seed layer formed by Al-induced crystallization
   ③ The 78th JSAP Autumn Meeting
   ④ Nagoya Congress Center, Nagoya, Japan, 14a-PB6-4, Sep. 2015

10. (Oral presentation)
   ① Joko Suwardy, Wipakorn Jevasuwan, Kaoru Toko, Takeshi Suemasu, and Naoki Fukata
   ② Formation of polycrystalline Si layer on Quartz substrate by Al-induced crystallization
   ③ The 62rd JSAP spring meeting
   ④ Tokai Univ., Tokyo, Japan, 12p-A18-1, Mar. 2016

2013

11. (Poster presentation)
   ① Joko Suwardy, and Yudi Darma
   ② Thermal annealing effects of SrTiO3 film on Si (100)
   ③ Padjadjaran International Physics Symposium 2013
   ④ Univ. of Padjadjaran, Jatinangor, Indonesia, 112, May 2013

12. (Oral presentation)
   ① Pia Dinari, Christian Chandra, Joko Suwardy, Salim Mustofa, and Yudi Darma
   ② SrTiO$_3$ thin films deposition using pulsed laser deposition technique
   ③ the 13th International Conference on Quality in Research (QiR) in conjunction with the ICCS 2013
   ④ Sheraton Mustika Hotel, Yogyakarta, Indonesia, B10.6, June 2013